Design Optimisation of Brushless Permanent Magnet Synchronous Motor for Electric Vehicles

NASSER BRAIWISH

A thesis submitted to Cardiff University in the candidature for the degree of Doctor of Philosophy

Wolfson Centre for Magnetics

School of Engineering

Cardiff University

United Kingdom

2016

DECLARATION AND STATEMENT

DECLARATION

This work has not been submitted in substance for any other degree or award at this or any other university or place of learning, nor is being submitted concurrently in candidature for any degree or other award.

Signed …… (Nasser Braiwish) Date …06/12/2016…

STATEMENT 1

This thesis is being submitted in partial fulfillment of the requirements for the degree of Doctor of Philosophy (PhD)

Signed …… (Nasser Braiwish) Date …06/12/2016…

STATEMENT 2

This thesis is the result of my own independent work/investigation, except where otherwise stated. Other sources are acknowledged by explicit references. The views expressed are my own.

Signed …… (Nasser Braiwish) Date …06/12/2016…

STATEMENT 3

I hereby give consent for my thesis, if accepted, to be available for photocopying and for inter-library loan, and for the title and summary to be made available to outside organisations.

Signed …… (Nasser Braiwish) Date …06/12/2016…

Thesis summary

A novel new application of optimisation algorithm “Bess Algorithm” in the design of electric machine is presented in this thesis. The optimisation has the ability to perform global and local search and can be applied on constrained, unconstrained optimisation problem with multi-objective function, which all counted when consider optimisation algorithm for the design of electric machine. The searching procedure of the optimisation algorithm has been described in detailed. Furthermore, novel instructions and recommendation were implemented to tune the optimisation parameters, particularly for the purpose electric machine design, which in turn reduced the search space, increase efficiency and ability to find optimal solution with lower computation time.

The optimisation was applied to search for optimal parameters of a benchmark electric machine with multi-objective to reduce the cost and increase the power density, power-volume ratio and efficiency. Throughout the thesis, a full detailed analytical model for the design of brushless permanent magnet synchronous motor that account for electromagnetic and thermal aspects was described. The optimisation was employed to search for optimal parameters of the analytical model that satisfy the design requirements. Then, the generated optimal parameters were evaluated and verified by Finite Element Analysis, FEA. The results from the FEA show good agreement with their corresponding values in the analytical model within acceptable range. At the same operational conditions and output specifications, the results show that the power density, volume to power ratio and cost of the new optimised motor

were all increased by 19%, 39%, 24% respectively and the efficiency reduced only by -1%.

The optimisation was also compared with one of the most usable optimisation algorithm used in the design of electric machine i.e. Genetic Algorithm. The results show that bees algorithm has more ability to cover the search space with less number of recruited bees and less number of iterations and higher computation efficiency.

Acknowledgment

First and foremost, all praise and thanks are to Allah, God the Almighty, most beneficent and most merciful.

I would like to express the deepest appreciation and gratitude to my supervisor, Dr Fatih Anayi for his kind guidance, support and encouragement during my doctoral studies at Cardiff University. The perspective valuable friendly discussions and approach he brings towards research have had a deep and beneficial influence on me.

I would like to thank Dr Nabeel Shirazee from Electronica Products UK, Ltd, for his professional advices and the benchmark design. My special thanks also go to Infolytica Ltd, for providing me with finite element package.

I would like to present my sincere thankfulness to my dear family. My mother, your prayer for me was what sustained me thus far. Words cannot express how grateful I am to my deceased father, for his great role in my life and his numerous sacrifices for me and for my brothers. I would also like to thank my brother and sisters, particularly Abu Rashid, for their heartening and encouraging.

Finally, and most importantly, I would like to thank my wife and my wonderful children Sarah, Kareem and Yousef for all support and encouragement during these years.

Abstract

The design of the electric motor for traction applications encompasses strict requirements and objectives in the machine's size, weight, power density, efficiency and cost, all conflicting with each other. Furthermore, the design of electric machines is a comprehensive mission based on multi-physics electromagnetic, mechanical and thermal models. However, with recent improvements in power electronics, materials and applications, the old, conventional method used to design electric machines has become outdated. Consequently, extensive effort has been devoted to optimising electric machines with respect to different objectives, such as efficiency, power density, cost, and reliability.

In recent decades, numerous automated design optimisation technologies have been adopted for the design of electric machines for different applications. The inherent limitations of an individual optimisation search algorithm and the effect of these limitations in solving general optimisation problems has raised the need for a new algorithm that is able to consider constraint parameters and multi-objective functions. Therefore, this thesis introduces a new optimisation algorithm in the design of electric machines i.e. "Bees Algorithm" (BA). BA is a new optimisation algorithm that mimics honeybees and has been adopted to solve many realistic engineering design problems. With the setting six parameters, Bees Algorithm has the ability to perform both exploitative neighbourhood (local) search and explorative global search of an optimisation problem. The algorithm is also reliable in handling complex multi-objective functions that satisfy the constraints quickly and efficiently.

Based on specification of a benchmark machine, this thesis describes the design and development of high power density three-phase brushless permanent magnet motor through Bees Algorithm. The optimisation will be employed to search for new optimal four prime variables that subject to constraints and have conflicting objectives function. The generated new optimal parameters will be used evaluate the dimensions, electromagnetic and thermal parameters of the new optimised machine, which will be verified by FEA. Then, the performance indices of the resulted machine will be compared with their corresponding values in the benchmark design. The results show that new optimised machine with the same efficiency has benefit of higher power density, lower volume and cheaper cost.

List of abbreviations and nomenclatures

Abbreviations

ACO	Ant Colony Optimisation algorithm
AWG	American wire gauge
BA	Bees algorithm
BEM	Boundary Element Method
BLPMDC	Brushless permanent magnet direct current motor
BLPMSM	Brushless permanent magnet synchronous motor
CPR	constant power region
CTR	constant torque region
CVT	continuously variable transmission
EMF	electromotive force
EMG	electronic-magnetic gearing
EV	Electric Vehicle
FCVT	FreedomCar and vehicle Technologies
FDM	Finite Difference Method
FEA	Finite Element analysis
FEM	Finite Element Method
FGT	fixed-ratio gear transmission
GA	Genetic Algorithm
HEV	Hybrid Electric Vehicle
IM	Induction Motor
MMF	Magnetomotive Force
MEC	Magnetic Equivalent Circuit
MLS	moving of least square
NdFeB	Neodymium Iron Boron
PC	Permeance Coefficient
PM	Permanent Magnet
PMM	Point Mirroring Method
PSO	Particle Swarm Optimisation

REM	Rare Earth Magnets
RMS	Root Mean Square
SI	Swarm Intelligence
SmCo	Samarium Cobalt
SMPMSM	surface mounted permanent magnet synchronous machine
SRM	Switched Reluctance Motor
SUMT	Sequential Unconstrained Minimization Technique
TENV	Totally Enclosed Non-Ventilated
UQM	Unique Mobility Inc.

Nomenclatures

A	Area
ac	Specific electrical loading A/m
A_{wire}	Strand cross section area
A_{slot}	Slot area
A_{cu}	Copper area per slot
$\overline{B}$	Specific magnetic loading (T)
B	Magnetic flux density
B_{arm}	Flux density doe to armature reaction
B_i	Intrinsic magnetic flux density
B_r	Remanent magnetic flux density
B_k	The flux density value on the demagnetization curve where magnetic polarization vector collapses (T)
BH_{max}	Maximum energy product
B_{so}	Slot opening width
B_g	RMS airgap flux density
$B_{g(1)}$	First harmonic of the magnetic airgap flux density
B_{sm}	Mean width of stator slot
B_{knee}	Knee point of lamination B-H curve
B_{max}	Lamination maximum flux
D	Stator inner diameter (m)

D_{frame}	Frame diameter
EMF	Electromotive force
$EMF_{(1)}$	Flat-top electromotive force
f_{LKG}	Leakage coefficient
f	Electric frequency
H	Magnetic field intensity
H_c	Magnetic coercivity
H_{ic}	Intrinsic coercivity
h_m	Magnet thickness
H_s	Total height of slot
H_k	The field intensity value on the demagnetization curve where magnetic polarization vector collapses (A/m)
I	Electric current
I_{LR}	Locked-rotor current
I_{ph}	Phase current
I_{demag}	Demagnetisation current
J	Current density
k_c	Carter's coefficient
k_h	Hysteresis loss coefficient
k_{ec}	Eddy current loss coefficient
k_{ds}	Tooth flux concentration factor
k_w	Fundamental winding factor
k_s	Lamination stacking factor
K_{fill}	Slot fill factor
k_{exp}	Coefficient of thermal expansion
L	Machine axial length (m)
l	Path length
L_s	Synchronous inductance
L_{ew}	End-winding inductance
L_{sl}	Slot leakage inductance

L_{sg}	Airgap inductance
l_{turn}	Total of the length of one turn
l_{end}	Turn's end-winding length
MMF	Magnetomotive force
$mmf_{(PM)}$	Magnetomotive force produced by the permanent magnet
N_m	Number of stator slots
N_{ph}	Number of turn in series per phase
N_p	Number of poles
N_{mpp}	Number of slots per pole
N_{spp}	Number of slots per pole
N_u	Nusselt number
OD	Stator outer diameter
p	Number of pole-pairs
P_{m0}	Internal magnet permeance
P_{core}	Laminations Iron losses
P_{cu}	Copper losses
P_{slot}	Slot permeance coefficient
P_{elm}	Electromagnetic Power
P_{hys}	Hysteresis loss
P_{edd}	Eddy current loss
P_{wind}	Windage loss
P_{fric}	Friction loss
Pr	Prandtl number
q	Number of slots per pole per phase
rps	Revolution per second
$\Re$	Magnetic reluctance
R_{ph}	Phase resistance
R_{dc}	Direct current phase resistance
Ra	Rayleigh number
S	Electric motor rating power

S_{DO}	Stator outer diameter
S_{ebi}	Thickness of stator back-iron
R_{ebi}	Thickness of rotor back-iron
T_w	Stator Tooth Width
T	Torque
T_m	Mean temperature
T_{PM}	Permanent magnet temperature
T_{am}	Modified Taylor's number
T_{Cu}	Winding temperature
T_{max}	Maximum torque
T_{avg}	Average torque
V_t	Terminals voltage
V_{dc}	Supply Voltage
w_m	Magnet Width
Wt	Weight
X_d	d-axis synchronous reactance
X_q	q-axis synchronous reactance
X_s	Synchronous reactance
α_{Br}	B_r reversible temperature coefficient
α_{Hc}	H_c reversible temperature coefficient
α_{Cu}	Copper reversible temperature coefficient
α_p	Ratio of the magnet-pitch to the total pole-pitch
β	Ratio of slot pitch to pole pitch
λ	Machine aspect ratio
ϕ	Magnetic flux
ψ	Flux linkage
μ	Material magnetic permeability
μ_0	Air magnetic permeability
μ_r	Relative permeability
μ_{rec}	Recoil Permeability
τ_s	One slot pitch

τ_p	One pole-pitch
τ_{Tw}	One teeth-pitch
τ_c	Length of end winding pitch
ρ_{cu}	Copper electric resistivity
η	Efficiency
λ_r, λ_a	Radial and axial thermal conductivities
v	Viscosity of the air
g_r	Gravitational constant
Ω	Angular velocity of the rotor

Table of Contents

List of Tables

Table of figures

1 Chapter 1: Introduction and objective of research

1.1 Introduction

In recent years, Brushless Permanent Magnet Synchronous Motor (BLPMSM) has become the most widely used motor for traction application in Electric Vehicles (EV) and Hybrid Electric Vehicles (HEV) [1]. It has been used in the production of many hybrid vehicles e.g. Toyota Prius, Honda Accord, and Ford Escape [2]. Compared with Induction Motor (IM) and Switched Reluctance Motor (SRM), the BLPMSM constitutes a good choice for applications where steady-state operation, high efficiency and torque density are needed [3]. However, for traction application there are general ideal characteristics required in electric machines, including the following [1, 3, 4].

- High torque density and power density
- High torque for starting, at low speed and hill climbing, and high power for high-speed cruising.
- Wide speed range, with constant power operating range of around three to four times the base speed being a good compromise between the peak torque requirement of the machine and the volt-ampere rating of the inverter.

- High efficiency over wide speed and torque ranges, including low torque operation.
- Intermittent overload capability, typically twice the rated torque for short durations.
- High reliability and robustness appropriate to the vehicle environment.
- Low acoustic noise and low torque ripple [5].
- Acceptable cost.

Recently, various types of electric machines have been developed and applied on traction applications. Table 1.1 summarises the advantages and disadvantages of each type of motor. Compared with the ideal characteristics required of an electric machine for traction application, the BLPMSM is the type of motor that offers the best efficiency and high power density, making it the best choice to drive modern electric vehicles.

Table 1.1 Advantages and disadvantages of different types of motors

Motor Type	Advantages	Disadvantages
BLPMSM	• High Power density • High efficiency	• Limited speed range • High cost • High stator core losses at high speed
Induction motor (IM)	• High speed range • High reliability • Low cost • Rigidity in hostile environments	• Low efficiency • Thermal problem at high speed
Switched reluctance motor (SRM)	• Desirable torque speed characteristics • High reliability • Low cost • Rigidity in hostile environments	• High torque ripple and noise • Low power density • Low efficiency

Despite substantial improvements in modern materials, power electronics and computing tools over recent decades, electric machines are still designed based on old, conventional methods that were established more than half a century ago. Therefore, it is important to develop a new method that reflects modern progress in electric drives, materials and manufacturing abilities. In this respect, considerable effort has been spent over recent decades in developing a method based on optimisation to improve the design of electric machines.

Generally, to accomplish an electric machine design based on optimisation, the designer needs essentially two tools: first, an accurate analytical model to design the electric machine; and second, an efficient optimisation algorithm as shown in Figure 1.1 [6]. While the design based on analytical modelling takes its input variables from the optimisation to calculate the relationships between the electromagnetic, mechanical, and thermal aspects of the machine simultaneously, the optimisation studies all the possible options and allows the designer to find a compromise between material properties, machine dimensions, the cost of production and assembly processes that satisfies the design specifications. Therefore, the proposed research is stimulated to design both an accurate analytical design and efficient optimisation.

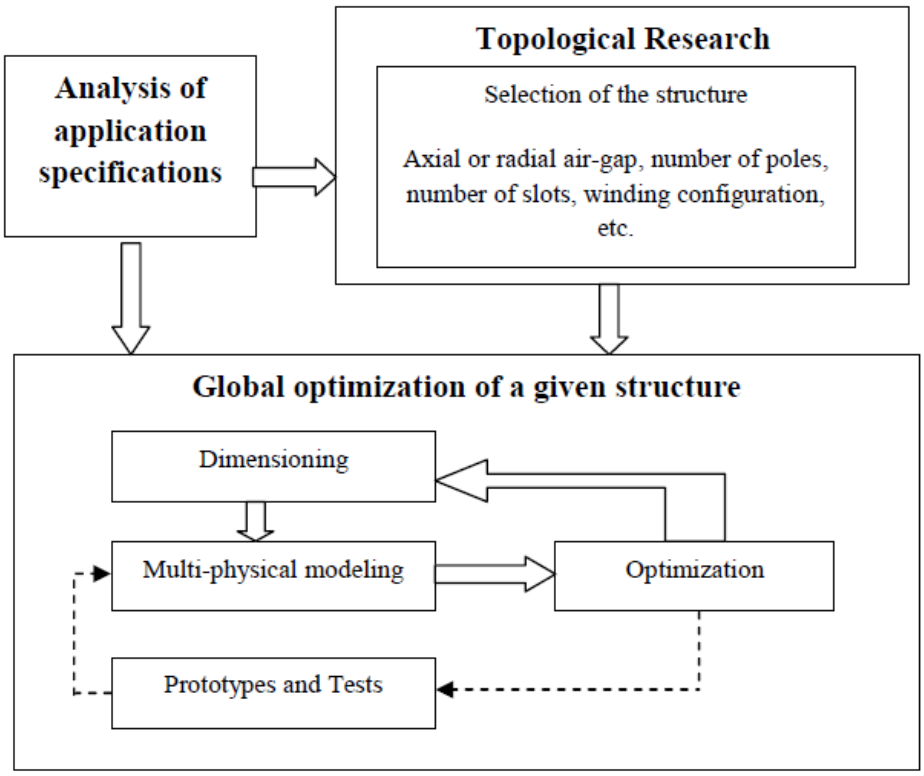

Figure 1.1 Diagram of general electric machine design based on optimisation

1.2 Motivation and research objectives

Given the context and the continuous need for improving electric machines, this research focuses on the design methodology for BLPMSM for traction application based on optimisation. The main objectives of the proposed research are as follows:

1. To compute a comprehensive and accurate analytical modelling for BLPMSM. The design specifications and requirements are based on a benchmark motor that has been developed by "Electronica Products Limited, UK".

2. To apply a new optimisation algorithm i.e. Bees Algorithm (BA) to search for optimal design parameters that are needed to improve the performance of the benchmark design in term of power density, volume, efficiency and cost.
3. Provide comprehensive analysis of the optimisation search criteria and explain both local and global searches in the Bees Algorithm, as well as provide instructions that help the user to efficiently tune the algorithm parameters for the particular specification of an electric machine design.

1.3 Dissertation outline

Chapter 2 reviews the old, traditional method in the design of electric machines. Also presented are brief descriptions of the search procedure of recently applied optimisation algorithms in electric machine design. The chapter covers the most recent developments in electric machine optimisation.

Chapter 3 demonstrates and compares the different methods employed to evaluate and compute magnetic field problems. It also presents the possibilities of integrating these methods into algorithm search processes. In addition, this chapter introduces the characteristics of permanent magnet materials and their behaviours as illustrates in the demagnetisation curve. The chapter also clarifies in detail the "equivalent magnetic circuit" in analysing of the magnetic circuit of a surface mounted permanent magnet machine.

Chapter 4 provides full assessments of the benchmark design using finite element analysis (FEA) to evaluate the electromagnetic and thermal performances of the benchmark design. Also in this chapter, the analysis of the characteristics of torque,

power, and efficiency of the benchmark is simulated and the performance indices are evaluated.

Chapter 5 introduces an analytical model of a surface mounted permanent magnet machine, including an evaluation of the electromagnetic, thermal and losses of an electric machine. The proposed analytical study also includes the selection of some machine parameters before optimisation. The analytical model also includes constraints and penalty functions to ensure the delivery of a feasible design. Finally, a multi-objective function of the design is expressed to match with the required aims of the design.

Chapter 6 provides more details about the search criteria that Bees Algorithm follows to survey the optimisation search space. The chapter also analyses the relation between the algorithm parameters, search space boundaries and the variables in the optimisation problem and their impact on the overall search performance, particularly for an electric machine design.

Chapter 7 shows the values of the new optimal variables generated from the Bees Algorithm and the evaluation of the new optimal machine on the basis of these new optimal variables. The evaluation involves verification of the electromagnetic and thermal parameters in the analytical model and simulation of the new optimised machine on numerical analysis. Finally, the new optimised machine is compared with the benchmark design in terms of their performance indices weight, volume, cost and efficiency.

Chapter 8 summaries the conclusion, contributions and recommendations for future work.

2 Chapter 2: Literature Review

2.1 Design and optimisation of Electric Machine

2.1.1 Overview

Since its invention in 1820, the design methodology of the electric machine has gone through diverse stages to develop a fitting way to search for ideal design parameters. Until 1979, the design of electric machines was implemented by an old, traditional design method that was dominated by the rule of thumb and historical empirical curves. Recent developments in power electronics, the generation of new magnetic materials, electric machine applications and manufacturing processes have stimulated the need to find a more efficient design methodology to convey these improvements. A summary of the work conducted using the old, traditional method shows that this method has slowly become outdated and has often not made use of progress to improve machine performance. Therefore, a decision for a novel machine design method that can reflect recent developments in electric machines is urgently required.

Therefore, in this chapter, a comprehensive literature survey is introduced to summarise the traditional design method and the latest progress in optimisation of electric machines design. An evaluation of various recent optimisation algorithms that

focuses on their abilities and limitations in searching for optimal design parameters is also presented. The computational efficiencies and accuracy of optimisation algorithms, with consideration of the ability to reflect constraints and specifications, is also summarised.

2.2 Traditional method for electric machines design

The procedure of the traditional design method, as reviewed, was governed by semi-empirical sizing equations, a general, heuristic guideline and rule of thumb that predominantly reflect designer experiences. The procedure is also based on a limited number of material curves that are not intended to be strictly accurate or reliable for every situation. After determining the machine electric and magnetic loading, the procedure is followed by iterative processes to tune some parameters, as shown in Figure 2.1 [7].

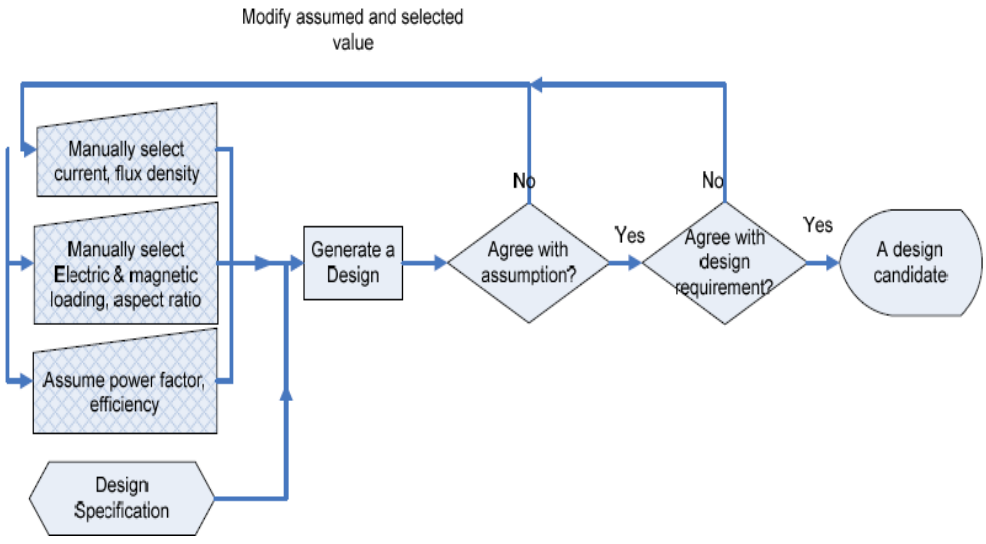

Figure 2.1 Illustration of the iterative design process in the traditional machine design

To achieve the required design outputs, the designer begins by selecting appropriate values for the main design dimensions as shown in the sizing equation (2.1) [8]

$$S = 11k_w \times \overline{B} \times ac \times D^2 L \times n \quad (2.1)$$

Where, S is the electric motor rating power W, $\overline{B}$ is the specific magnetic loading in Tesla (T), ac is the specific electrical loading in A/m, D is the stator inner diameter (m), L is the machine active length (m), kw is the fundamental winding factor and n is the rated speed in revolution per second (rps).

According to the available cooling strategy, the designer estimates the values for the magnetic and electric loading. The selection of magnetic loading $\overline{B}$ depends on the saturation point and core loss of the available limitation materials, while the value of electric loading ac depends on the current density δ and type of winding insulation materials. Both B and ac values are selected from guidebooks based on common collected data and designers' experiences, such as the table in Figure 2.2 [7].

D m.	$\frac{L}{D}$ max.	Slip-ring			Cage		
		$\overline{B}$ Wb./m.²	ac amp.-cond./m.	δ A./mm.²	$\overline{B}$ Wb./m.²	ac amp.-cond./m.	δ A./mm.²
0·1	0·8	0·3	6 000	3·8	0·3	11 000	4·0
0·15	0·75	0·35	10 000	3·6	0·35	15 000	3·8
0·2	0·7	0·4	13 000	3·4	0·4	18 000	3·6
0·3	0·65	0·43	17 500	3·3	0·43	22 500	3·5
0·4	0·62	0·45	21 500	3·2	0·45	26 000	3·5
0·5	0·6	0·46	25 000	3·2	0·46	29 000	3·5
0·75	0·5	0·47	30 000	3·2	0·47	33 000	3·5
1·0	0·42	0·48	32 500	3·2	0·48	35 000	3·5
1·5	0·33	0·5	34 000	3·2			
2·0	0·3	0·51	35 000	3·2			
3·0	0·3	0·53	37 000	3·2			

Figure 2.2 Traditional table to select magnetic and electric loading

From the table, it is clearly shown that only limited magnetic loading ($\bar{B}$) up to 0.53T, limited electric loading (ac) up to 37000 amp.cond/m and limited current density up to 4.0 A/mm2 have been considered. This indicates the limited availability of the soft

and hard magnetic material for the design and the limited cooling strategy, probably an air-cooling system, available for the design. By contrast, in the modern application, the magnetic loading where Rare Earth Magnets (REM) are used, the magnetic loading can go to more than 0.75T. In addition, in modern cooling strategies, such as liquid cooling and intensive oil spray cooling systems, the current density can rise to 28A/mm2 [9]. Furthermore, within the past decade, the improvements in lamination materials have allowed electric machines to operate at higher flux densities with fewer iron losses. This led to smaller teeth width and thinner back-iron in the stator and, therefore, resulted in smaller size machines. Comparing traditional silicon steel with that of modern magnetic material, such as Nickel-iron and Iron-cobalt, Figure 2.3 shows that, at the same frequency and magnetic flux density, silicon-steel has power loss ten times that of Nickel-iron. Also, as shown in Figure 2.4, for the same materials, the B-H curves indicate that the saturation level for silicon steel is much higher than that for Nickel-iron. This means that the Nickel-iron will be saturated at a lower flux density and then the magnetic circuit for using this material will be designed to operate at a lower airgap flux density. Accordingly, it can be concluded that empirical curves with fixed saturation levels and estimated losses cannot reflect the improvement in modern lamination materials.

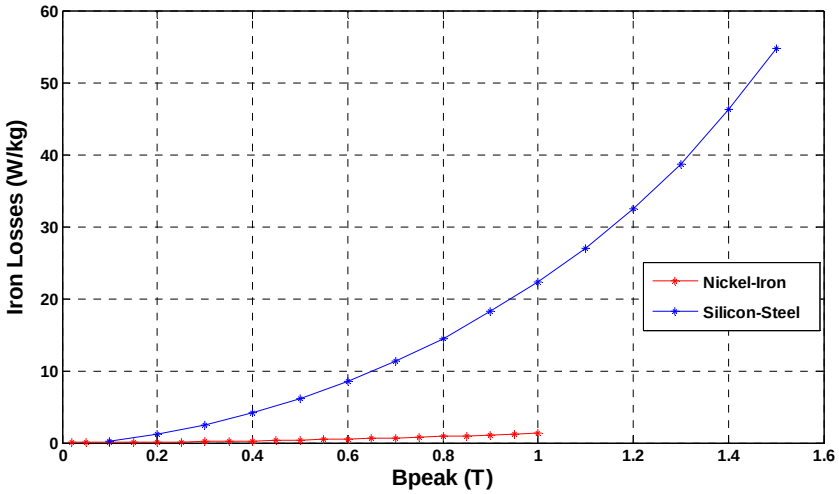

Figure 2.3 Loss curve for silicon steel and Nickel-Iron at 400Hz

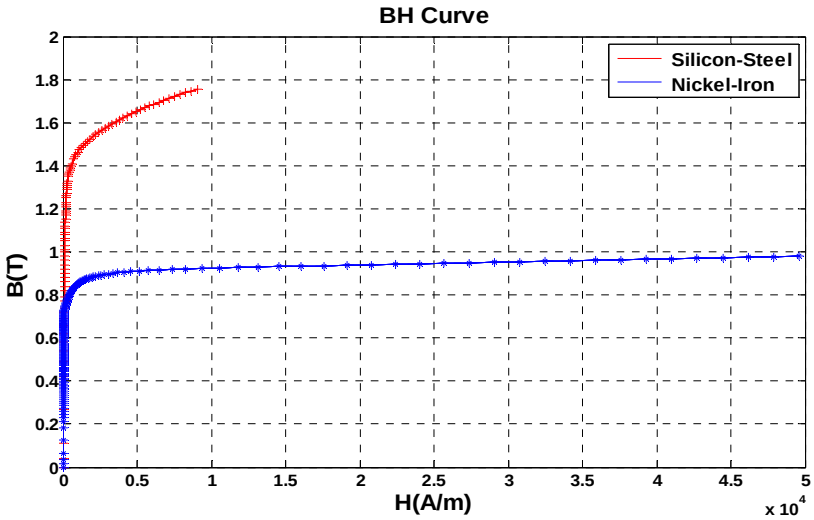

Figure 2.4 BH curve of silicon steel and Nickel-Iron

Thereafter, upon selection of specific magnetic and electrical loading, the designer estimates the ratio between the stator inner diameter D and the machine active length L from the sizing equation (2.1). At this stage, the designer again needs to use an empirical curve and another sizing equation to approximate an appropriate number of pole-pairs p for the machine to calculate the machine aspect ratio λ, as shown in Figure 2.5 and Equation (2.2) [10].

$$\lambda = \frac{L}{\pi D/p} \tag{2.2}$$

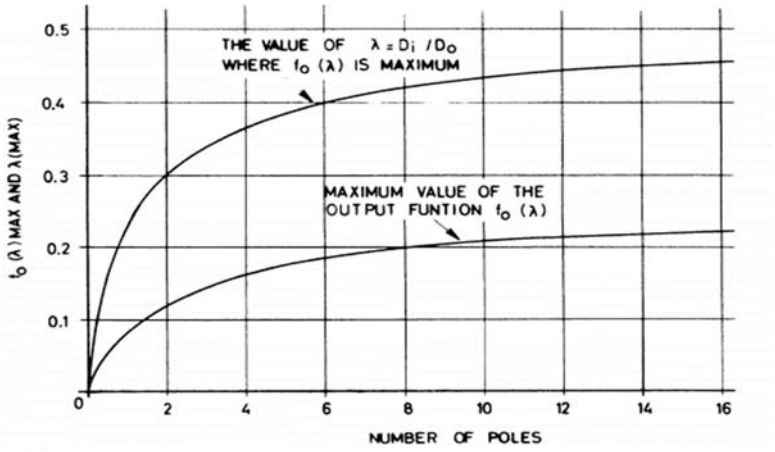

Figure 2.5 Traditional curve for the selection of the aspect ratio λ [10]

However, the selection of aspect ratio λ based on Equation (2.2) cannot be useful in some applications where small machine outer diameter and high power density are concerned. Furthermore, the determination of aspect ratio λ is not only limited by the parameters used in Equation (2.2), it is extended to include different machine variables, such as material utilisation, required performance, machine manufacturing feasibility, and cooling possibility.

After selecting the values for B, ac, p and λ and in order to determine the machine size, the designer needs to estimate another important factor, which is current density (J). In its simple form, current density is the amperes in conductor divided by the area of the conductor $J = I/A_{wire}$. The selection of the current density J, using the traditional method, is based on a typical value range between 3 and 5 A/mm2 [7] and the designer estimation for the machine rated current and evaluation of temperature rise. According to the selected value of current density, the cross-sectional area of copper wire is determined. However, a higher value of current density can lead to smaller wire diameter, which proportionally increases copper losses and subsequently temperature rise. According to [11], the excessive current density in an electric

machine is a common cause of electric machine failure. At rated current and high frequency, when the wire diameter is too small, the eddy current in the wire forces much of the current to flow near the outside of the conductor directly under the insulation. This can cause localised heating in the insulation, which may cause the insulation material to bubble-up and deteriorate the insulation system. Furthermore, the limitation of current density between 5-7 A/mm2 is valid only for air-cooling systems and does not reflect modern improvements where the current densities can increase sometimes up to 10 A/mm2 for air cooling systems and up to 28A/mm2 for liquid and gas cooling systems [9].

From the aforementioned procedure for electric machine design, it is clear that the traditional method is based on semi-empirical curves, fixed tables and to a high degree has relied on designer experience to select the magnetic and electric parameters. The semi-empirical curves and tables are valid only for a limited number of materials and does not take into account the improvement in modern materials and the reduction of power electronics cost in recent decades.

However, the design of an electric machine is a multi-physics task based on electromagnetic, mechanical and thermal analytical modelling which cannot be designed separately. Throughout the procedure of the traditional design method, only limited connections between these models have been considered. Therefore, there is no genuine relation, neither between the diverse machine models nor the design input parameters and machine output performance. Moreover, there is no information guide for the designer as to how to tune parameters to improve the design in the next iterations.

Furthermore, electrical machine design is a comprehensive process based on several factors, including economic, material availability, specifications and special application-dependent factors. At the same time, machine design is a multi-physics task comprising electromagnetic, insulation, thermal and mechanical design. Therefore, there is an absolute requirement for a modern design method that is flexible, reliable and reflects up-to-date improvements in modern science and technologies.

2.3 Previous work on the optimisations of electric machine design

Since 1980, with the escalating need for electric machines, the desirability for a reliable and flexible design optimisation method for electric machines has become urgently needed. The sophisticated nature of the electric machine makes the optimal design a difficult and challenging task. Electric machine design is concerned with paying particular consideration to machine weight, cost, volume and efficiency. The optimisation problem of an electric machine involves continuous and discrete variables from different domains of physics that make the objective functions nonlinear and having no analytical expression [12]. The design of electric machines contains analyses of electromagnetic, mechanical and thermal modelling that are closely related and, practically, cannot be designed independently. This makes the composition of an electric machine complex and based on multi-physics analysis. Therefore, the need for efficient tools that are able to trade-off between the design objectives and expeditiously search for optimal parameters is imperative.

With the development of computer technology, the design of electric machines using different optimisation techniques has received considerable research interest. Optimisation algorithms have been proved to search effectively for optimal design

parameters and compromise conflicted objectives to generate a feasible design that matches the available resources of the design inputs with the required output performance. Therefore, compared with the old traditional heuristic approaches to solving engineering problems, it is apparent that adopting modern algorithm techniques to search for optimal design parameters has made optimisation algorithms very attractive from both technical and business points of view.

Within the past decade, various optimisation algorithms have been investigated for the design of electric machines. The main goal of these investigations was to find an ideal optimisation method that could search for an optimum solution to all optimisation problems. However, according to the "No Free Lunch Theorem", if an algorithm performs well on a certain class of problems, then it necessarily pays for that with a degraded performance on the set of all remaining problems [13]. Therefore, there is no ideal algorithm that works perfectly for all optimisation problems; instead, the proper optimisation is the one that can efficiently survey all search space and find the optimal solution with a lower number of iterations. Thus, one of the main boundaries to utilising design optimisation is the difficulty in selecting the suitable optimisation method for a given problem.

The search space for a given problem is characterised by the type of responses, and the number and range of the design variables. In the case of electric machine design, the algorithm has to correspond between machine geometries and performance, taking into account the properties of the available materials. Such a model usually contains a large number of input data. In some optimisation methods, such as Sequential Unconstrained Minimisation Technique (SUMT), the algorithm works successfully

when there is a possibility to tune the gradient of the solution accordingly with the variables; on the other hand, stochastic methods tend to need more evaluations but are gradient free [14]. Some optimisation strategies, however, can perform well in discrete variable or continuous variable yet not both. Other optimisations require a large number of iterations and evaluations to be performed before reaching an optimal solution. Therefore, with a specific end goal to pick the best optimisation technique for a given problem, one must first comprehend the type of design space that is being searched.

Generally, an optimisation search procedure can be stated as finding the combination of independent variable parameters that maximise or minimise a given single or multi objective function, possibly subject to some constraints within the limited bounds for parameter [15].

Mathematically, the definition of the optimisation procedure can be stated as follows [16, 17]:

- Starting from the initial design parameter vector

$$\bar{X}_0 = [x_{01}, x_{02}, \dots\dots, x_{0D}], \quad \bar{X}_0 \in R^D,$$

- Find the final design parameter vector

$$\bar{X}_m = [x_{m1}, x_{m2}, \dots\dots, x_{mD}], \quad \bar{X}_m \in R^D,$$

- This satisfies the objective function set

$$f(\bar{X}_m) = [f_1(\bar{X}_m), f_2(\bar{X}_m), \dots\dots, f_k(\bar{X}_m)],$$

- And which subject to the design constraints

$$g_i(\bar{X}_m) \leq 0 \quad \text{For } i = 1,2,\ldots\ldots,n$$

- Where the boundaries of the design parameters are defined as

$$x_j^{(L)} \leq x_j \leq x_j^{(u)} \quad j = 1,2,\ldots\ldots,D$$

Based on these search criteria, several computational optimisation techniques have been utilised and improved to solve engineering problems. Swarm Intelligence (SI) procedures that are based on population were the dominant means to search for an optimal solution to the design of electric machines.

Swarm Intelligence (SI) concept is an ingenious mathematical procedure that emulates nature methods to drive a search toward the optimal solution of different parameter settings of the design process. Unlike the direct search algorithms, such as "hill climbing" and "random walk" that use a single solution, SI algorithms use a population of solutions that is processed in every iteration to outcome with another population of solutions to converge to the final optimum. In each population-based algorithm, there is a strategy used to generate variations of the solution that is being sought. Some search methods are greedy, where the convergence to the optimal solution accepts a new solution if, and only if, it increases the value of the objective function. On the other hand, some other search methods are non-greedy, where they can successfully find the true optimum solution even if it involves moving to the worst solution during the search. An example of SI includes the Ant Colony Optimisation algorithm (ACO) that emulates the behaviour of real ants, Genetic Algorithm (GA), based on natural selection and genetic recombination, and Particle Swarm Optimisation (PSO), based on the social behaviour of groups of organisations such as the flocking of birds or

schooling of fish. Summarised below are a brief introduction and operating principles for the most popular swarm optimisation algorithms currently used for the design of electric machines.

2.3.1 Genetic Algorithm

Genetic algorithms GA developed by Holland [18] are adaptive algorithms based on the mechanism of natural selection and genetics for finding the global optimum solution for an optimisation problem [19]. Hence, when applied to optimisation problems, the GA has the advantage of performing a global search only [20]. However, GAs have been widely used for solving complex electromagnetic problems and optimising final design behaviour of electric machines [16, 21]. The simple genetic algorithm is characterised by binary representation of individual solutions, crossover and mutation operators, and proportional selection rule. The standard procedure search of the genetic algorithm is outlined in Figure 2.6.

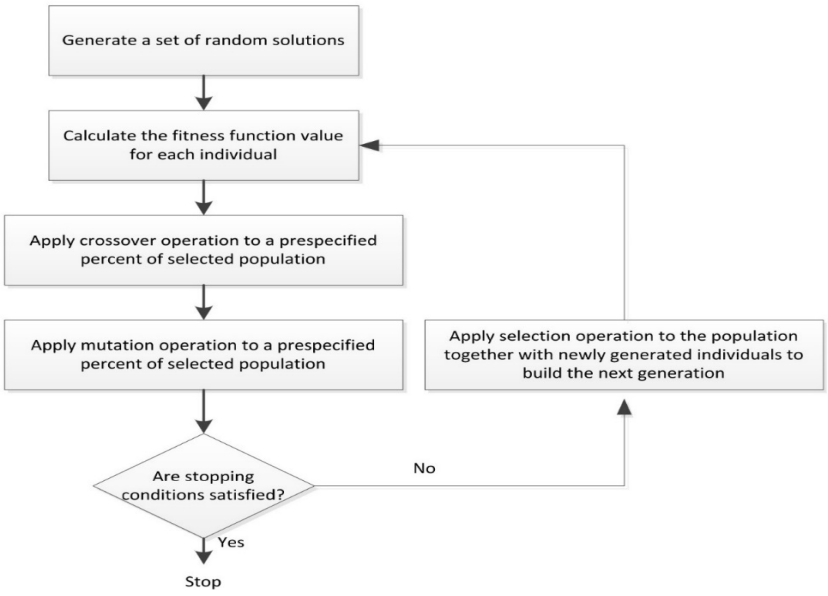

Figure 2.6 Standard search procedure of genetic algorithm

GA is a stochastic algorithm where population solution members are randomly initialised. The population members are encoded into binary representations called "strings" or "chromosomes". The chromosomes are evaluated according to an objective function and a fitness score is assigned for each chromosome. At each cycle, the algorithm creates pairs of subset populations called "parents" and scales them into a raw fitness score; only the populations with higher/lower fitness values are chosen to pass to the next generation.

The algorithm performs a selection rule of combinations (crossover and mutation) to reproduce offspring or children. Crossover is an evolution process involving exchange of genetic materials between individuals, which usually occurs between randomly selected parents. In GA, crossover is the main and most important operation to generate new points in the feasible domain towards the search for global optimum. Genetic mutation occurs to a small fraction of the children by randomly picking the location of a bit-string and flipping its content. The importance of mutation in GA is secondary and aims to introduce new genetic characteristics in the population. However, the after mentioned procedure is repeated until the stopping criteria are met [22, 23].

From the previous procedure; GA has the advantage of performing a global search. The exchange material between individuals through crossover and mutation does not represent a sufficiently intensive search around a proposed prime variables solution. According to [9], in engineering problems, it is generally considered practical to intensify the search around a local solution. Therefore, in the optimisation of electric

machines, it is more convincing to employ optimisation that can perform an intensive search around local optima.

2.3.2 Particle Swarm Optimisation PSO

Particle Swarm Optimisation PSO is an evolutionary optimisation technique developed in 1995 by Kennedy and Eberhard [24]. PSO is a population stochastic algorithm inspired by social behaviour simulation, such as a flock of birds.

The PSO consists of a swarm of particles where each particle represents a candidate solution to the optimisation problem. Each particle holds a position and velocity vector and is treated as a point moving in the n-dimensional search space. Each particle adjusts its "flying" according to its own flying experience, as well as the flying experience of the other particles. However, the best previous position and velocity of each particle are recorded and saved at the end of each iteration. At each iteration, each particle changes its position by two "best" values. The first one, called "personal best", is the best fitness value achieved so far by that particle. The second value, called "global best", is the value obtained so far by any particle in the neighbourhood of that particle. After finding these two best values, the particle updates its velocity and position according to the relative best.

However, in PSO, there is no material exchange (crossover or mutation) between particles; instead each particle's trajectory is influenced by its previous best position in the local or global population. Hence, PSO has the capability to conduct both local and global searches. The process repeats in this way until the stopping criteria are met. The searching criteria flow chart of PSO is shown in Figure 2.7.

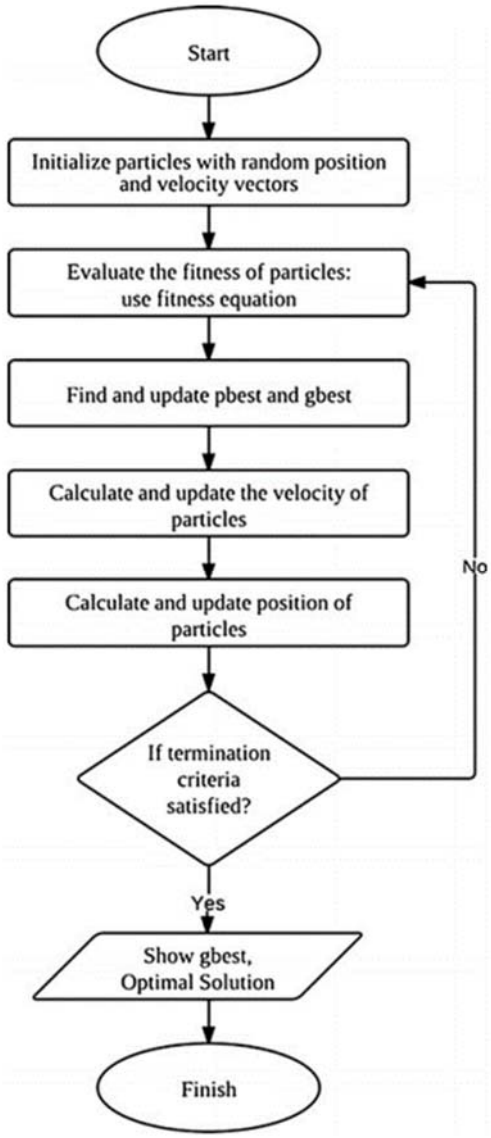

Figure 2.7 Standard search procedure of Particles Swarm Optimisation PSO

Recently, a new version of PSO has been introduced by adding inertia weight to the search processes that control the effect of the previous history of velocities on the current velocity [25]. Accordingly, the inertia weight has impact to trade-off between global and local exploration abilities of the flying points. A large inertia weight encourages the global search area, while small inertia tends to local exploration. Suitable choice of the inertia weight provides a balance in the middle of global and

local exploration capacities and in this way, requires fewer iterations to find the optimum.

PSO was applied for the optimisation of synchronous reluctance motor [26], induction motor [27] and surface mounted machines with segmented pole [28]. With proposed improvement versions, PSO received a large amount of interest from researchers for optimising multimodal functions such as Auto-tuning multi-grouped PSO [29] applied for the optimisation of interior permanent magnet generator [30].

2.3.3 Bees Algorithm (BA)

The Bees Algorithm (BA) is a population-based search algorithm recently developed by a group of researchers at the manufacturing Engineering Centre, Cardiff University (Pham et al. 2006a). BA mimics the food foraging behaviour of a swarm of honeybees and could be regarded as belonging to the category of "intelligent optimisation tools" [31]. Compared with Genetic Algorithm and Particle Swarm Optimisation and (PSO), the Bees Algorithm is the most recent.

The Bees Algorithm, in its basic version, depends on six parameters, which are: the number of scout bees (n), the number of selected sites (m), number of elite sites out of (m) selected sites (e), number of bees recruited for non-elite sites (nsp), number of bees recruited for each elite site (nep) and neighbourhood size (ngh).

The Bees Algorithm's search flowchart is shown in Figure 2.8 [32]. As shown in the figure, the algorithm search criteria follow a number of steps to find the optimal solution [33, 32, 34]. In the first step (1), the algorithm spreads the number of scout bees (n) randomly in the search space. In the second step (2), the fitness of the sites

visited by (n) are evaluated, with respect to the objective function, and ranked in ascending or descending order according to the optimisation target. In the next step (3), the bees with the highest fitness values are chosen as selected (m) sites and the bees visited by them are chosen for neighbourhood searches. However, the selected sites (m) are classified into two sub-groups: elite sites (e) and non-elite sites (m-e). Then, in steps 4 and 5, the algorithm conducts a neighbourhood search around the selected (m) sites by assigning more forager bees (nep) to search near to the (e) sites and fewer bees (nsp) to search near the (m-e) sites. According to this strategy, the search effort is concentrated on the best elite (e) sites, which represent a more promising solution. Together with scouting, this differential recruitment is a key operation of the Bees Algorithm.

In step six, for each patch only the bee with the highest fitness rank will be selected to form the next bee population. In step seven, the unselected remaining bees (n-m) in the population are assigned to perform a random (global) search around the search space scouting for new potential solutions that were not detected in the neighbourhood search process. This search step (7) shows that the algorithm can extend the search space without being trapped at local optima. However, at the end of each iteration, only the bees with the most promising solutions will be selected to form the next generation. These steps will be repeated until the stopping criteria are met.

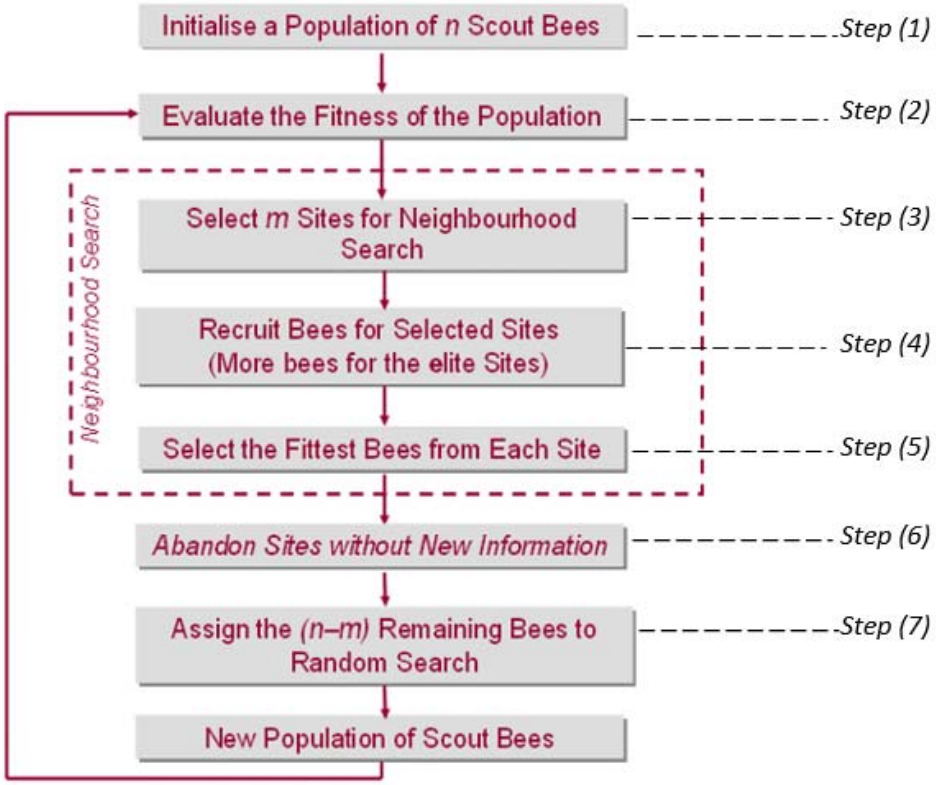

Figure 2.8 Flow chart of basic Bees Algorithm search criteria

From the aforementioned, it is shown that BA is able to perform a combination of both exploitative neighbourhood search (local search) and explorative global search. This indicates the strong ability of the optimisation to reliably handle complex multi-objective optimisation problems quickly and efficiently.

BA has been employed to search for optimal parameters in different discrete and continuous types of problems. It has been widely applied to solve many complex engineering and manufacturing optimisation problems, such as improving the size of stand-alone renewable hybrid energy systems [35] and solving power flow on large scale power systems [36]. Through these applications, BA has shown competitive performance and efficiency in solving constrained and unconstrained optimisation

problems. Although BA has been known since 1997, this thesis is the first published work applying the Bees Algorithm to the design of an electric machine.

2.4 Review of Recent Developments in Electrical Machine Design Optimisation Methods

With the general objective of producing an electric machine design at minimum cost and maximum efficiency, recently there have been significant developments on the algorithms search procedure. Electric machine design contains a large number of parameters and data, including rotor and stator dimensions, material properties, winding configurations, etc. The complexity of the design process and the non-linear relationship between these parameters definitely increases the search space of the optimisation problem. To reduce the solution search space, a surrogate models technique is utilised to reduce the number of variables in the machine. The surrogate models technique has been applied in the population-based optimisation algorithms to design either part or all electric machines [37, 38, 39, 40]. Some of the recent developments and progress in the design of electric machines using surrogate models are outlined and reviewed.

In order to reduce the search space and the effort of repetitive analysis in the optimisation process, the surrogate model technique was applied in [41]. The technique was aimed to approximate the relationship between major design input variables such as the spatial ratio between the stator inner diameter and the machine length. The method applies a statistical screening technique based on the stepwise multiple regression, aimed at approximating the relationship between major design input variables. The benefit of this screening is to determine the sensitivity between

main performance indices to the objective physical quantities, and output characteristics. The proposed technique was applied to the benchmark problem and design of Interior Permanent Magnet Synchronous Motor (IPMSM). The validation of applying the screening technique confirmed through comparison of the Pareto-front calculated by using the full set of decision variables and the Pareto-optimal solutions determined by means of fewer design variables.

Another technique aimed at reducing the optimisation search space by breaking the design processes into two-stage surrogate models, hence reducing the number of optimisation prime variables, was suggested by [42] and applied on surface-mounted permanent magnet synchronous machines SMPMSM to improve the torque density. In the first stage, a statistical analysis based on multiple correlation coefficients is used to render the application of the FEM simulation model feasible. At the second stage, an approximation method i.e. moving of least square (MLS) has been employed to make the surrogate model compatible with different swarm-based optimisation algorithms by applying the coefficient obtained from FEM.

Another similar screening technique was also adopted in [43] to design motor drive system for SMPMSM. This technique, based on correlation analysis, aims to solve the relation between the design variables, constraints and the optimisation objective functions. The design variables are classified according to their importance to the convergence improvements and allocated in multilevel optimisation problems. Thereafter, the variable at each level is encoded independently and assigned with multiple population and different dynamic genetic operators.

Using a surrogate model to optimise an electric machine, the designer needs to optimise the design with two main processes; firstly, he needs to reduce the search space by finding the relation between the input variables and their corresponding output characteristics, which is mostly achieved by using an analysis method such as FEM. The second step is to apply the optimisation algorithm to search in the reduced space search. This method needs a substantial programming effort to perform the two steps. However, the results from FEM are not generic: what is seen to be of benefit for one design could be detrimental for another design. In order to comprehend the search in the search space of an optimisation, the number of iterations and population of the optimisation algorithm should be compatible with the maximum and minimum boundaries of each prime variable. Thus, if the boundaries were very wide, the number of population and iterations should be large enough to cover the whole search space. Moreover, in some optimisations like Bees Algorithm, the designer can enhance the global or local search, or both of them, by assigning suitable optimisation parameters according to the optimisation problem. An illustration of how to tune the optimisation parameters is explained in detail in Chapter 6.

2.5 Chapter Summary

Electric machines design is a complex task and a comprehensive process consisting of electromagnetic, mechanical and thermal models that cannot be designed separately. The design of an electric machine contains a large number of parameters that in most cases have nonlinear relations. The target of an electric machine design usually involves multi-objectives that conflict with each other, such as weight, cost and efficiency.

In this chapter, the old, traditional method of designing electric machines has been reviewed. It is shown that this method has been mainly based on typical sizing equations and data from typical curves for a limited number of materials. It is also shown that the accuracy of the final machine parameters depends largely on designer experience, regardless of the application. However, with substantial improvement in magnetic materials, cooling strategies and power electronics, the traditional design method cannot be adopted to accurately design electric machines for modern applications.

An accurate design of an electric machine requires intensive computational processes that can connect between the different design models and compromise the design objectives. Swarm Intelligence, based on Swarm-Population Algorithm, is approved to be a multi-physic design tool that can rapidly and efficiently search for optimal design parameters for certain design requirements. In modern electric machine applications, optimisation algorithms are reliable in systematically considering the effects of power supply, machine controls, load profiles, thermal effects and materials on the output performance of the machine design.

Recently, for the design of electromagnetic systems, various optimisation strategies with different search criteria have been employed to search for optimal machine parameters. A brief description and key factors of the most widely applied optimisation tools, Genetic Algorithm (GA) and Particle Swarm Optimisation (PSO), have been illustrated in this chapter. A relatively new optimisation algorithm, Bees Algorithm BA recently developed at Cardiff University, has shown competitive performance and efficiency to solve single and multi-objective constrained and

unconstrained optimisation problems. It has received a number of improvements and is widely applied to solve many complex engineering and manufacturing optimisation problems.

BA can perform an exploitative neighbourhood local search combined with a random global explorative search. According to preliminary research, BA can offer certain advantages over the other optimisation methods, and hence may be a good candidate for electric machine design optimisation. Therefore, this research represents a novel application of Bees Algorithm in the design of electric machines.

3 Chapter 3: Analysis of magnetic circuit in BLPMSM

3.1 Background

The design of electric machines requires comprehensive knowledge of the quantitative and interrelation of the magnetic field in every part of the system, particularly the field distribution in the airgap region. In BLPM machines, the magnetic flux ϕ is established by permanent-magnet and linked with the armature winding to generate torque. Torque is proportional to the armature current I and the flux linkage ψ. Flux linkage and armature current are the key parameters to determine the characteristics of torque-speed curve in electric machines.

The fundamental magnetic concept is the vector of magnetic field density B. The electric current I that flows in the conductors or coils gives rise to magnetic fields. To define the relationship between these two magnetic fields and current, it is useful to introduce a new magnetic quantity i.e. magnetic field intensity H. The relation between these magnetic quantities is the magnetisation characteristics of the magnetic materials in which the magnetic field exists. To solve practical problems, this relation can be described in mathematical form as:

$$B = \mu H \tag{3.1}$$

$$\oint H.dl = \sum i \tag{3.2}$$

Where μ is the material permeability, $H.dl$ the integral of closed path and the summation on the right is the sum of all the currents enclosed by the paths.

3.2 Numerical methods for solution of static magnetic field

The problem of computing B for given H is a static magnetic field problem. In seeking an accurate solution for a magnetic field problem, an appropriate method has to be chosen. The most important method prescribed in [44] are listed as follows:

1. Finite Element Method (FEM)
2. Finite Difference Method (FDM)
3. Boundary Element Method (BEM)
4. Magnetic Equivalent Circuit (MEC)
5. Point Mirroring Method (PMM)

In computing the design of electric machines using evolutionary optimisation method, there are several key factors that must be addressed effectively to enable consideration of the significant large search space. The first of these factors is the type of underlying analysis. In order to evaluate the "fitness" function, it is necessary to accurately conduct a magnetic analysis of the machine. This may be done using analytical methods, magnetic equivalent circuit (MEC), finite-element methods (FEM) or a combination of both methods.

The second main factor that the optimisation must have is the ability to cover the optimisation search space, efficiently search for optimal parameters, and make trade-off between different machine designs within a reasonable computational time. A

large electric machine model includes more than 200 parameters linked by more than 100 equations. A change in the value of just one parameter affects the calculation of another parameter. Therefore, with this huge number of design variables and the complicated relationships between them, the computational time becomes an extremely significant challenge for this search.

From the aforementioned, it can be concluded that the most suitable optimisation method is the one that provides accurate results for non-linear problems with minimal computational effort. However, the characteristics of the above-mentioned analysis methods, in terms of geometric approximation and computational cost, are concluded in Table 3.1

Table 3.1 Characteristics of analysis methods in terms of geometric approximation and computational cost

Method	Geometry approximation	Non-Linearity	Computational Costs
FEM	Extremely flexible	Possible	High
FDM	Inflexible	Possible	High
BEM	Extremely flexible	Troublesome	High
MEC	Specific geometries	Possible	Very Low
PMM	Simple geometries	By constant factor	Low

3.2.1 Finite Element Method FEM

FEM is a procedure for approximating an electromagnetic field by means of numerical algorithms. The algorithm is based on partial differential equations of a continuum domain that is discretised into a finite number of parts known as elements. It has been widely used in many engineering disciplines such as the analysis of structures, solids,

electromagnetics, heat transfer and fluids. As shown in Table 3.1, FEM has extreme flexibility in approximating geometries and high possibility in solving non-linear problems; it has been applied to analyse electric machines to improve performance and efficiency. On the other hand, when using evolutionary optimisation, due to the high computational effort, the FEM cannot be considered an efficient tool to design electric machines. Instead, FEM represents a good choice to explore magnetisation behaviour of certain material shapes or to verify obtained results for magnetic problems.

In [45], the FEM has been employed to determine the optimum shape and magnetisation of a set of discrete anisotropic magnet blocks or arcs in permanent magnet synchronous machines. Also FEM has been used in [46] to find the optimal shape for permanent magnet and improve efficiency. However, in both cases, the design parameters have been given first to the FEM before it carries out the analysis. Therefore, FEM is a very reliable and powerful analysis technique to simulate electric machine designs and predict their performance.

With the development of faster computers, much commercial software was improved based on FEM to provide reliable 2D and 3D analysis tools. Since it is not restricted by size, FEM is very efficient and can be applied to any geometry or set of material properties and loading conditions.

3.2.2 Magnetic Equivalent Circuit (MEC)

Magnetic Equivalent Circuit MEC is an analytical approach based on equations used to determine the values of each element in an electromagnetic network. These values are used to approximate the magnitude of different magnetic quantities, such as the

fundamental flux density in the airgap and maximum flux densities in different parts of the motor.

Since the very beginning, MEC has been the principle design tool for electric machines. The MEC consists of a large set of equations that link between the different models of electric machine design, such as electrical, magnetic, thermal and mechanical equations. Using MEC, the input of certain design variables can be initialised directly from the designer or randomly from optimisation algorithm to calculate the parameters and other variables in the design.

Although the traditional approach of MEC is to study the steady-state magnetic properties, the steady-state flux distribution and magnitude can also be achieved by assigning non-linear properties of the magnetic materials.

The MEC has a good accuracy and very low computational effort; hence, it is suitable to be employed in optimisation processes. The challenge of using MEC in the optimisation is the large number of design variables and the complicated relationship between them. MEC has been integrated into the optimisation set to search for hundreds of optimal parameters for different types of motor design and various applications. Considerable research has been published on improving the accuracy of MEC, such as the consideration of magnetic saturation, core loss resistance, inductance profile according to amplitude of line current and current angle and the variation of no-load linkage flux [47, 48, 49, 50].

3.2.3 Finite difference method FDM

This is the oldest known numerical strategy for computing magnetic fields. It is based on rectangular meshes and nodes drawn around the area being computed. The Maxwell's differential equations for magnetic potential at the nodes are replaced with a system of linear difference equations that are solved iteratively until convergence occurs at various nodes. Due to the networks of rectangular meshing, the method involves a large number of equations that results in high computational cost. It is also inflexible in handling complex geometries, which makes it an inappropriate method to be considered in an electric machine that is based on evolutionary optimisation.

3.3 Magnetic Circuit Analysis

The rapid development of permanent-magnet material has been reflected in many industrial areas by replacing induction motors with permanent-magnet machines that benefit from higher efficiency and smaller size. The choice of permanent-magnet grades and techniques to utilise the maximum power from these materials requires in-depth knowledge of how they behave in the electric machine system. Therefore, it is wise to study the behaviour of permanent magnet material before commencing on the analysis of magnetic circuit.

3.3.1 Characteristics of Permanent Magnet Material

The characteristics of permanent-magnet material can be expressed graphically by plotting the practical relation between the magnetic output B measured in Tesla (T) and the magnitude of an external applied field, magnetic field intensity H measured in (A/m) of a magnetic material. The plot is located in the upper left-hand quadrant,

called the demagnetisation curve as shown in Figure 3.1. The curve provides specific information of how a given material can practically operate and how it withstands under of magnetic loading conditions. It should be noted here that the curve is representative of the specific magnet material properties and independent of the dimension of the magnet.

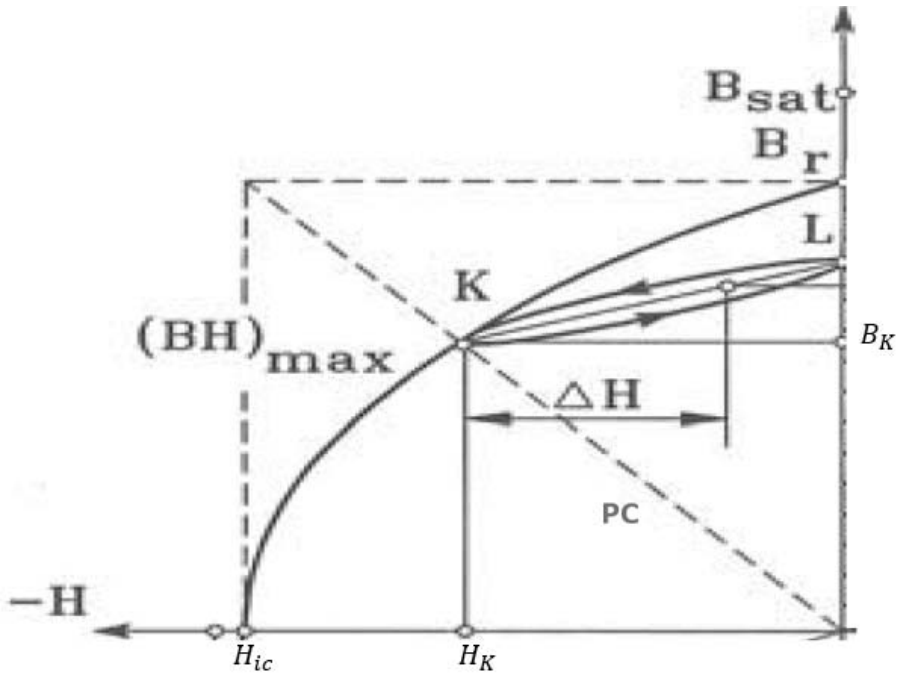

Figure 3.1 Second quadrant "demagnetisation curve" of full hysteresis loop for a permanent magnet material

With no current in the phase winding, the magnet operates on the intrinsic demagnetisation curve with intrinsic magnetic flux density B_r and intrinsic coercivity H_{ic}. However, when current is applied to the phase winding, the magnetic flux density reduced below B_r at the point L. When the reversal magnetic field intensity is removed, the magnetic flux density B returns to the point L according to a minor hysteresis loop. The magnet operation point generally moves reversibly up and down within the minor hysteresis loop. The minor hysteresis loop is usually replaced

by a straight line called the recoil line. The slope of the recoil line is called the recoil permeability μ_{rec}.

The operating point of magnetic material is the intersection of the load line, also known as Permeance Coefficient PC, with the intrinsic curve. As long as the negative field intensity does not exceed the maximum value corresponding to point K, the magnetic flux density recovers and the permanent-magnet is regarded as being reasonably permanent. If the applied negative magnetic field intensity is greater than K, a new and lower recoil line will be established upon removing H. The general relationship between magnetic flux density B, intrinsic magnetic flux density B_i and the magnetic field intensity H can be expressed as (3.3)

$$B = \mu_0 H + B_i = \mu_r \mu_0 H \tag{3.3}$$

Another important factor in the BH curve is the maximum energy product $(BH)_{max}$. This term is commonly used to rate materials for maximum energy output per unit volume (kJ/m^3). The material with greater energy product does not indicate better performance of that material; instead, it expresses the maximum energy that can be held by the permanent-magnet when the BH hyperbola is tangential with the recoil line.

Another important factor that affects the magnet operating point is temperature. Both remanent magnetic flux density B_r and magnetic coercivity H_c are temperature dependent, with the relation referred to as the reversible temperature coefficient following classical relation, as follows:

$$B_r(T) = B_{r(20)}[1 + \alpha_{Br}(T - 20)/100] \tag{3.4}$$

$$H_c(T) = H_{c(20)}[1 + \alpha_{Hc}(T - 20)/100] \tag{3.5}$$

Where $B_{r(20)}$ and $H_{c(20)}$ are the values of B_r and H_c at 20˚C. The symbols α_{Br} and α_{Hc} are the reversible temperatures coefficient of B_r and H_c respectively.

From the foregoing, it can be concluded that most suitable permanent-magnets are those having high-energy and a straight demagnetisation curve that is close to the theoretical maximum. Therefore, it is important to choose the proper permanent magnet material in an electric machine, as it has influence on the torque and power density. Among the permanent magnet materials, the rare-earth permanent magnets: Samarium Cobalt (SmCo) and Neodymium Iron Boron (NdFeB) are considered to be the best grades. This is due to the high ability of these materials to store large amounts of magnetic energy to operate, as well as their high coercivity, allowing for small size application. Table 3.2 shows a general overview of select permanent magnet materials and addresses their characteristics.

Table 3.2 Properties of typical permanent magnet materials

Magnet Material	**Br (T)**	**Hc (kA/m)**	**BH_{max} kJ/m^3**	**Max operating Temp. ˚C**	**α_{Br} %/˚C**	**Resistance to demagnetisation**
NdFeB (42/15)	1.3	1011	335	150˚C	-0.1	Very High
SmCo 18/30	0.87	2387	140	300˚C	-0.03	Very High
Alnico	0.82	51	79	550 ˚C	-0.02	Low
Hard ferrite (Ceramic)	0.4	255	31	300 ˚C	-0.2	Moderate

3.4 Magnetic Circuit analysis

As mentioned earlier, temperature and applied current directly affect the operating point of a permanent magnet and consequently the overall machine performance. In electric machines, the performance of the magnetic system is highly dependent upon

the airgap flux density; which is in turn affected by the location, shape and magnetisation direction of the permanent magnet in the rotor. Therefore, this section will be dedicated to explaining how to determine the magnetic flux density in different parts of the motor components.

The simplest way to evaluate the magnetic flux densities is to study the magnetic flux circulation based on a non-linear reluctance network. Such networks have been proven accurate to analyse the flux behaviour for different rotor configurations [51]. Also, the computational effort to solve reluctance network is very low; hence, it is highly suitable for integration in an optimisation algorithm.

To study the magnetic flux in a magnetic circuit network, the magnetic circuit is considered as an analogy to an electric circuit. In the magnetic circuit, the magnetic flux ϕ is equivalent to current I, the magnetic reluctance $\mathcal{R}$ is equivalent to resistance R and the magnetomotive force MMF is equivalent to voltage V. In the reluctance network, the relation between these parameters is computed as (3.6)

$$MMF = \emptyset . \Re \tag{3.6}$$

Ampere's law states that the line integral of the magnetic field intensity H taken around any closed loop is proportional to the total current passing through any area enclosed by that loop. Mathematically, this statement can be written as (3.7)

$$\oint H . dl = i \tag{3.7}$$

According to Gauss's law, also known as flux conservation principle for magnetism, for any closed region, the total magnetic flux within a magnetic circuit entering this region is equal to total flux leaving this region. This principle is expressed as (3.8)

$$\oint B . dA = 0 \tag{3.8}$$

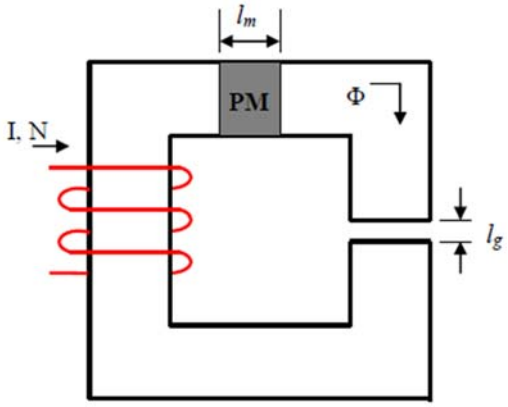

Figure 3.2 Simple magnetic circuit with permanent magnet

Figure 3.2 shows a simple magnetic circuit comprised of permanent-magnet, steel, and applied current. The magnetic flux generated from the permanent-magnet will travel from one steel pole piece and pass through the airgap to reach the other steel pole piece. In unsaturation conditions, the magnetic permeability of the steel is thousands times the magnetic permeability of the air $\mu_0 = 4\pi\times10^{-7}$; therefore, the magnetic permeability of the steel is assumed to be infinite. Assuming no flux leakage in the magnetic circuit, at no-load condition the magnetomotive force MMF is generated only by the permanent magnet. The total flux passing through the magnet must be equal to the total flux through the airgap and the MMF drop around the magnetic circuit is equal to 0.

$$\oint H.dl = \sum I \xrightarrow{\textbf{no-load}} H_m.l_m + H_g.l_g = 0 \tag{3.9}$$

$$B_m.A_m = B_g.A_g \tag{3.10}$$

Where A is the area and l is the flux path length in the direction of magnetisation. The subscripts m and g deal with permanent magnet and airgap respectively.

However, at load condition $I \neq 0$, the current flows in the armature winding. According to ampere law, the line integral of magnetic field strength or intensity taken around any closed path is proportional to the total current flowing across any area bounded by that path. Therefore, from ampere's law and conservation of flux, at load condition equation of balanced MMF (3.9) is replaced with (3.11)

$$\oint H.dl = \sum I \quad \xrightarrow{\boldsymbol{load}} \quad H_m . l_m + H_g . l_g = N . I_a \tag{3.11}$$

Where N the number of turns per coil and I_a is the armature current.

If we keep assuming infinite permeability of steel laminations, the permanent-magnet flux density B_m is given as (3.12)

$$B_m = \mu_r \mu_0 \frac{A_g}{l_g A_m} (-H_m . l_m) \tag{3.12}$$

This equation represents the load line as shown in Figure 3.1, also known as permeance coefficient line. The linear approximation of the demagnetisation curve, shown as an intrinsic curve in Figure 3.1, is

$$B_m = B_r + H_m \mu_r \mu_0 \tag{3.13}$$

The slope of the normal curve is $\mu_r \mu_0$ from Equation (3.13). Therefore, the actual flux density from the permanent magnet at load condition is the result of combining Equations (3.11) with (3.12) and compensating the value (3.14)

$$B_m = \frac{l_m A_g B_r}{\mu_r l_g A_m + l_m A_g} + \frac{\mu_r \mu_0 A_g}{\mu_r l_g A_m + l_m A_g} N I_a \tag{3.14}$$

However, the magnetic intensity for the permanent magnet on the BH curve

$$H_m = \frac{B_r}{\mu_0 \mu_r} \left[\frac{1}{\mu_r l_g + l_m} - 1 \right] + \frac{N_a I_a}{\mu_r \, l_g + l_m} \tag{3.15}$$

For operating an electric machine, the amount of demagnetisation is determined by the intersection point between the load line and the demagnetisation curve. When the current flows in the armature winding, the second term of Equation 3.14, an opposite magnetic field from the armature will be present and cause a distortion of the magnetic field set up by the permanent magnet; the larger the stator current, the larger the distortion. Thus, the amount of H_m is shifted from the origin to the left in Figure 3.1 and the magnetic flux density is reduced. This effect is known as armature reaction field.

However, if the current is increased above the maximum permissible value e.g. at abnormal operating conditions, this results in moving the operating point further to the left. If the load line is past the nonlinear point H_k as shown on Figure 3.3, also known as knee point, an additional field will be applied and cause partial or total demagnetisation for the permanent magnet.

In electric machine design, to keep the operation within a safe range, it is the designer's responsibility to estimate the worst demagnetisation condition and decide the thickness of the permanent magnet that is associated with the maximum marked demagnetisation conditions.

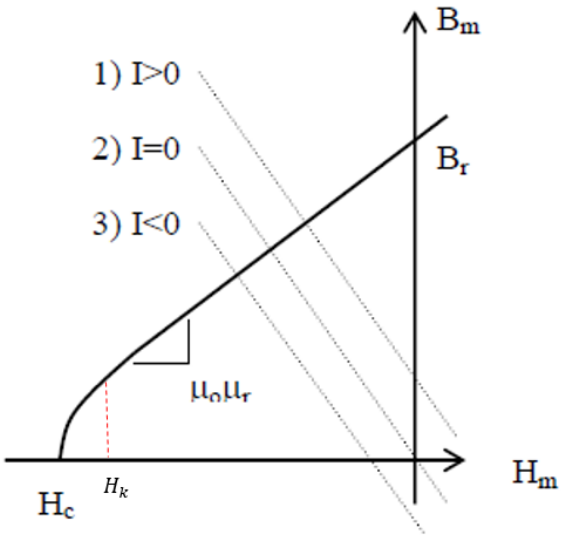

Figure 3.3 Demagnetisation curve of permanent magnet material

3.4.1 Magnet Circuit of Permanent Magnet Synchronous Motor PMSM

In an electric machine, the permanent magnet is considered as a flux source. The flux paths, and their contribution in energy conversion, should be assigned in the surrounding airgap, rotor core and stator core. Figure 3.4 shows the magnetic flux distribution in surface mounted permanent magnet rotor. As shown in the figure, the flux produced from the permanent magnet is divided mainly into two parts: flux circulating through the stator and linking the armature winding to participate in the energy conversion i.e. flux linkage ψ. The other part of flux is the leakage flux ϕ_l, inside the dotted circles, that flows in the rotor back iron, airgap and between the magnet poles without linking with the armature winding. This flux can cause a substantial effect on the useful magnetic flux and degrade machine performance. To accurately evaluate flux density in the airgap, both paths of flux must be considered.

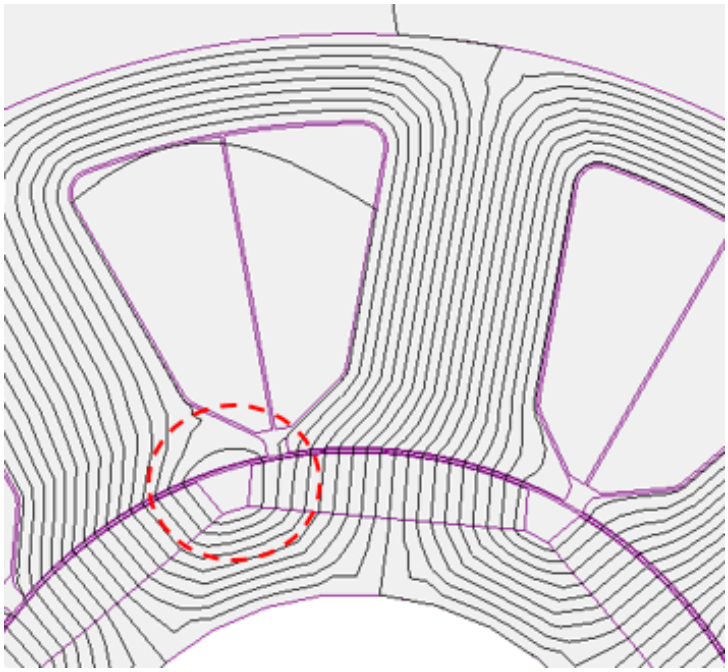

Figure 3.4 Magnets flux line using FEM: observation of magnetic leakages in the rotor.

Generally, the equivalent magnetic circuit EMC is affected by the rotor configuration and magnetisation direction. Therefore, there are several types of magnetic circuit available. In this section, equivalent magnetic circuits for rotors with surface mounted permanent magnet SMPM will be studied to calculate the value of airgap flux density.

3.4.2 Equivalent Magnet Circuit of Surface-Mounted Permanent Magnet SMPM

Motors with surface mounted permanent magnet on the rotor are the most widely used topology of brushless permanent magnet machines. This is due to their simple structure and low manufacturing cost. Figure 3.5 shows a schematic diagram of magnetic flux distribution under open circuit conditions for one-pole section, half N-pole and half S-pole. In the circuit, the actual flux generated from the permanent magnet ϕ_m travels from the N-pole through the airgap to stator teeth and yoke cross the airgap again before it goes back to the S-pole and the rotor steel to complete the

closed-loop circuit. The schematic diagram also shows that some other magnetic flux i.e. flux leakage ϕ_l has passed through the airgap, but without linking with the phase winding.

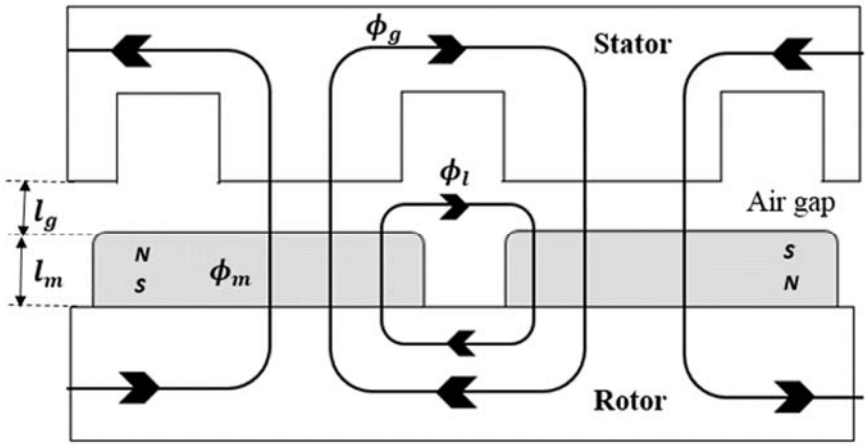

Figure 3.5 Schematic diagram of magnetic flux path for PM synchronous motor

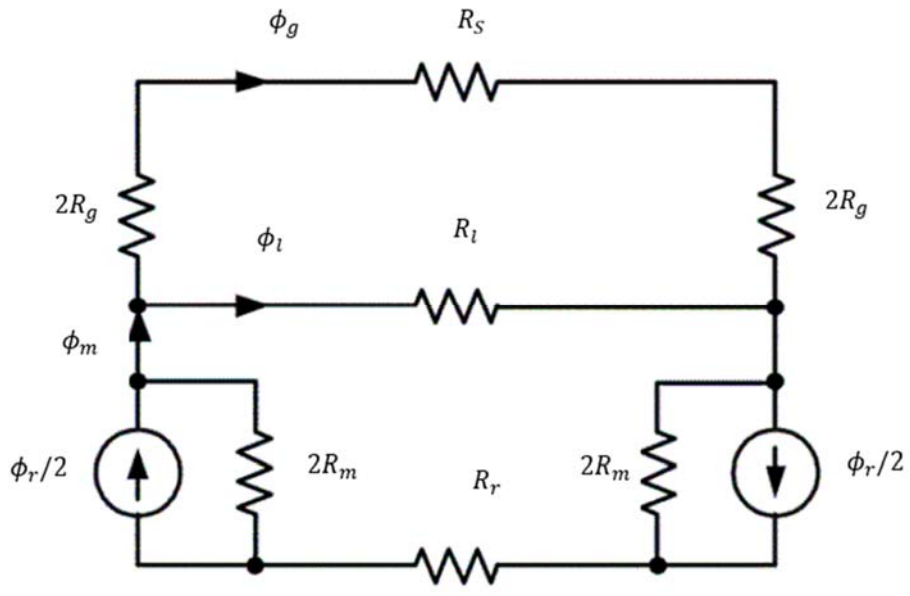

Figure 3.6 Complete Magnetic Equivalent circuit for one pole of SMPM motor

Figure 3.6 shows the equivalent magnetic circuit for the schematic diagram in 3.5, where $\Re_m, \Re_g, \Re_l, \Re_S, \Re_r$ are the equivalent reluctance that represents the MMF drop on the magnet, airgap, leakage flux, stator lamination and rotor steel respectively.

$$\Phi_m = \Phi_g + \Phi_l = \frac{4\Re_m}{4\Re_m + 4\Re_g + \Re_l + \Re_S + \Re_r}\ \Phi_r \tag{3.16}$$

Considering the leakage reluctance $\Re_l$, stator-yoke reluctance $\Re_S$ and rotor reluctance $\Re_r$, at this stage of the analytical model, the exact values needed to determine their reluctance values are unknown. As mentioned earlier, the magnetic permeability of the steel is thousands of times that of the air and, therefore, the reluctance is, comparatively, very small. Hence, in small electric machines, these reluctances are completely omitted. However, in an electric machine of large size, neglecting the reluctances in stator and rotor laminations can result in an inaccurate approximation of the airgap flux density. Therefore, a reluctance factor, having its value chosen to be a constant slightly greater than unity, has to be considered in the analytical procedure to compensate the MMF drops in the stator and rotor steel. The value of the reluctance factor depends mainly on the machine size with typical value ranges between (1.0 – 1.2) to multiply the R_g [52]. Thus, the Equation (3.16) can be simplified for single external reluctance i.e. $\Re_g$ and re-written as (3.17)

$$\Phi_m = \frac{4\Re_m}{4\Re_m + 4\Re_g}\ \Phi_r \tag{3.17}$$

By Gauss's law, the total flux generated from the permanent magnet ϕ_m is given by

$$\phi_m\ = \phi_g + \phi_l$$

$$\Rightarrow \qquad \Phi_m = \phi_g + \phi_l = \frac{\Phi_r}{1 + P_{m0}\Re_g} \tag{3.18}$$

Where P_{m0} is the internal magnet permeance equal to

$$P_{m0} = \frac{\mu_0 \mu_m A_m}{h_m} \tag{3.19}$$

Furthermore, the leakage flux ϕ_l can also be considered as a ratio of flux generated from permanent magnet to that flux passed through the airgap. This is known as the leakage coefficient f_{LKG} and is expressed mathematically as Equation (3.20).

$$f_{LKG} = \frac{\phi_g}{\phi_m} = \frac{\phi_g}{\phi_g + \phi_l} \tag{3.20}$$

Leakage flux ϕ_l causes a substantial reduction effect on the useful magnetic flux. The leakage coefficient depends on the distance between magnet pieces and the rotor configuration with a typical value range between (0.9 - 1.0) [53]. With this assumption for leakage coefficient f_{LKG}, the complete EMC can be eliminated to appear as shown in figure 3.7.

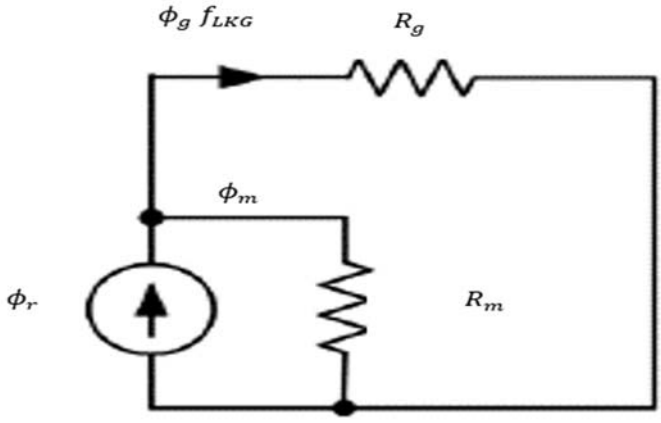

Figure 3.7 Simplified Model for Equivalent Magnetic Circuit for SMPM motor

And Equation (3.18) can be re-written to include the new coefficient f_{LKG} as

$$\Phi_m = \frac{\Phi_r}{1 + f_{LKG} P_{m0} \Re_g} \tag{3.21}$$

And from Equation (3.20) $\phi m = \phi g / fLKG$. Equation (3.21) can be rearranged to give

$$\Phi_g = \frac{f_{LKG} \cdot \Phi_r}{1 + f_{LKG} P_{m0} \Re_g} \tag{3.22}$$

Given that

$$\Phi_g = B_g A_g \tag{3.23}$$

And

$$\Phi_r = B_r A_m \tag{3.24}$$

Equation (3.22) an be rearranged to

$$\mathrm{B}_g = \frac{f_{LKG} \frac{A_m}{A_g} . \mathrm{B}_r}{1 + f_{LKG} P_{m0} \Re_g} \tag{3.25}$$

Finally, compensate the values of P_{m0} from 3.19 and $\Re_g$

$$\Re_g = \frac{g}{\mu_0 A_g} \tag{3.26}$$

Equation (3.25) can be rearranged to give

$$\mathrm{B}_g = \frac{f_{LKG} \frac{A_m}{A_g} . \mathrm{B}_r}{1 + \frac{f_{LKG} . g . \mu_m A_m}{A_g . h_m}} \tag{3.27}$$

At this stage, it is assumed that the values of stator inner diameter D, the thickness of permanent magnet h_m, the axial length of the machine L, and the airgap thickness g are known or have been initialised randomly from the optimisation search space.

However, considering the slotting effects on the stator, the effective length of the airgap g' should be determined using Carter's coefficient k_c. To calculate Carter's coefficient, an appropriate value for the slot opening B_{so} and the equivalent airgap length g_{eq}, consider the MMF drop on the permanent magnet and its relative permeability μ_m i.e. $g_{eq} = g + h_m/\mu_m$. However, the choice of B_{so} value depends primarily on the manufacturing method of stator lamination and the diameter of the winding conductors. The ratio of the slot opening width B_{so} to the effective airgap is usually small, a typical value being around 1.01. Therefore, the effect of the stator slotting on the calculation of the flux per pole is normally negligible; the exception being when a large slot-opening is used to reduce the cogging torque, as in [54]. On the other hand, a small value of B_{so} leads to higher fundamental flux density, but at the same time increases the leakage flux [54]. However, for small and medium size machines (about 1 kW to 100 kW), past experience shows that 2-3 mm is usually chosen. Thereafter, the Carter's coefficient k_c can be expressed as

$$k_c = \frac{\tau_s}{\tau_s - \gamma . g_{eq}} \tag{3.28}$$

Where τ_s is the tooth pitch that is equal to

$$\tau_s = \frac{\pi . \mathrm{D}}{N_m} \tag{3.29}$$

Where N_m is the number of slots in the stator and γ is expressed as

$$\gamma = \frac{4}{\pi}\left[\frac{B_{so}}{2\,g_{eq}}\tan^{-1}\left(\frac{B_{so}}{2\,g_{eq}}\right) - \ln\sqrt{1+\left(\frac{B_{so}}{2\,g_{eq}}\right)^{2}}\right] \tag{3.30}$$

And the effective airgap g'

$$g' = g \times k_c \tag{3.31}$$

Furthermore, SMPM machines are reported to have relatively high torque pulsations [55, 56], which are composed of cogging torque and torque ripple. The main source of these undesirable components is a substantial change in the distribution of the airgap flux density [57]. Reducing the torque ripple in PMSM has received significant attention from researchers in recent years [58, 59, 60]. Concerning cogging torque reduction, numerous methods have been proposed, such as fractional number of slots per pole, skewing, notching and magnet shifting or a combination of these methods. However, a general solution that aims to reduce harmonic distortion, and therefore torque ripple and cogging torque, can be achieved by optimising the magnetic pole coverage α_p. Hence, choosing a suitable value for α_p to reduce the torque pulsation will minimise the focus on machine geometries in the optimisation problem, as well as reduce the search space of the optimisation. The α_p defines as the ratio of the magnet-pitch to the total pole-pitch and has a value between 0 and 1.

$$\alpha_p = \frac{\tau_m}{\tau_p} \tag{3.32}$$

Using this approach, the magnet area A_m can be defined as a percentage of the airgap area A_g

$$\alpha_p = \frac{A_m}{A_g} \tag{3.33}$$

According to the previous definition for Carter's coefficient k_c and magnetic pole coverage α_p, Equation (3.27) can be rewritten as

$$\mathrm{B}_g = \frac{f_{LKG} \,.\, \alpha_p \,.\, \mathrm{B}_r}{1 + \frac{f_{LKG}.\, g'.\, \mu_m.\ \alpha_p}{h_m}} \tag{3.34}$$

From Equation (3.34) we note how f_{LKG} reduces the airgap flux density compared to the value it would have if there were no leakage. The corresponding magnet flux density is determined as

$$B_m \ = \frac{B_g}{f_{LKG}.\, \alpha_p} \tag{3.35}$$

In Equation (3.34) B_g is the rms value determined from the sinusoidal flux distribution in the airgap. Therefore, by Fourier analysis the first harmonic of the airgap flux density $B_g(1)$ distribution is

$$B_g(1) = \frac{2}{\pi} \int_{-0.5\alpha\pi}^{0.5\alpha\pi} B_g \cos\alpha d\alpha \ = \ \frac{4}{\pi}\, B_g \, sin\left(\frac{\pi.\, \alpha_p}{2}\right) \tag{3.36}$$

4 Chapter 4: Evaluation and analysis of benchmark BLPMSM

4.1 Background

This chapter provides an assessment of a benchmark motor designed to meet the requirements of driving a small electric vehicle EV. The component geometries, material properties, and electromagnetic parameters of the benchmark design will be given and the model of the design will be simulated and evaluated using FEA analysis.

The characteristics of the benchmark motor in terms of weight, volume and efficiency will be evaluated. In the next chapter, Bees Algorithm BA will be employed to search for alternative optimal dimensions and parameters that can match the same level of output power with lower weight, volume and higher efficiency. The optimal dimensions and parameters generated from the BA will be analysed and verified on FEA analysis. The objectives of the new optimised design generated from BA will be evaluated and compared with the benchmark design in Chapter 7.

4.1.1 Specifications and materials of benchmark motor

The benchmark motor has been designed by "Electronica Products Limited, UK" to be used for traction applications. The design has a classic three-phase star connected winding in the stator and surface-mounted permanent magnet on the rotor to develop

1.75 kW at 640rpm. The topology of the benchmark motor and explanation of motor dimensions are given in Figures 4.1 and 4.2 respectively. The values of the main geometrical dimensions of the stator and rotor are given in Table 4.1.

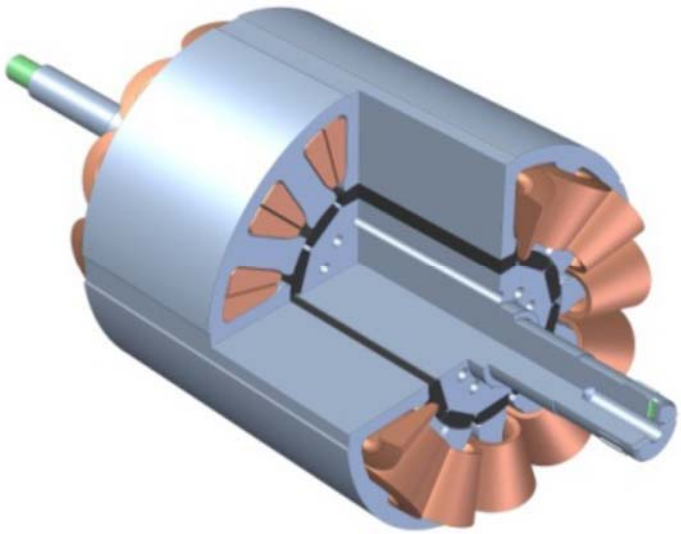

Figure 4.1 Model of the benchmark Motor

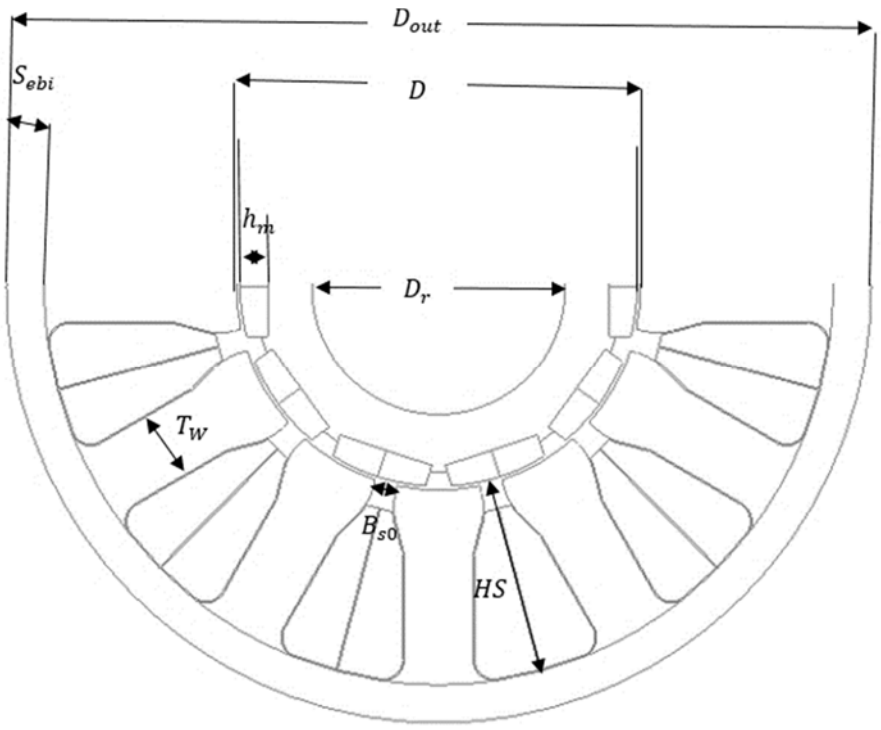

Figure 4.2 Explanation of motor dimensions

Table 4.1 Specifications and dimensions of benchmark motor

Parameter	Description
Number of Slots, Nm	12
Number of Poles, Np	10
Stack length, L [mm]	114
Stator inner diameter, $\boldsymbol{D}$, [mm]	58.3
Stator outer diameter $\boldsymbol{D_{out}}$, [mm]	124.9
Air Gap, g [mm]	0.5
Stator Slot Depth, Hs [mm]	27.85
Stator Tooth Width, $\boldsymbol{T_w}$, [mm]	10
Stator Slot Opening, $\boldsymbol{B_{s0}}$, [mm]	3.3
Magnet Thickness, $\boldsymbol{h_m}$, [mm]	4
Magnet base width, $\boldsymbol{w_m}$, [mm]	14
Rotor inner diameter, $\boldsymbol{D_r}$, [mm]	25
Turns per phase, $\boldsymbol{N_{ph}}$	352
Nominal Wire OD [mm]	0.9
Total mass [kg]	7.92
Volume [Litre]	1.64

The volume and weight of the motor are given in Table 4.1. The motor weight refers to the machine active materials that consist of the stator and rotor steel laminations, copper of stator winding and permanent magnet material only. The materials used for the machine are given in Table 4.2. Using these descriptions for weight and volume, the total mass of the benchmark motor is 7.92 kg and the power density, power-to-mass ratio, using the active material is 0.221 kW/kg.

Table 4.2 Materials and mass for the benchmark SMPM machine design

Component	Material	Mass [kg]	Percentage of total weight [%]
Stator core	M330-35A	4.99	63
Rotor core	M330-35A	0.72	9
Permanent magnet	NdFeB 230/220h	0.53	6.7
Copper	5.77e7 S/m	1.68	21.2
Insulation material	Class H	--	--

The volume calculation includes a simple cylindrical where the diameter is the outer diameter of the stator and a length taken over the axial end-turn of the winding. With an allowance of 10 mm made for each end-winding length around each tooth, the volume is 1.64 Litres which yield to power-to-volume ratio of 1.067 kW/Litre.

The winding of the benchmark motor uses 0.9mm wire diameter, which is equivalent to standard wire size of (19 AWG), formed as a multi winding as 88 turns per conductor, so with four conductors per phase the total number of turns per phase N_{ph} is 352. Using slot dimensions as shown in Figure 4.3 and wire size, the fill factor was determined as 0.36.

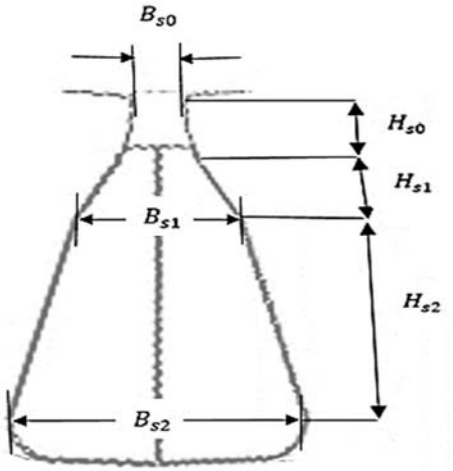

H_{s0}	3.5
H_{s1}	4.0
H_{s2}	20.0
B_{s0}	3.3
B_{s1}	7.5
B_{s2}	19.8

Figure 4.3 Slot design and geometries of the benchmark motor

At a room temperature of 20˚C, the phase resistance R_{ph} was determined as 2.7Ω.

According to the given properties of the insulation materials Class-H, the winding temperatures is expected to rise to 140˚C as shown in figure 4.4. where it will be safe to keep their life for 20 years. Therefore, with copper reversible temperature coefficient α_{Cu} of 0.00386 $/C^{\circ}$, the R_{ph} will rise to 3.95 Ω at a temperature of 140˚C.

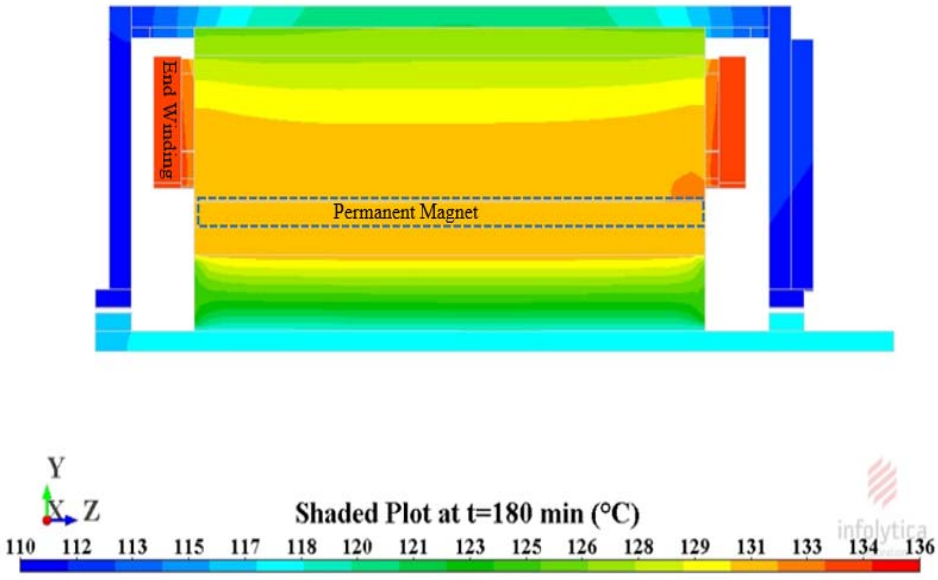

Figure 4.4 Thermal analysis benchmark design

However, under extreme steady state conditions the magnet is expected to rise to about 140˚C, as shown in Figure 4.4. This means the permanent magnets must be assumed to have stabilised after reaching this temperature; so, the magnet cannot be demagnetised. The permanent magnet grade employed in the benchmark design was NdFeB230/220h and the properties of this material, as provided by the supplier MS Schramberg, are given in Table 4.3. At 20˚C temperature, the remanence B_r is 1.16 T. Thus, as the temperature rises to 140˚C, the magnetic parameters fall below the room temperature level and B_r and H_c decline at the rate of the reversible temperature

coefficients. This suggests that under operating temperature 140˚C, with reversible temperature coefficients of -0.08 and -0.5, the actual remanence and coercivity fall to 1.05 T and 771 kA/m respectively.

Table 4.3 Properties of permanent magnet material NdFeB 230/220h

Parameter	**Description**
Remanence B_r [T], at 20˚C	1.16
Coercivity H_c [kA/m], at 20˚C	890
Relative permeability μ_r	1.1
Temp. Reversible coeff. of Br α_{Br} [%/K]	-0.08
Temp. Reversible coeff. of Hc α_{Hc} [%/K]	-0.5

The characteristics of the demagnetisation curve as shown in figure 4.5, shows that NdFeB 230/220h has a high intrinsic coercivity H_{ci} that is sufficiently able to provide linear demagnetisation throughout the second quadrant up to almost 150˚C. This is a basic technique to exhibit that the magnet ought to hold its fully magnetised state over its operating temperature range.

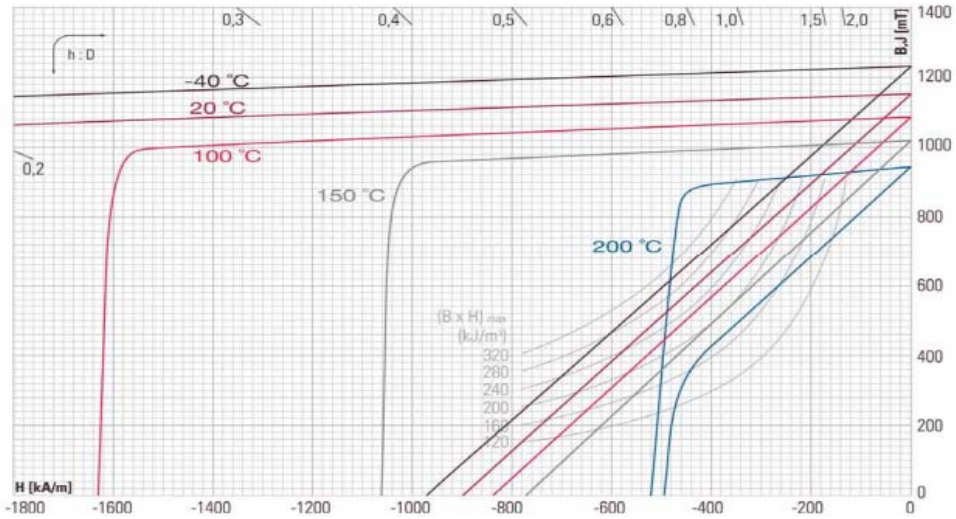

Figure 4.5 Demagnetisation characteristics of NdFeB 230/220h grade

The stator of the benchmark motor is designed with non-oriented electrical steel M330-35A of lamination of 0.35mm thickness; data on this specific grade and thickness material are given in Table 4.4. Iron losses P_{core} can be computed at any speed and for any peak magnetic field (B) experienced at any place in the core using material specific parameters an expression of the form:

$$P_{core} = k_h f^{\alpha} B^{\beta} + k_{ec} (fB)^2 \quad (4.1)$$

Table 4.4 Properties of core material M330-35A

Parameter	Description
Hysteresis loss coeff. k_h	0.00754373
Eddy current loss coeff. k_{ec}	3.11e-5
Parameter α	1.295
Parameter β	1.796

The magnetisation characteristics of M330-35A are shown in Figure 4.6. From the B-H curve, the knee point value is just around 1.35T.

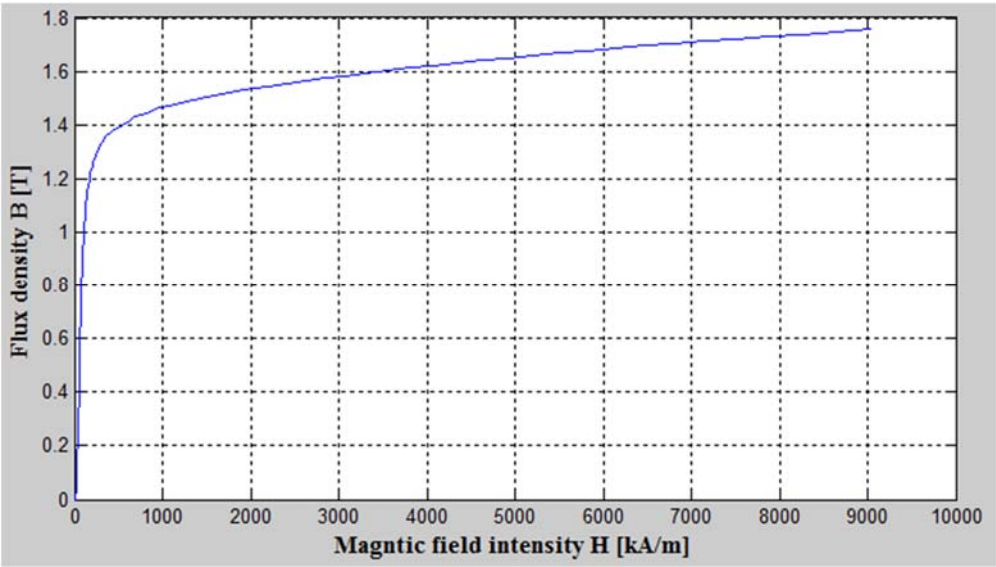

Figure 4.6 Magnetisation characteristics of M330-35A

4.2 Ideal performance benchmark motor

Generally speaking, electric machines designed for traction applications are required to develop a constant-torque region at low speed and a constant-power region at high speed. The continuous torque at low speed is dictated by the maximum slope specified for hill climbing, while the continuous power determines the maximum cruising speed of the vehicle. Intermittent overload for short durations is required for vehicle accelerations at any speed.

The benchmark motor has been designed to operate at maximum speed of 2400 rpm. This means that the motor should develop 1.75 kW through the Constant Power Region CPR from 640 to 2400 rpm and 26.1 N.m at Constant Torque Region CTR below 640 rpm. Accordingly, the ideal characteristics of the torque-speed required for the motor can be graphically drawn as in Figure 4.7.

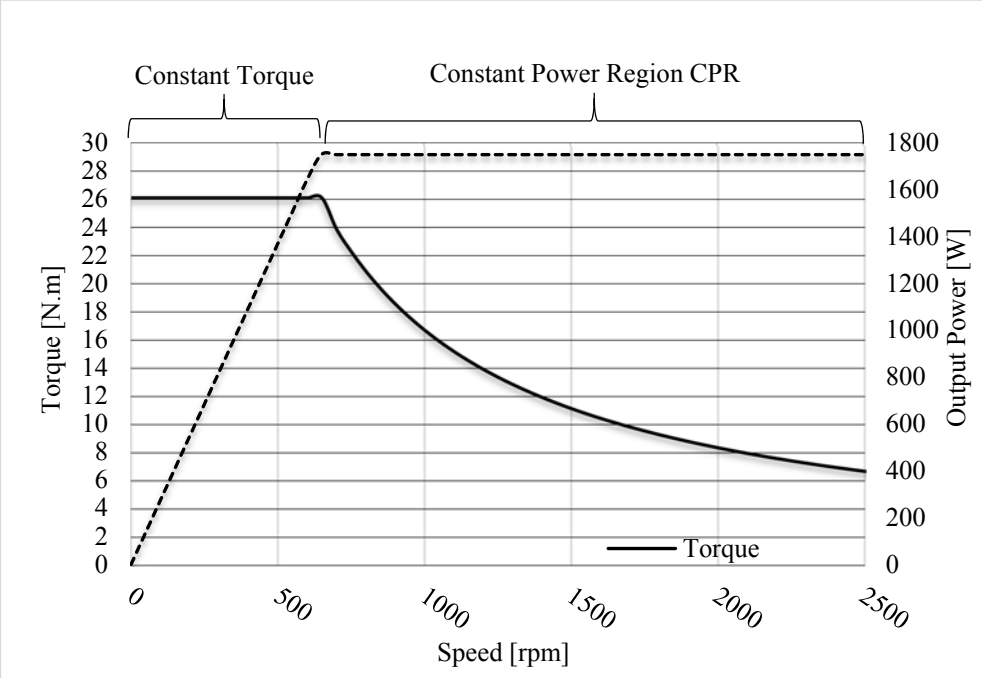

Figure 4.7 Ideal torque-speed characteristics required for benchmark Motor

Constant power operation over a wide speed range is desirable in many applications, such as electric vehicle drives, machine tool spindles and hand tools. In an electric machine for traction applications, the constant power-operating region ideally ranges between 3-4 times the base speed [5]. However, many solutions have been introduced to extend the CPR, including adopting control strategies such as scale and vector flux-weakening control, enhancing the power capability by employing a dc-dc voltage booster, such as that employed in the Toyota hybrid system [61]. Furthermore, using a Continuously Variable Transmission CVT or Fixed-ratio Gear Transmission FGT was the most common.

4.3 Phasor diagram

The benchmark motor has the permanent-magnet glued on the rotor surface i.e. non-salient pole machine. The design of such a machine is quite well-known in that its synchronous reactance at d-axis and q-axis are equal $X_d = X_q$ and the machine total reactance is represented by the synchronous reactance X_s. In the steady state with balanced sinusoidal phase currents, the operation is characterised by the phasor diagram shown in Figure 4.8.

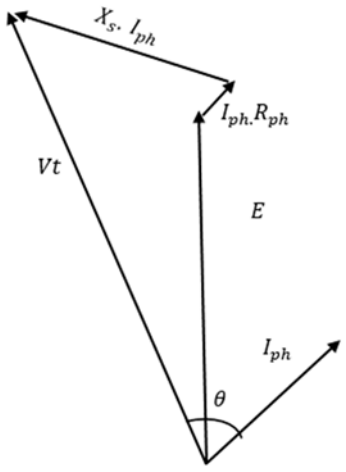

Figure 4.8 Phasor Diagram of the SMPM machine at the rated operation condition

The sum of the back-EMF and voltage-drop across the winding resistance and synchronous reactance must be equal to the applied terminals voltage V_t as given in Equation (4.2).

$$\overline{Vt} = \bar{E} + \left(R_{ph} + jX_s\right).\overline{I_{ph}} \tag{4.2}$$

However, since $X_d = X_q$ there is no permeance difference between d and q axes, hence, there is no reluctance torque. Therefore, the total generated torque is purely electromagnetic as can be found from the torque expression in (4.3).

$$T = 3\,p\,\psi_f\,I_{ph}\cos(\theta) \tag{4.3}$$

Where p is the number of pole-pair, ψ_f is the flux linkage, θ is the angle applied between the phasor voltage Vt and the phase current I_{ph}.

The terminal voltage of the benchmark motor has been supplied from mains power using a voltage booster. The line-line voltage V_{LL} was 218, which is obtained from DC supply voltage bus of 380 V_{DC} using inverter. However, at maximum operating temperature, the phase resistance R_{ph} was 3.94Ω. Therefore, to avoid the increase in the current density J and copper loss that can quickly overheat the winding, the supply current was limited to 5A (7A peak phase current). Thus, with wire diameter of 0.9mm, the current density was read off as 7.86 A/mm2.

4.4 FEA analysis of benchmark motor

The dimension of the benchmark design as given in Table 4.1 and Figure 4.3 along with the subsequent parameters of the design were replicated into “MotorSolve” and

"MagNet" software provided by Infolytica to perform FEA analysis of the machine performance. Figure 4.9 shows an axisymmetric model of the final benchmark motor.

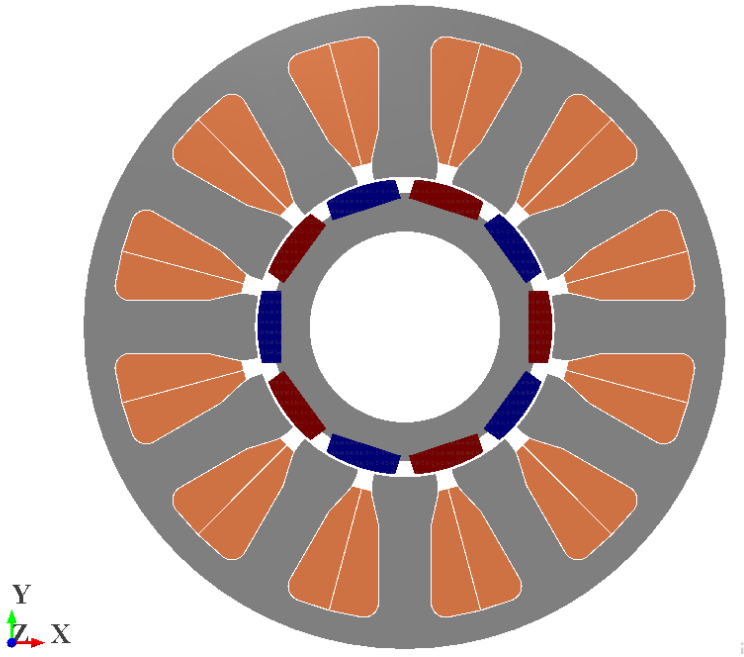

Figure 4.9 Layout of benchmark motor design in "MotorSolve" FEA program

The corresponding FEA analysis in Figure 4.10 shows the flux density distribution at load condition. The analysis shows that the maximum flux density value was 1.6T in the stator teeth. However, at no-load condition, the magnitude of the average flux density was 1.45T, which is equal to the knee point for this core material M330-35A.

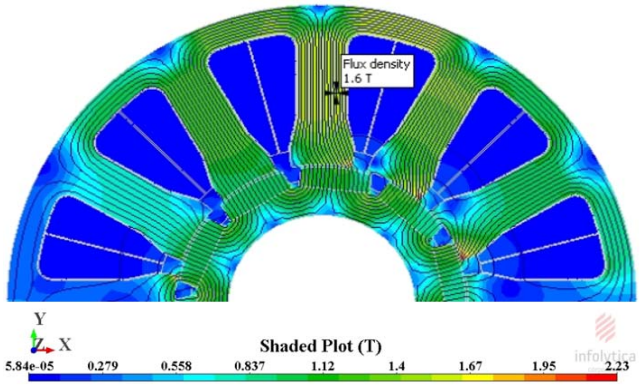

Figure 4.10 Flux densities in stator and rotor laminations calculated by FEA

The peak operating profile in Figure 4.7 showed the torque and speed that the motor is required to develop at the 380Vdc supply voltage and RMS phase current of 5A. Allowing for a 10V voltage drop in the inverter, the RMS terminal voltage V_t, which corresponds to 380Vdc supply, is 118V. Calculation of motor performance via the phasor diagram of the previous section requires values for flux linkage ψ_m and synchronous reactance X_s, all of which can be determined using FEA analysis. However, the fundamental open-circuit flux linkage due to the permanent magnet ψ_m only, without the excitation current, was calculated from FEA solution as shown in Figure 4.11. In this case, the peak flux linkage was read off as 0.511 Wb.turn which corresponds to RMS fundamental open-circuit flux linkage per-pole of ψ_m= 0.361 Wb.turn.

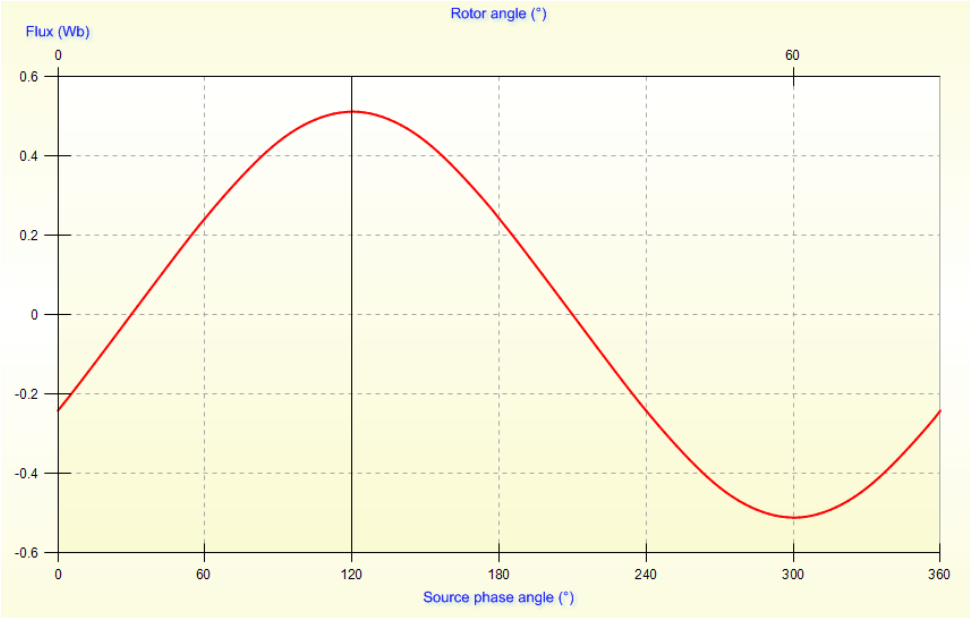

Figure 4.11 Waveform of the fundamental flux linkage of the benchmark motor

Figure 4.12 shows the total inductance L_s of the benchmark motor. The waveform shows that inductance is almost constant over different ranges of current. In this case it was L_s = 47.8 mH.

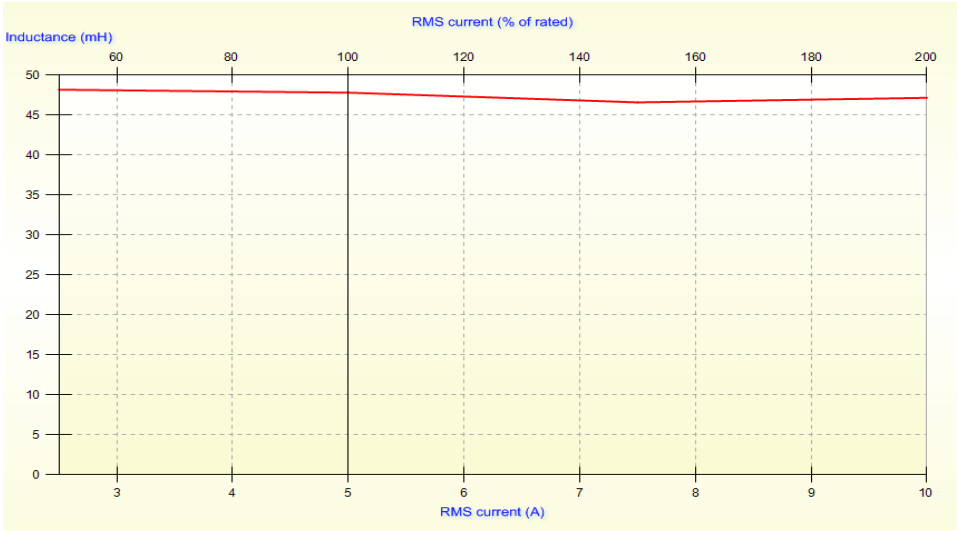

Figure 4.12 Average inductance current in benchmark motor design at different gear levels

The phasor quantities have been determined for the benchmark motor and can be applied in the Equations (4.2) and (4.3). Therefore, with a frequency of 53.3Hz at base-speed, the back-EMF was calculated as 119Vrms, which agrees with the value simulated from FEA analysis, as shown in Figure 4.13.

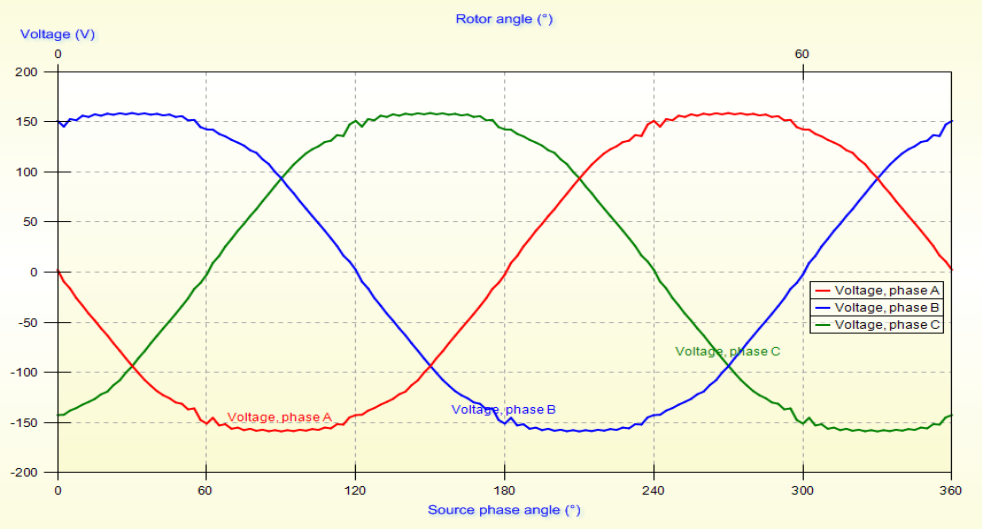

Figure 4.13 Waveform of peak phase voltage generated from FEA analysis at no-load for the benchmark motor

With the value of flux linkage, the torque profile over the full range of speed can also be calculated from Equation 4.3

$$T = 3 \times 5 \times 0.361 \times 5 \times \cos(0) = 27.07\ N.m$$

The generated electromagnetic torque that computed on FEA analysis almost agrees with the analytical calculated results 26.3Nm, as shown in Figure 4.14.

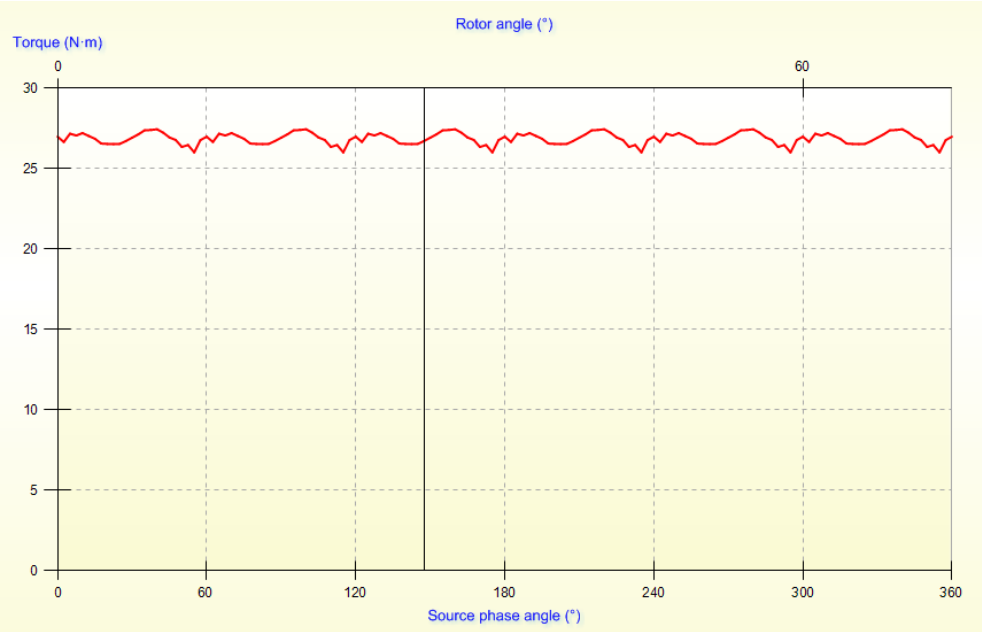

Figure 4.14 FEA analysis of Electromagnetic generated torque of the benchmark design

As mentioned earlier, in addition to the high efficiency and high overload capability, electric motors designed for traction applications are required to have a constant torque at low speed to meet the demand power needed to start a vehicle or to climb up a hill. It is also required to have a wide constant power region CPR to determine the maximum speed of the vehicle in flat run through cruising operation. Through both constant torque and power regions, overload torque and power are welcome for quick acceleration at any speed, as long as the motor is thermally safe while the inverter and battery are at their maximum rating limits.

Comparing the achieved torque/speed profile of the benchmark machine, as appeared in Figure 4.15, with the ideal characteristics, it can be said that benchmark design has developed all the required torque in the constant torque region up to the base-speed of 640rpm.

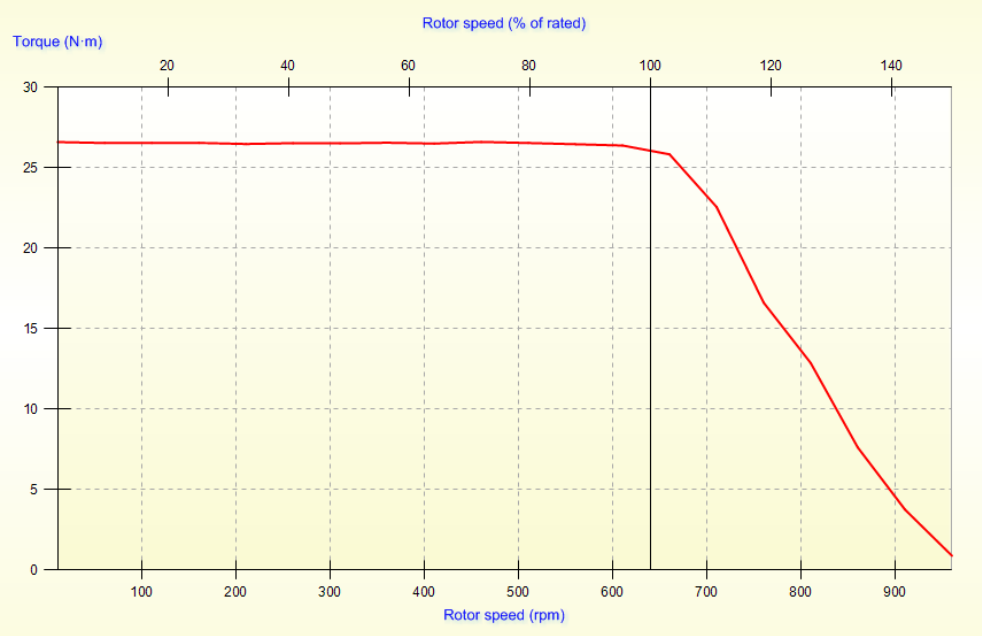

Figure 4.15 Torque profile at 380Vdc for the benchmark motor design

However, after base-speed, the PWM duty-cycle reaches its maximum and the motor terminal voltage is equal to the maximum voltage available from the converter. Consequently, an advance angle needs to be applied in the field weakening region to match the required power. The required torque is achieved by advancing the phase angle from an initial 10° towards 75° at 2400rpm. Finally, the torque/speed characteristic has been constructed as shown in Figure 4.16. It is shown that the motor has the capability of developing the required torque over the full range of speed (640-2400) rpm.

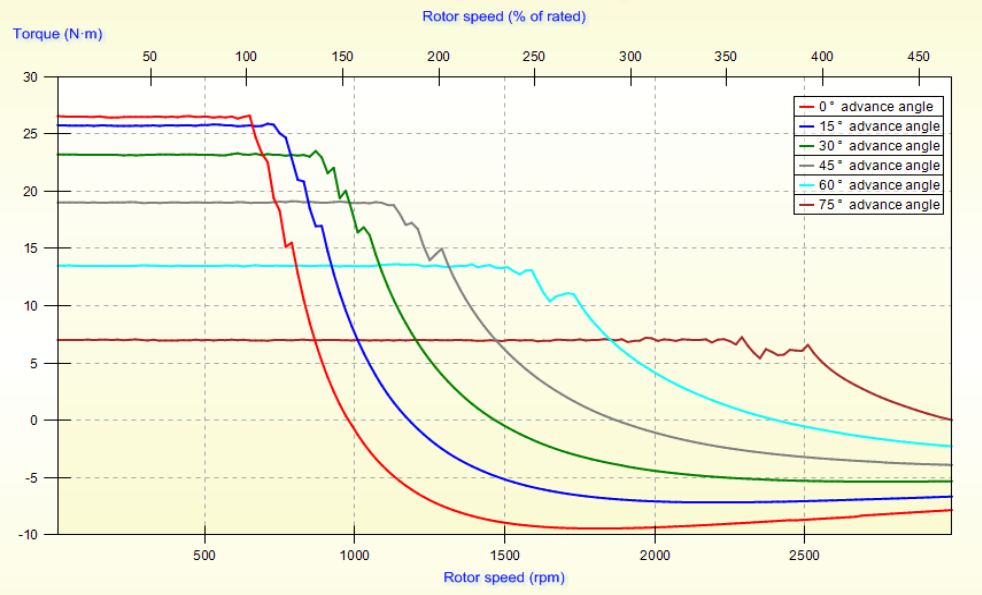

Figure 4.16 Torque/speed profile at 380Vdc for the benchmark motor design at different advance angles

According to the design specification, the motor should develop 1.75 kW through the constant power region at and after 640 rpm until 2400 rpm. Figure 4.17 shows the power-speed characteristics of the benchmark motor. The graph shows that benchmark design has delivered the required power over the entire range of speed through the CPR.

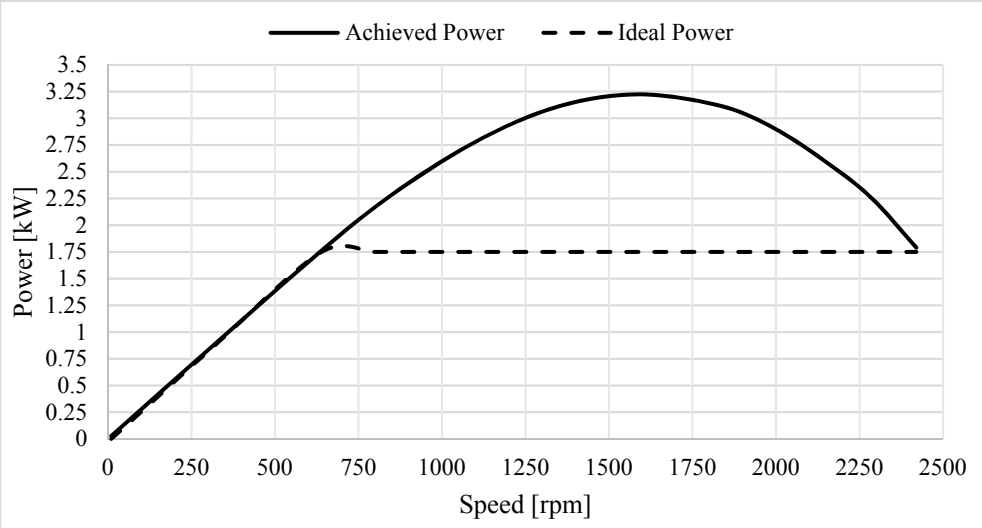

Figure 4.17 Power-speed characteristics of benchmark motor and ideal power with required power at full speed range

Generally, electric machines for traction application are designed with consideration of cogging torque. For the benchmark design, the cogging torque was 0.5Nm as shown in Figure 4.18. This value is considered reasonable for small electric machines.

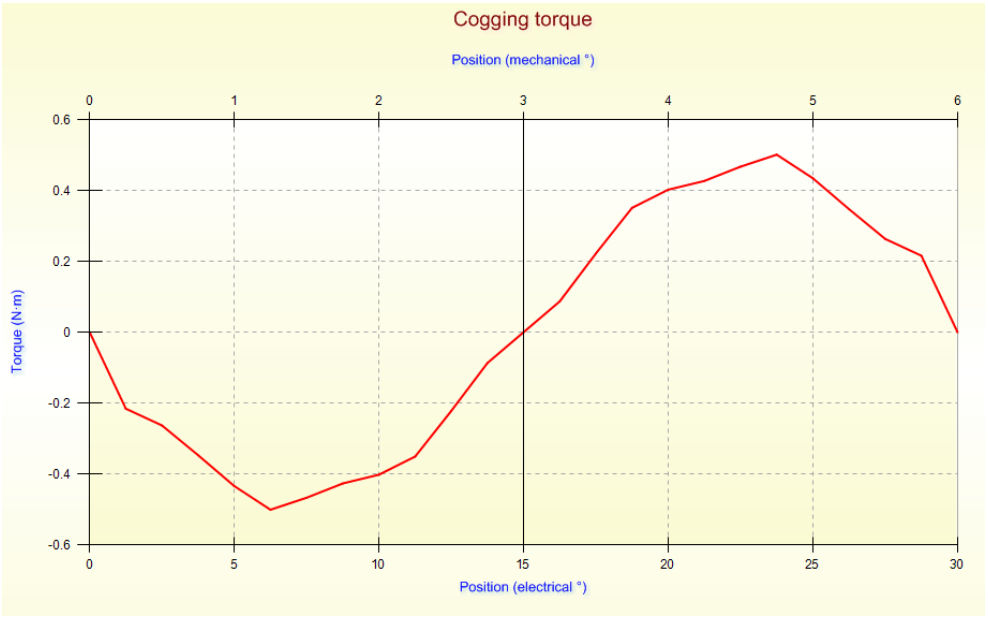

Figure 4.18 Cogging torque of the benchmark design

4.5 Losses and efficiency

The total losses have been evaluated and the motor efficiencies over the full range of speed have been plotted as shown in Table 4.5 and Figure 4.19 respectively. As expected, the copper loss formed the highest portion of total losses, although the core losses in the magnetic circuit will vary because they are a function of both the peak field distribution (B) and the speed. Figure 4.19 shows a lowest efficiency of >90% was achieved through the constant power region, falling to 80% over the constant torque region.

Table 4.5 Losses of the benchmark motor

	BenckMark
Loss - Total (kW)	0.218
Loss - Winding (kW)	0.202
Loss - Iron (kW)	0.0143
Loss - Stator back iron (kW)	0.00436
Loss - Stator teeth (kW)	0.00988
Loss - Rotor back iron (kW)	8.2E-05
Loss - Magnet 1 (kW)	0.00139

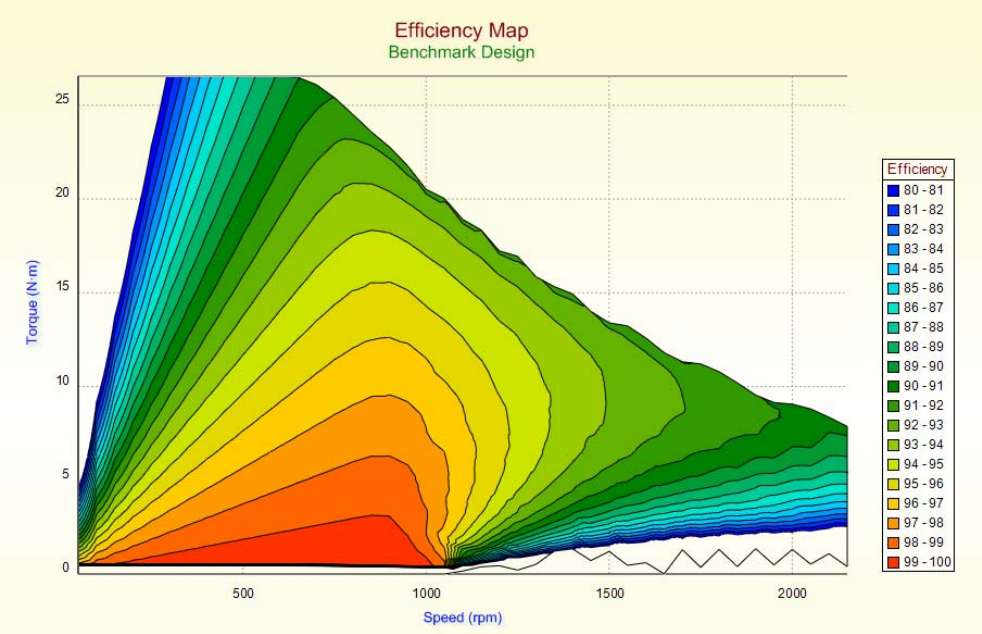

Figure 4.19 Efficiency of the benchmark motor over full range of speed

4.6 Chapter summary

In this chapter, a full description of dimensions and material properties of the benchmark motor has been given and illustrated. The torque, power and speed characteristics of the benchmark motor have been analysed by FEA and compared with the ideal specification of the motor. From the foregoing analysis, it was found that the benchmark motor can provide the required torque over constant torque region and enough power over the constant power region with high efficiency.

5 Chapter 5: Analytical design model of BLPMDC motor

5.1 Introduction

Analytical models are often used in the first step of an electric machine design process. They are usually associated with an optimisation method to find a solution that fulfils particular design specifications. Therefore, the aim of this chapter is to build an analytical model "optimisation problem" of BLPMSM motor and integrate it with Bees Algorithm to search for an optimal design solution. The design specifications are similar to the benchmark design as described in the previous chapter. The main objectives for the optimisation are to search for an alternative design with higher power density, improved efficiency and lower cost.

5.2 Analytical design methodology

An analytical model is based on numerous equations used to evaluate the dimensions and electromagnetic parameters of an electric machine. Each equation in the model describes a physical phenomenon or hypothesis associated with an electric machine. The equations of an analytical model contain hundreds of variables that describe particular magnetic, electrical or thermal parameters. Depending on the optimisation

problem and objective function, the value of these variables can be kept constant or vary through the optimisation search.

The procedure to accomplish the analytical design of an electric machine is described in a flow chart as shown in Figure 5.1. At the beginning of each iteration, the Bees Algorithm initialises random values for the design prime-variables $D, L,\ h_m\ and\ J$. The quantity of initialised prime variables depends on the set of parameters in the algorithm, as will be explained later. Hence, in each iteration, the optimisation algorithm evaluates a different combination of prime variables. According to each combination of prime variables, the corresponding variable machine dimensions are determined and the electromagnetic and thermal parameters in the optimisation problem are identified. Subsequently, the output of the multi-objective function is calculated and the fitness of prime variables combination is assigned at the end of each iteration.

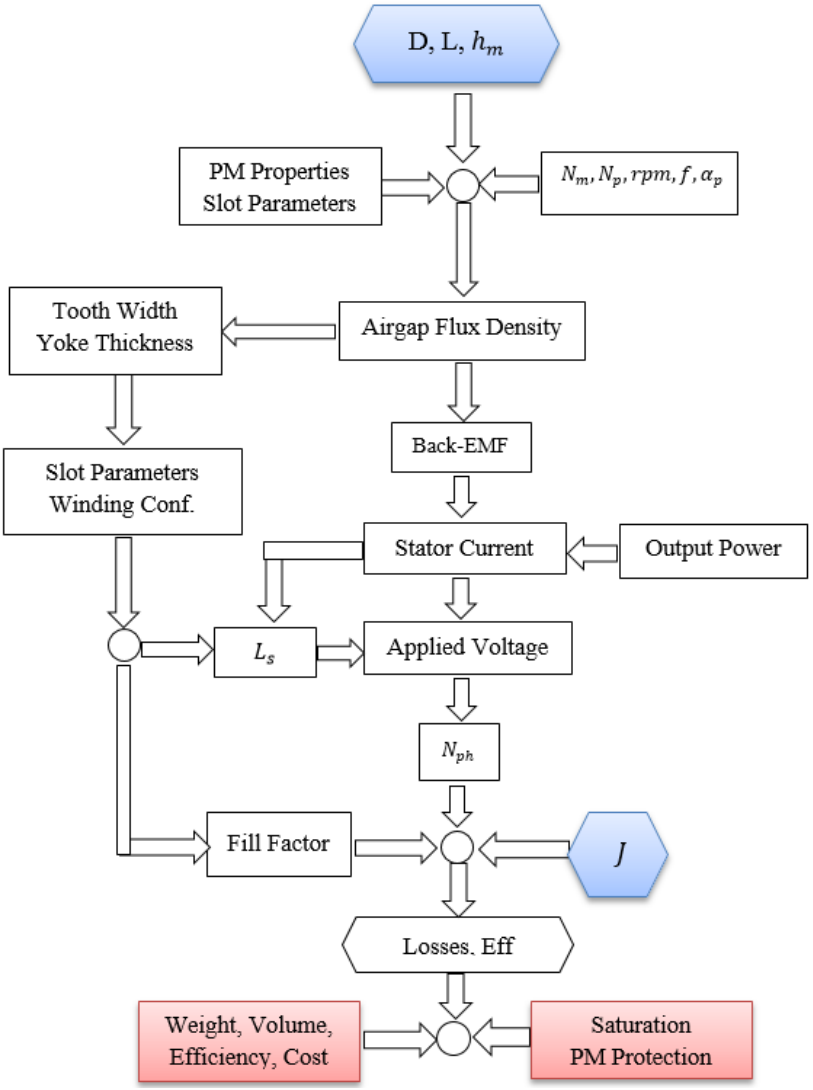

Figure 5.1 Flow chart of the optimisation analytical design

While the values of the prime variables continuously keep changing throughout the optimisation search, the optimisation problem also contains parameters with predetermined values that never change during optimisation progress. The values corresponding to these parameters are determined prior to the optimisation search, based on specific material properties, general typical values or previous results obtained from FEA analysis. The main aims of keeping these parameters at constant

values is to enhance smooth output torque of the machine, increase the efficiency and also reduce the computation time for the optimisation process.

However, to ensure the optimisation search delivers only a feasible design, the values of some parameters are constrained to a certain maximum or minimum range. During the optimisation search, if the limits of these constraints are violated, a penalty will be added to the objective function. Hence, the output value of the objective function will increase and its fitness be significantly reduced, which indicates that the initialised prime variables at this particular iteration have led to a prototype with shortcomings and the implementation of this design is infeasible.

5.3 Parameter selection

In this section, the processes of selecting values for predetermined parameters will be performed. The criteria for selecting these values are to choose the most promising values that can increase the machine's performance. The performance analysis of the selected parameters will be approved by carrying out an analytical or FEA test. However, in some cases an empirical result from previous work can be involved. The parameters that will be selected in this part are the number of slots, number of poles and magnet shape.

5.3.1 Selection number of pole-per-slot pole/slot

In the design of an electric machine, the selection for number of slot-per-poles is crucial. The combination choice depends upon many factors, such as winding configuration, grade of magnet material and rotational speed. However, for three-

phase machines, there are many slot/pole combinations that vary for different applications and design objectives.

To find an optimal ratio for the number of slots per pole, an easy method can be used by including this parameter with the optimisation prime variables. However, this approach will increase the number of optimisation variables and significantly complicate the optimisation problem. Hence, the computation time consumed by optimisation to search optimal parameters will increase significantly.

A simple basic rule can be used to estimate the number of poles i.e. the number of poles is inversely proportional to the maximum speed of rotation. The reason for that is to limit the frequency and consequently reduce the iron losses. Therefore, it is convenient that electric machines with high rotational speed are designed with a small number of poles. On the other hand, every time the number of poles is doubled, the thickness of stator back-irons is reduced by one half. Hence, for the same stator outer diameter, this will lead to an increase in the slot space for winding coils and therefore reduce copper loss.

PMSM machines are reported to have relatively high torque distortion, which is mainly composed of cogging torque and torque ripple that result from an inappropriate selection of both the number of slot-per-pole and magnet pole coverage ratio α_p. In general, torque distortion is not desirable as it degrades the overall performance of the machine. Therefore, to seek a general solution in this work, an analytical study was performed to evaluate the cogging torque components for various combinations of slot-per-pole.

Cogging torque is defined as the oscillatory torque caused by the tendency of the rotor to line up with the stator in a particular direction, where the permeance of the magnetic circuit seen by the magnet is maximised [62]. Although numerous methods have been proposed recently for the calculation, analysis and reduction of cogging torque as illustrated in the literature [63, 59, 64, 65], using fractional slot/pole ratio with a concentrated stator winding is generally the first and easiest solution to achieve a low cogging torque.

In the benchmark machine, the number of slot-per-pole was $N_{spp} = 1.2$, with double-layered concentrated non-overlapping winding resulting in a high winding factor of 0.933 and short end-winding. These factors improved the machine output performance and efficiency. It is expected that a lower value of N_{spp} will lead to lower cogging torque and higher winding factor. Therefore, the number of slot-per-pole used in the benchmark design has been compared in FEA analysis with a new combination i.e. 9/8 to evaluate cogging torque as shown in Figure 5.2. The results show that cogging torque was minimised when the number of poles and slots were set to eight and nine respectively.

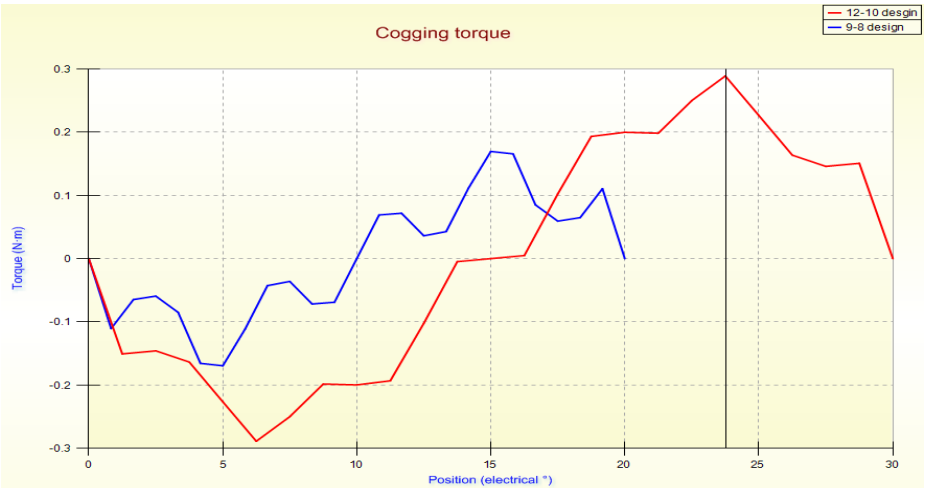

Figure 5.2 Cogging torque simulation result for different slot/pole combinations

However, it has been stated that, for a given stator inner diameter, the power density of the motor can be increased by using more poles [66]. This is due to the reduction in the stator yoke thickness, which results in a reduction of the stator outer diameter. On the other hand, according to Equation (5.1), the electromagnetic power increases as the number of poles decreases. Therefore, reducing the number of poles must be accompanied with optimum stator inner diameter to compensate proportionally for the reduction in power density.

$$P_{elm} = 0.5\pi^2 k_w D_{in}^2 L\, f B_m J/p \tag{5.1}$$

Furthermore, the use of eight poles will reduce the frequency and proportionally decrease the core loss. Finally, compared with the benchmark design, the new combination of number of slot-per-pole 9/8 will slightly increase the winding factor to 0.945. Therefore, with eight poles the machine is expected to generate a higher electromagnetic power and lower core loss.

5.3.2 Selection of magnet pole

With regard to the second cause of torque distortion i.e. the torque ripple, also called torque pulsation, assuming ideal driving current, it refers to the additional oscillatory torque component that results from the interaction between the magnetomotive force MMF produced by the permanent magnet and the space-harmonic in the winding layout. Therefore, reducing the amplitude of the MMF produced by the permanent magnet will definitely reduce the torque ripple.

According to [67] the amplitudes of the MMF fundamental, 3rd, 5th, 7th … harmonics can be calculated for sinusoidal waveform distribution as in (5.2)

$$MMF_{PM}(\theta_r, t) = \sum_{n=1,3,5,..} n\frac{\alpha_p \,.\, mmf_{(PM)}}{\pi}\,(nA_1 + nA_2)\,.\cos(p\theta_s - \,\omega t) \qquad (5.2)$$

Where

$$nA_1 = \frac{\sin\left((n+1)\frac{\alpha_p}{2}\right)}{\left((n+1)\frac{\alpha_p}{2}\right)}$$

$$nA_2 = 1 \qquad for\ n = 1$$

$$nA_2 = \frac{\sin\left((n-1)\frac{\alpha_p}{2}\right)}{\left((n-1)\frac{\alpha_p}{2}\right)} \qquad for\ n \neq 1$$

Where, n is the space harmonic corresponding to amplitude for the rotor MMF and $mmf_{(PM)}$ is the magnetomotive force produced by the permanent magnet. For the surface-mounted rotor, topology can be calculated as $mmf_{(PM)} = H_c.hm$, where H_c is the coercive field intensity of the permanent magnet material and hm is the thickness of the permanent magnet in the direction of magnetisation.

From Equation (5.1) it appears that the amplitude of the MMF harmonic is not related to the rotor diameter or the axial length of the machine; instead, it is a function of magnet pole coverage coefficient α_p. Therefore, an appropriate selection of α_p that has least total harmonics can significantly reduce the torque ripple and provide smoother transition of the torque.

Figure 5.3 shows the amplitude of the fundamental, 3rd, 5th, 7th and 9th harmonics produced from the permanent magnet for different magnet pole coverage ratios (α_p between (0.5-1). As shown in the figure, the fundamental harmonic has increased proportionally with the increase of α_p. Also, the total MMF harmonics have a lower value when α_p is equal to 0.83. Therefore, this value for α_p is considered as the optimal point that generates lower MMF harmonics.

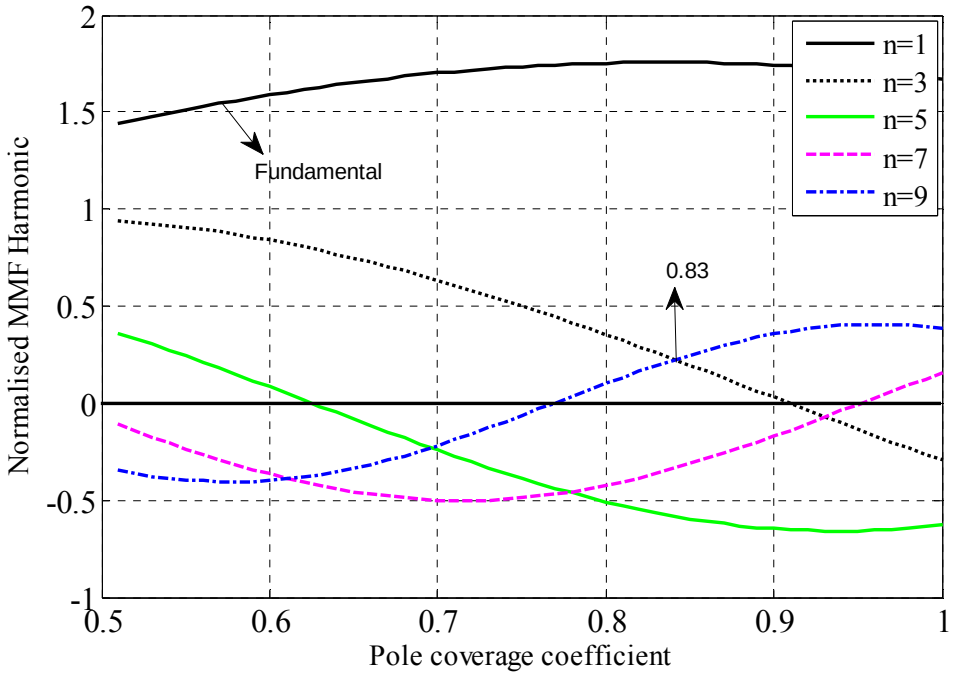

Figure 5.3 Normalised harmonics for range of pole coverage coefficients

Furthermore, using this ratio for magnet pole coverage, the flux leakage between the magnets is expected to be reasonable. Therefore, a value of $\alpha_p = 0.83$ would be appropriate to minimise the torque ripples and also reserve the flux for energy conversion.

5.3.3 Selection of magnet shape and magnetisation direction

The operation of BLPMSM motors can be classified according to their excitation into two main categories: (BLPMDC), which has trapezoidal back-EMF; and sinusoidal (BLPMAC), which has sinusoidal back-EMF. Although both types of machines have similar physical construction, the difference between the two types refers to the controller and the inverters used to drive the machine. However, in order to maximise the torque density and minimise torque pulsations, it is desirable to operate a machine that has a trapezoidal back-EMF waveform in BLPMDC mode, and a machine that has a sinusoidal back-EMF waveform in BLPMAC mode [5].

An ideal sinewave motor is distinct in three aspects: sinusoidal distribution of magnet flux in the airgap; sinusoidal current waveform; and sinusoidal distribution of stator conductors. Thus, the purity of the sinewave depends partially on the magnet flux-distribution and partially on the winding distribution, which should be formed as near as possible to the sinewave [53]. However, if both magnet flux and winding were perfectly sine-distributed, there would be no flux–linkage. Fortunately, practical windings are not perfectly sine-distributed. Therefore, in order to operate a machine which has a sinusoidal back-EMF at maximum torque density and minimum torque pulsation, it is necessary to make the magnet flux distribution as nearly sinusoidal as possible.

To achieve sinusoidal flux distribution in the airgap, a study was performed to identify the most suitable shape of magnet and magnetisation direction that can generate back-EMF closest to the ideal sinusoidal waveform. In the study, three different shapes of magnet with different magnetisation directions, which are commonly used to generate

sinusoidal flux, have been tested by FEA to determine the shape and characteristics of back-EMF waveform. The three magnet shapes, as shown in Figure 5.4, are: a) the magnets are parallel-magnetised; b) the bread-loaf magnets naturally profile the flux distribution to achieve proper sinewave; c) the magnets are radially-magnetised. However, the stator and rotor outer diameter, machine length, winding configuration, magnet material and thickness were kept unchanged at each test.

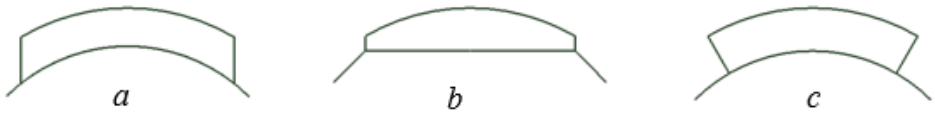

Figure 5.4 PM rotors commonly used in sinewave motors.

Figure 5.5 shows the back-EMF waveform generated from the three different magnet shapes. The waveform for the parallel magnet (green) is hidden behind the blue waveform. Although the three designs have generated almost the same amplitudes, the waveforms resulting from the parallel and bread-loaf magnet shapes were more sinusoidal than the radial magnet and also have less ripple. However, considering the costs, the bread-loaf magnet shape has less manufacturing cost than the parallel shape. Hence, bread-loaf magnet shape was chosen for the design.

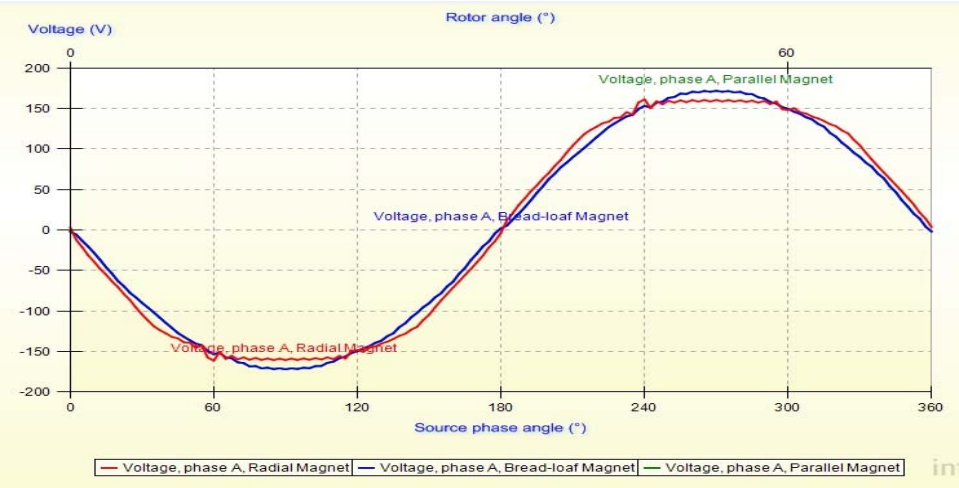

Figure 5.5 Generated back-EMF for different magnet shape

5.3.4 Design material selection

Generally speaking, the primary determinants of material selection are the cost, torque per unit volume, range of operating temperature, and the severity of operational duty [68]. Therefore, it is important to select appropriate grades of permanent magnet, silicon steel and insulation materials that are compatible together to produce maximum power density and smooth energy transition within the operating temperature and at reasonable cost.

The selection of permanent magnet material is limited not only by the magnetic loading; it is also determined by the demagnetisation effect of the magnet at the operating temperature. As the motor is designed to operate with Totally Enclosed Non-Ventilated (TENV) cooling, it is important to select a grade of permanent magnet that has the ability to withstand demagnetisation due to temperature variation and armature reaction.

The selection of electrical steel lamination is limited by the core loss and saturation level of the stator teeth. Excessive saturation of stator laminations requires extra excitation MMF from the permanent magnet and causes extra heating due to core losses. Therefore, selection of the electric steel should consider the ability to accommodate the generated magnetic flux from the permanent magnet.

The motor design will be compared with the benchmark motor in terms of weight, volume, efficiency and cost at the same cooling conditions. However, as the cost of this material has not been specified in the benchmark design, instead of including the "cost" in the optimisation objective function, the same material as the benchmark design will be utilised in the new design. This includes the permanent magnet material,

silicon steel and insulation material. Subsequently, the comparison point "cost" will not be included in the objective function; instead, the maximum weight of the permanent magnet will be limited so that it should not exceed the original weight in the benchmark design.

5.4 Analytical model based on prime variables

In this section, an analytical design method for BLPMSM is outlined. The values for the predetermined parameters *Np, Nm*, α_p and machine output specifications, as shown in Table 5.1, will be kept unchanged during the optimisation search. The properties of the machine active materials, permanent magnet and steel will also be included in the optimisation programme to evaluate the machine efficiency and performance.

Table 5.1 Specifications of the new design traction motor

Parameters	**value**
Output power [W]	1750
Speed [rpm]	640
Battery operating voltage (V-dc)	380
Number of slots	9
Number of poles	8
Magnet coverage coefficient	0.83

The optimisation objective function attempts to minimise the machine weight, volume, cost and to maximise efficiency. At rated power and speed, the main parameters directly related to the objective function are stator inner diameter D, machine stack length L , thickness of permanent magnet h_m and current density J. These parameters

are called the prime variables and the main task for optimisation is to search for optimal values for these prime variables. Therefore, in the following calculations the values of these variables are assumed to be known.

5.4.1 Airgap flux density

The amplitude of fundamental airgap flux density can be calculated based on the analytical Equations (3.34) and (3.36) provided in Chapter 3 for surface mounted permanent magnet topology.

As the machine is relatively small, the leakage coefficient f_{LKG} and the reluctance factor k_r have typical values of 0.95 and 1.0 respectively. The length of the airgap for a small electric machine with value of 0.5mm and the slot opening of 2.0mm are also considered reasonable. With these given values, the Carter's coefficient k_c and the amplitude of the fundamental airgap flux density $B_{g(1)}$ can be calculated based on the analytical Equation (3.36) in Chapter 3.

From the determined amplitude of flux density in the airgap, the electrical parameters in the phasor diagram and the geometries corresponding to the rotor and stator can be calculated. The airgap flux density is coordinated along a pole to obtain the flux per pole $\Phi_{(1)}$. Therefore, the amplitude of the fundamental flux $\Phi_{(1)}$ is

$$\Phi_{(1)} = B_{g(1)} \cdot A_g \tag{5.3}$$

Where A_g is the airgap area under one pole.

The thickness of the stator back-iron S_{ebi} and rotor back-iron R_{ebi} can be directly calculated based on the magnetic properties of the steel lamination and the amplitude of the fundamental flux. Before considering the field from armature reaction, the flux

density at the knee point B_{knee}, as shown in Figure 5.6, is considered as the maximum flux allowed in the steel. For most of the non-oriented silicon steel, typical value of B_{knee} ranges between (1.3T-1.45T). Accordingly, S_{ebi} and R_{ebi} can computed as

$$S_{ebi} = \frac{\Phi_{(1)}}{2\, B_{knee}\ \mathrm{L}\, k_s} \tag{5.4}$$

$$R_{ebi} = \frac{\Phi_{(1)}}{2 B_{knee}\ \mathrm{L}\, k_s} \tag{5.5}$$

Where k_s is the lamination stacking factor with a typical value between (0.95-1).

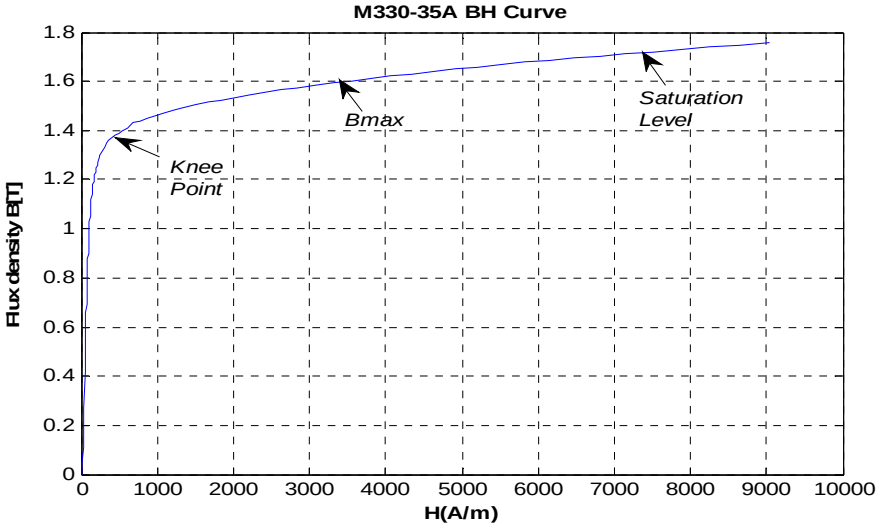

Figure 5.6 Magnetisation characteristics of M330-35A

The maximum flux density in the stator teeth Φ_{Tw} is slightly different. A tooth concentration factor k_{ds} between the tooth and airgap should be calculated and considered correctly [69]. It is calculated as the width ratio of one slot pitch τ_s over one tooth pitch τ_{Tw} over. For the magnetic flux density in the stator teeth Φ_{Tw} ,

$$T_w = \frac{\Phi_{(1)} \times k_{ds}}{B_{knee}\ \mathrm{L}\, k_s} \tag{5.6}$$

$$k_{ds} = \frac{\pi . \frac{D}{Nm}}{\pi . \frac{D}{Nm} - Bs0} \tag{5.7}$$

5.4.2 Phasor diagram

The phasor diagrams for synchronous machines are constructed as shown in Figure 5.7. When the machine rated voltage V_t is given, other electrical parameters EMF, phase resistant R_{ph}, synchronous inductance L_s and phase current I_{ph} can be approximated at rated operating condition using the relation between parameters as expressed in Equation (5.8)

$$\overline{V_t} = \overline{EMF} + \left(R_{ph} + jX_s\right).\overline{I_{ph}} \tag{5.8}$$

Where V_t is the terminal voltage, jX_s is the synchronous reactance.

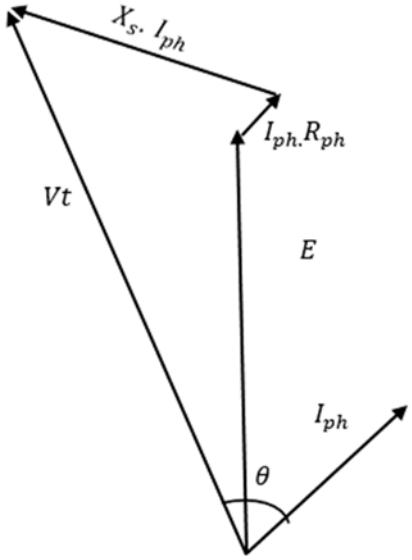

Figure 5.7 Phasor diagram at rated operation condition

When the flux is generated from the permanent magnet and linked with the stator winding, the induced back-EMF is proportional to the rotational speed of the rotor. The flux in the airgap is assumed to have a sinusoidal waveform with peak amplitude value i.e. fundamental airgap flux $\Phi_{(1)}$. Assuming all the flux produced from the permanent magnet is linked with the stator winding, the RMS value of the fundamental generated $EMF_{(1)}$ is obtained by (5.9)

$$EMF_{(1)} = \frac{2\pi f}{\sqrt{2}} \left(k_w . N_{ph}\right) \mathrm{B}_{g(1)} \frac{2\pi DL}{p} \tag{5.9}$$

k_w is the winding factor and N_{ph} is the number of turns in series per phase. How to determine the number of turns will be explained later.

As the rated output power of the machine is given, assuming the machine is designed to be inverter-driven with field oriented control applied, the RMS value of the phase current I_{ph} under rated operating condition can be estimated as:

$$I_{ph} = \frac{P_{out}}{3. EMF_{(1)}} \tag{5.10}$$

The total inductance L_s in the synchronous machine is a linear sum of three main inductances: the airgap inductance L_{sg}, slot leakage inductance L_{sl} and the end-winding inductance L_{ew} as given in (5.11)

$$L_s = L_{sg} + L_{sl} + L_{ew} \tag{5.11}$$

The airgap inductance L_{sg} contributes to the major value of the total actual inductance. It is produced from the armature reaction inductance and is calculated as (5.12)

$$L_{sg} = \frac{3}{\pi}\left(\frac{k_w N_{ph}}{p/2}\right)^2 \frac{\mu_0}{g_{eq}} DL \tag{5.12}$$

The slot-leakage inductance L_{sl} mainly depends on the shape of the slot. Although, at this stage of calculation, the exact dimensions for the stator slot are unknown, typical values of the mean width of the slot B_{s1}, B_{s2} and the height of the slot H_{s0}, H_{s1} H_{s2} can be estimated. Later, when the exact slot dimension is determined, L_{sl} can be re-calculated accurately. However, depending on the slot shape, there are many equations to determine L_{sl} ; classical analytical expression can be used as in (5.13)

$$L_{sl} = \frac{2\,\mu_0\,L\,(N_{ph})^2}{p.q}\,\lambda_{sl} \tag{5.13}$$

Where q is the number of slots per pole per phase and λ_{sl} is the coefficients of leakage permeance of the slot [62]

$$\lambda_{sl} = \left(\frac{2}{3}.\frac{H_{s2}}{B_{s1}+B_{s2}} + \frac{2H_{s1}}{B_{s0}+B_{s1}} + \frac{H_{s0}}{B_{s0}}\right)\frac{1+3\beta}{4} \tag{5.14}$$

Where β is the ratio of slot pitch to pole pitch.

In Equation (5.14), the coefficient in the bracket is the effective depth/width ratio of the slot and is also known as slot permeance coefficient P_{slot} .

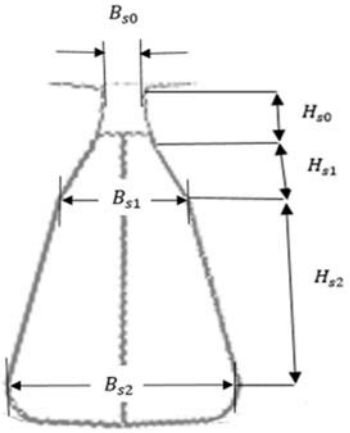

Figure 5.8 Slot design and geometries of the baseline motor

Due to the complex conformation of the end winding, it is difficult to calculate the end-winding inductance L_{ew} accurately. Its value is quite small and mainly depends on the number of layers and the length of the semi-circular arcs of the end winding i.e. winding pitch τ_c. A simple formula associated with double-layer to calculate L_{ew} can be obtained as in (5.15)

$$L_{ew} = \frac{\mu_0\,\tau_c\,N_{ph}^2}{16}\ln\left(\frac{\pi\ {\tau_c}^2}{4\ H_s B_{sm}}\right) \tag{5.15}$$

Where τ_c is the length of end winding pitch and B_{sm} is the mean width of the slot and calculated as $(\mathrm{Bs1} + \mathrm{Bs2})/2$. For a single layer, the coefficient "16" in (5.15) should be replaced by "8".

From the formulae for the phasor diagram components, it appears that the only missing value in all the equations is the equivalent number of turns in series per phase N_{ph} . As the value of the machine terminal voltage V_t is specified, the number of turns can be solved based on iteration for the Equations (5.9) to (5.15) using MatLab's internal function, such as (Fsolve or fzeros).

After solving electrical parameters in the phasor diagram and the number of turns per phase N_{ph}, the cross-section area of conductor A_{wire} can be calculated from the value of the current density J and phase current I_{ph}

$$A_{wire} = \frac{I_{ph}}{J} \tag{5.16}$$

Although the value of current density is initialised randomly by the optimisation, an accurate value can be adjusted from integration between the electromagnetic design model and thermal model of the machine.

The conductor diameter D_{wire} and total copper area of one slot A_{Cu} can be estimated from A_{wire} and the number of conductors per slot N_c, as follows:

$$D_w = \sqrt{\frac{4 \times A_{wire}}{\pi}} \tag{5.17}$$

$$A_{Cu} = A_{wire} \,.\, Nc = \frac{A_{wire} \,.\, N_{ph}}{q.p} \tag{5.18}$$

Values of the height of the stator tooth tip H_{s0} and the stator tooth wedge H_{s1}, as shown in Figure 5.8, can be estimated according to the manufacturing method. In small

electric machines, typical values of 1.5mm for the tooth tip and 2.5mm for the tooth wedge are reasonable. Assuming parallel tooth sides, the values of B_{s1} and B_{s2} can be determined as follows:

$$B_{s1} = \frac{\pi \left(D + 2\left(H_{s0} + H_{s1}\right)\right)}{N_m} - T_w \tag{5.19}$$

$$B_{s2} = \frac{\pi \left(D + 2 \times (H_{s0} + H_{s1} + H_{s2})\right)}{N_m} - T_w \tag{5.20}$$

The total slot area A_{slot} can be calculated upon slot-fill factor K_{fill} and copper area A_{cu} are known. For a single layer, a reasonable value of slot-fill factor K_{fill} is (0.65 – 0.7) and for a double layer (0.35-0.5) [67]. The slot area A_{slot} of trapezoidal shape is expressed as in (5.21)

$$A_{slot} = \frac{B_{s1} + B_{s2}}{2} H_{s2} \tag{5.21}$$

Again, internal "MatLab" function can be used to search optimal values for B_{s2} and H_{s2}.

5.5 Losses modelling and efficiency

During energy conversion in an electric machine, power losses occur that are dissipated in the machine components in the form of heat. The obtained power losses will be used as a heat source when performing the machine thermal analysis. Therefore, in order to design an efficient cooling system, it is important to accurately evaluate the power losses in the machine. Generally, there are two major parts of losses, electromagnetic losses and mechanical losses. Electromagnetic losses comprise copper losses P_{cu} and core losses P_{core} and in small electric machines they dominate

and contribute the major percentage of total power losses. Mechanical loss increases proportionally with speed and load, which contributes a small fraction of the total losses, and consists of bearing, frictional and windage losses.

5.5.1 Copper Losses

Copper loss P_{cu} is a resistive loss resulting from flowing current in the stator windings. The total for three-phase machine is given by (5.22)

$$P_{cu} = 3R_{ph}\left(I_{ph}\right)^2 \tag{5.22}$$

Where R_{ph} is the wire resistance in each armature phase and I_{ph} is the current flowing in each armature phase.

Typically, at low frequency such as 50-60 Hz, the phase wire resistance R_{ph} of a conductive wire length per phase l_{ph}, copper wire area of A_{wire} and electrical resistivity ρ_{cu} can be estimated as its dc resistance R_{dc} as given by 5.23

$$R_{ph} = R_{dc} = \rho_{cu}.\frac{l_{ph}}{A_{wire}} \tag{5.23}$$

At higher frequency the calculation of phase resistance should take into account the skin effect. However, the conductive wire length l_{turn} is the total of the length of one turn of the winding, including the end-winding part l_{end} as given by (5.24)

$$l_{turn} = 2(L + l_{end}) \tag{5.24}$$

The end connection depends on the coil pitch τ_p of the winding configuration. The average length of the end-winding for one turn is calculated as (5.25)

$$l_{end} = \frac{\pi(D + (H_{s0} + H_{s1} + H_{s2}))}{Nm} \tag{5.25}$$

Finally, the effective length of one phase winding is calculated as (5.26)

$$l_{w.ph} = 2\,N_{ph} * (L + l_{end}) \tag{5.26}$$

5.5.2 Core losses

Core loss is a function of the flux density in the core and frequency that is generated mainly in the stator back-iron and teeth. The total core loss is a sum of two major components, which are hysteresis loss P_{hys} and eddy current loss P_{edd}. The hysteresis component is associated with the changing magnitude and direction of the magnetisation of the magnet domains, while the eddy-current loss is generated by induced currents. Therefore, the iron core loss is calculated as a linear sum of P_{hys} and P_{edd}, as given by

$$P_{core} = (k_h\, f^{\propto} B_{max}^{\mathcal{B}} + k_e\,(f.B_{max})^2) \times Wt_{stator} \tag{5.27}$$

Where the first term of Equation (5.27) represents the hysteresis loss and the second term, the eddy current loss. B is the peak value of the flux density in the component core, k_h is hysteresis loss coefficient, k_e is eddy current loss coefficient, $\propto$ and $\mathcal{B}$ are constant material coefficients and Wt_{stator} is the weight of the stator

$$Wt_{stator} = Wt_{S_{ebi}} + Wt_{Tw} \tag{5.28}$$

Using thinner lamination can significantly reduce eddy current. However, the use of a thinner sheet can increase the industrial cost and it must be considered carefully. Also, total core loss is affected by manufacturing quality, such as the sharpness of cutting tools, and can be increased from its catalogue data by a factor called core loss augmentation coefficient with a typical value between (1.6-1.8) [62].

In addition to electromagnetic losses in the stator laminations, there are also electromagnetic losses in the rotor core and magnets that are produced due to the time harmonic in the armature reaction field. As this field rotates synchronously with the rotor, the core losses induced in the rotor core, which are laminated, is small at low and medium speed < 20000 rpm [70]. Also, due to the slotting effect, the airgap is relatively large and the effect of the armature reaction field is significantly reduced. Since the design of the machine is performed for the fundamental harmonic, it does not involve high speed or skin effects. The optimal design will not consider losses in the rotor back-iron or magnets. However, when the rotor core loss is more likely to occur, axial or circumferential segmentation for magnets and shorter pitch stator winding can be adopted [12]. Recently, numerous methods have been proposed for the analysis and reduction of eddy current losses in magnets at high and medium speed [70, 71, 72].

5.5.3 Mechanical losses

Friction loss P_{fric} is developed due to the contact between the bearing and the end-shafts. It can be approximated by the production of the friction torque and the orbital velocity of the bearing. Windage loss P_{wind} is the loss occurring due to friction between parts of the machine and the air inside the machine case.

Mechanical loss becomes a very important issue when the machine is running at high speed (20.000 – 200.000 rpm). For enforced ventilation, where gas fluid cooling is utilised, the flow type of the cooling fluid should be determined according to whether it is laminar, turbulent or a combination of both types and the windage loss should be calculated specifically in the main location around the rotor disc side where the

windage loss is most likely to occur [69]. In the case of our low speed motor, an estimation value of 1% of the output power P_{out} can be used to estimate the mechanical losses. Thus, the efficiency η of the machine can be given

$$\eta = \frac{P_{out}}{P_{out} + P_{cu} + P_{core} + P_{wind} + P_{fric}} \tag{5.29}$$

5.6 Thermal Analysis

While magnetic and electrical analytical models are designed to ensure the delivery of power and torque at a required speed with considerable efficiency, thermal analysis is of significant importance, as it interacts between these two models. The thermal model is designed to ensure the suitability of the machine design in terms of keeping the temperature of components within certain limits at rated operation conditions. The main purpose of this model is to protect the permanent magnet materials from being demagnetised and to protect winding insulation material from deteriorating. Therefore, the thermal model is of the utmost importance in validating the electric machine.

During the past decade, thermal analysis of electric machines has been undertaken by many authors [69, 73, 74, 75]. The techniques used to analyse electric machines can be classified into two categories, analytical lumped parameter model LPM approach and numerical analysis using finite element method FEM. While FEM is generic, shape independent and accurate, it requires high computational time to perform the thermal parameters. On the other hand, LPM analysis is not generic and requires some experimental data, such as heat flow and dissipation, that fit specific machines. However, the analytical design based on LPM has shown a good match with FEM

results and provides a fast calculation method with comparatively very low computational time; this is important when carrying out thermal analysis during optimisation search. Therefore, it is more ideal in the optimisation to use integrated LPM to determine the thermal parameters of electric machines.

An accurate thermal analysis based on LPM requires a high level of discretisation and exact approximation for the motor shapes and geometries. This includes all conduction and convection heat transfer diffusion of all the components inside the machine. Furthermore, to enhance the resolution of thermal models, the determination of thermal resistance should include the interface gaps and contact transition layers between these components. All of these parameters are critical in the thermal model and should be considered carefully in order to conduct an effective and accurate thermal analysis.

5.6.1 Conduction heat transfer

When considering conductive heat transfer between an electrical machine parts, one must bear in mind that heat conductivity can be in its most extreme either in the radial or axial and there is no heat transfer in the circumferential direction. This is very important when calculating the thermal resistance for adjacent components in the model network. The idea is that increasing the resolution of the network will not only give a more detailed description of the heat distribution in the motor, but ideally will also be able to more accurately model the different heat flow paths in the motor and associated resistances.

To show the heat transfer in an electric machine, a simulation of the heat transfer direction has been obtained from FEA for a one-pole section of stator lamination and

winding, as shown in Figures 5.9 and 5.10 respectively. In both figures, the heat transfer directions are represented by arrows.

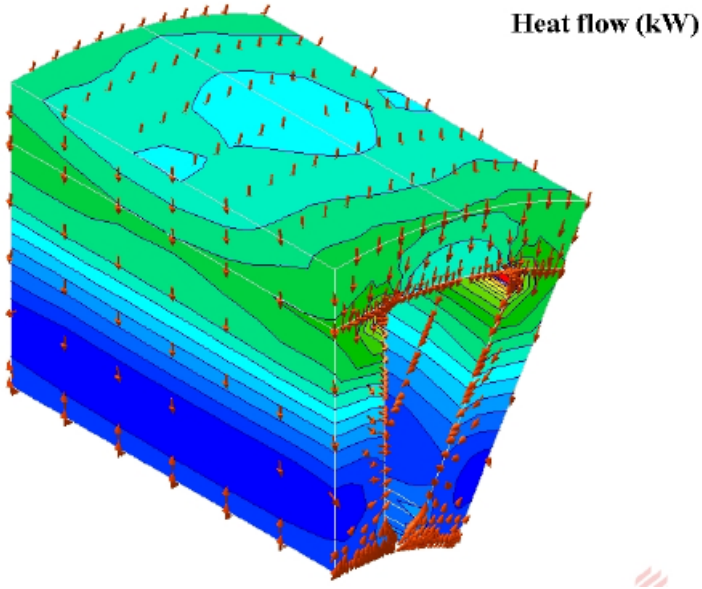

Figure 5.9 FEA simulation for heat transfer direction in one-pole section of benchmark stator back-iron and teeth

As shown in Figure 5.9, the effective heat conductivity in the radial direction of the stator lamination is very high compared with the corresponding axial directions. This is due to the presence of the dielectric coated layers between the lamination. The FEM simulation also shows that there is no heat transfer in the circumferential direction in the stator laminations. Therefore, the heat conductivity in the stator back-iron and teeth is mainly in the radial direction. Thus, thermal resistance in the axial and circumferential direction would be very low in the stator laminations.

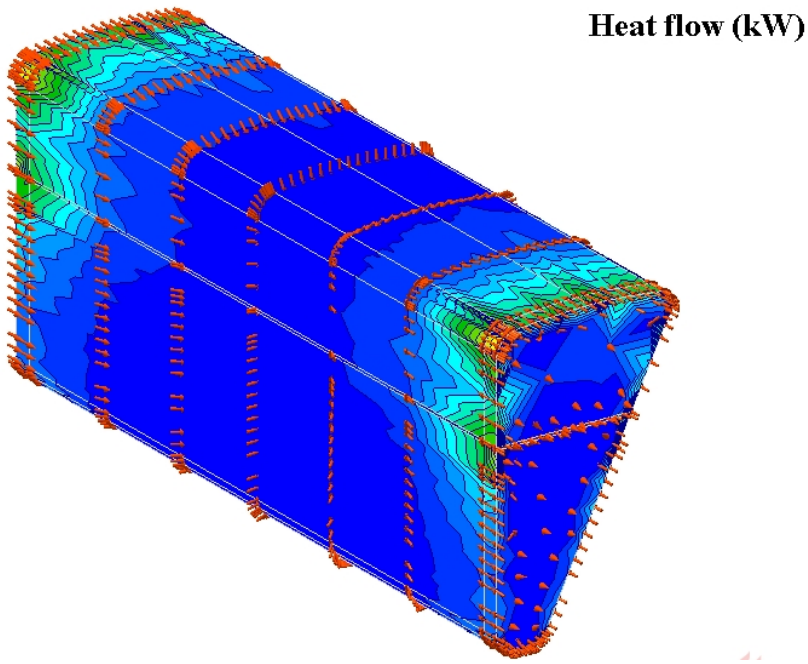

Figure 5.10 FEA simulation for heat transfer direction in one slot winding

Considering the heat transfer direction in the stator winding, as shown in Figure 5.10, the FEM simulation shows that the heat flow in an axial direction is dominant compared with the radial and circumferential directions. This is due to the presence and direction of the insulation layers around the winding. Therefore, heat transfer in the axial direction is the main flow path in the winding and the thermal resistance in this component should be determined at least in the axial direction. On the other hand, the direction of the heat flow in the end-winding is not axially distributed; instead, it flows over the entire surface of the winding. Thus, the end-winding passes through an uncertain amount of thermal resistance.

A proposed thermal model for electric machines with high power density using LPM has been suggested in [73]. The thermal model is based on nodes to outline the mean temperature rises in a motor cylindrical component and its T-equivalent lumped parameters network, as shown in Figures 5.11 and 5.12 respectively. Using this

approach, the generated heat is assumed to be uniformly distributed, and a single mean temperature node is used to represent the heat flow, both in radial and axial directions, independently.

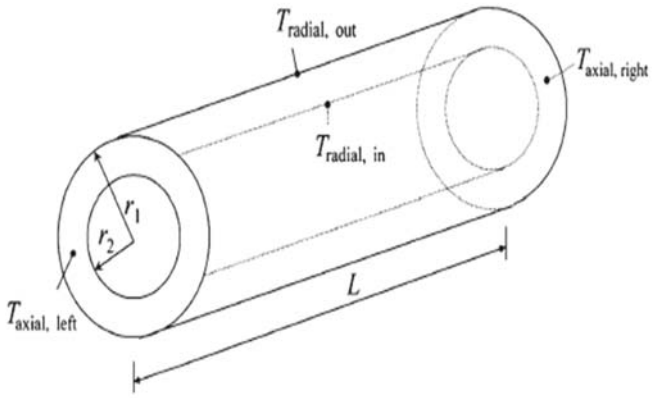

Figure 5.11 General cylindrical component with four unknown temperatures: two at the axial edges and two on the outer and inner surfaces

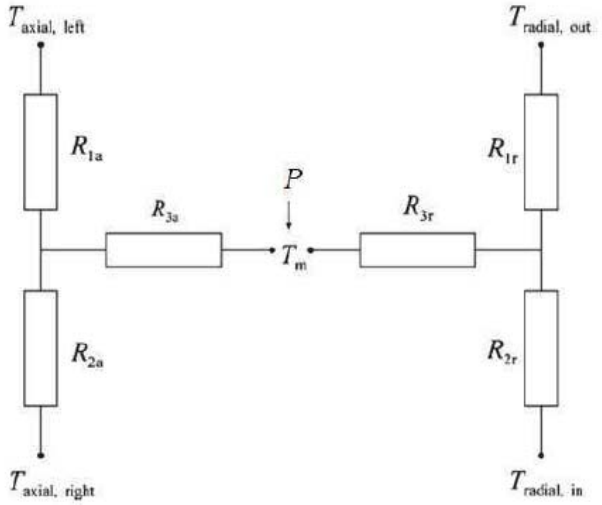

Figure 5.12 T-equivalent network represents independent axial and radial thermal resistances and average temperature node.

As shown in Figure 5.12, the T-equivalent resistance network accounts for conduction heat transfer in two networks that represent the axial and radial directions separately. Each network contains three terminals; two terminals represent the component outer

and inner surface temperatures $T_{radial,in}$ and $T_{radial,out}$ while the third terminal represents the component mean temperature T_m. The internal heat generation P is introduced in the mean temperature node. If there is no heat generation in the component, the central node will give the temperature in the network. However, if there is heat generation, the mean temperature will be the result of superposition of internal heat generation. Therefore, to obtain the mean temperature, additional thermal resistance R_{3a} and R_{3r} need to be added to connect the two nodes. The thermal resistances of each network are obtained from solutions of conduction equations in the radial and axial directions. The dimensions of the cylinder and the radial and axial conductivities λ_r, λ_a are required for the calculation [76].

$$R_{1r} = \frac{1}{4\pi\lambda_r l}\left[1 - \frac{2r_2^2 \ln\left(\frac{r_1}{r_2}\right)}{(r_1^2 - r_2^2)}\right] \tag{5.30}$$

$$R_{2r} = \frac{1}{4\pi\lambda_r l}\left[\frac{2r_1^2 \ln\left(\frac{r_1}{r_2}\right)}{(r_1^2 - r_2^2)} - 1\right] \tag{5.31}$$

$$R_{3r} = \frac{-1}{8\pi(r_1^2 - r_2^2)\lambda_r l}\left[r_1^2 + r_2^2 - \frac{4r_1^2 r_2^2 \ln\left(\frac{r_1}{r_2}\right)}{(r_1^2 - r_2^2)}\right] \tag{5.32}$$

$$R_{1a} = \frac{l}{2\pi\lambda_a(r_1^2 - r_2^2)} \tag{5.33}$$

$$R_{2a} = \frac{l}{2\pi\lambda_a(r_1^2 - r_2^2)} \tag{5.34}$$

$$R_{3a} = \frac{-l}{6\pi\lambda_a(r_1^2 - r_2^2)} \tag{5.35}$$

5.6.2 Convection

With regard to convection heat transfer, convection thermal resistances are mainly located between the components separated by air or cooling fluid. The convection heat transfer can be modelled as a single thermal resistance as in (5.36)

$$R_{cov} = \frac{1}{\alpha A} \tag{5.36}$$

Where A is the surface area of the component in contact with air and α is the convection coefficient. However, an accurate evaluation of a convection thermal resistance requires an accurate determination of convection coefficient α, which is in turn based on a set of dimensionless numbers at a given speed and circulation medium.

However, electric machines have external convection heat transfer, such as those between the frame, and ambient and internal convection heat transfer, such as the airgap between rotor and stator. In all cases, an accurate calculation of convection coefficient must be utilised, especially when fluid cooling is applied.

Considering the external heat transfer between the frame and surrounding medium. Assuming the frame is a smooth cylinder, the evaluation of the free convection coefficient α can be estimated by Churchill-Chu Equation (5.37) [77].

$$\alpha_{frame-ambient} = \frac{\lambda_{air}}{D_{frame}} \left[1.36 \frac{0.518\,(Ra)^{1/6}}{\left(1 + \left(\frac{0.559}{Pr}\right)^{9/16}\right)^{8/27}} \right]^2 \tag{5.37}$$

$For\ 10^4 \leq Ra \leq 10^9$

Where, λ_{air} is the thermal conductivity of the air, D_{frame} is the frame diameter, Ra is the Rayleigh number, Pr is the Prandtl number.

The Rayleigh number is given by (5.38)

$$Ra = \frac{g_r . k_{exp} . \Delta T . D^3}{k . v} \tag{5.38}$$

In which $g_r, k_{exp}\ and\ v$ are the gravitational constant, coefficient of thermal expansion and the kinematic viscosity of the air respectively. ΔT is the difference in temperature between the surface temperature and surrounding air.

Considering the internal convection heat transfer; the airgap between stator and rotor is deemed to be the most important location. This is because the airgap is the main heat flow path between the stator and rotor where the heat is transferred between the two main parts. To evaluate the heat transfer coefficient in the airgap, the heat flow in the airgap is assumed to be radial, so that the generated heat from the stator is transferred to the rotor surface through the airgap. Traditionally, evaluation of the convection heat transfer coefficient in the airgap requires an accurate definition of the Nusselt number so that

$$\alpha_{airgap} = \frac{N_u . \lambda_{air}}{g} \tag{5.39}$$

Where g is the radial length of the airgap and N_u is the Nusselt number defined as

$N_u = 2$ For $T_{am} < 1700$ (Laminar flow, when the machine is stationary)

$N_u = 0.128\, Ta_m^{0.367}$ For $1700 < T_{am} < 10^4$

$N_u = 0.409\, Ta_m^{0.241}$ For $10^4 < T_{am} < 10^7$

Where T_{am} is modified Taylor's number where the length of air gap and the rotor radius are taken into account as in (5.40).

$$T_{am} = \frac{Ta}{F_g} \tag{5.40}$$

T_a is Taylor's number that is used to determine the flow type in the air gap. It describes the ratio of viscous forces to the centrifugal forces as in (5.41)

$$T_a = \frac{\rho^2\, \Omega^2\, r\, g^3}{\mu^2} \tag{5.41}$$

Where Ω is the angular velocity of the rotor, ρ is the mass density of the fluid, μ is the dynamic viscosity of the fluid and r the rotor radius.

F_g is geometrical factor defined by (5.42)

$$F_g = \frac{\pi^4 \left[\frac{2r - 2.304g}{2r - g}\right]}{1697\left[0.0056 + 0.0571\left(\frac{2r - 2.304g}{2r - g}\right)^2\right][1 - 2r]^2} \tag{5.42}$$

As the airgap length is small compared to the rotor radius, $F_g \cong 1$ and $T_{am} = T_a$

5.6.3 Computation of nodal temperatures

Using the T-equivalent lumped-parameter, a thermal network for the machine was implemented as shown in Figure 5.13. The thermal network accounts for all the main components in the machine, including stator back-iron, teeth, stator winding and its insulation layers, end winding, airgap, magnet, rotor, shaft, end shafts, frame and the surrounding ambient condition.

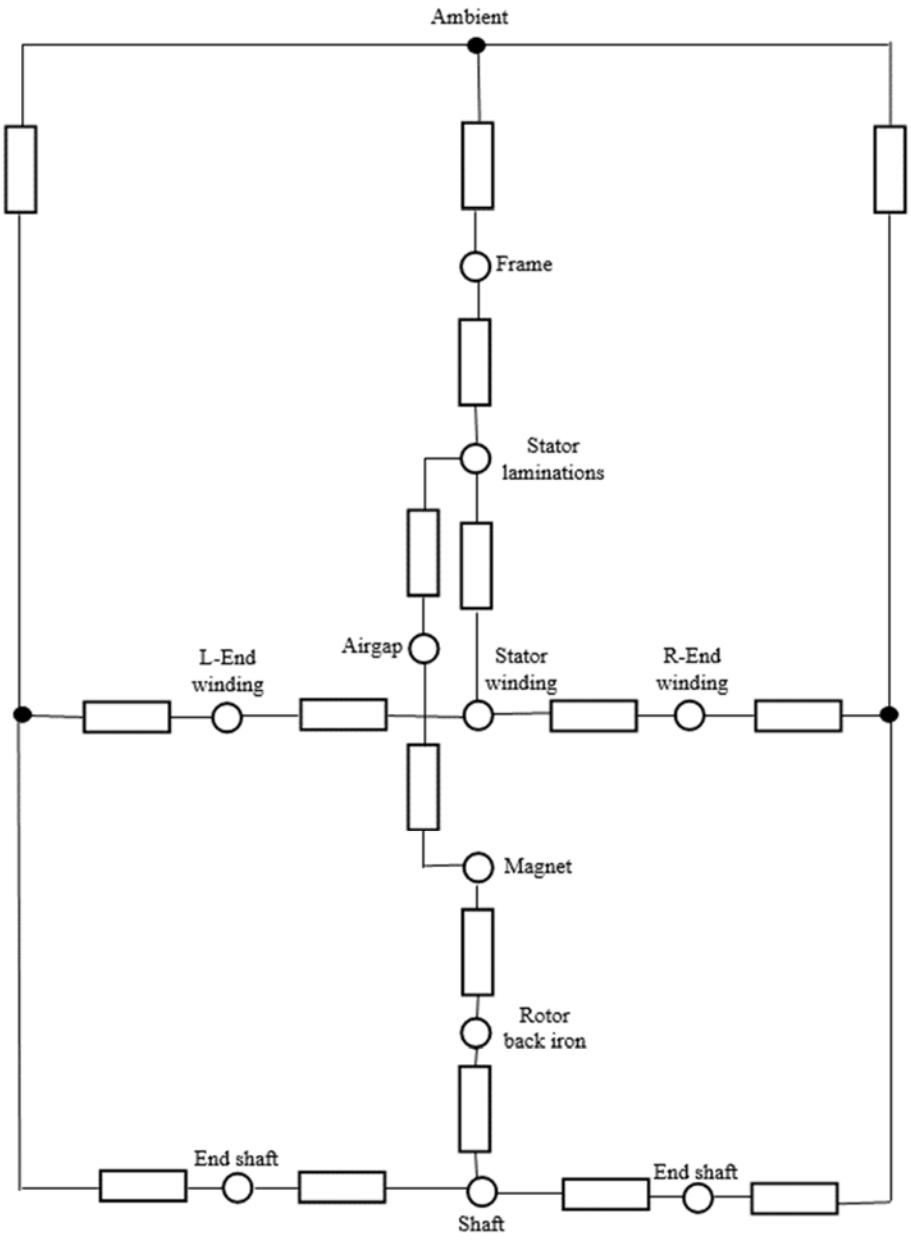

Figure 5.13 Thermal modelling network of IPMSM

Finally, the linear thermal model was written under matrix form to include all component nodes. The losses model was also integrated in the matrix to determine the temperature at each component, where magnet and copper temperatures are of interest. The influence of the magnet temperature and copper temperature was involved in the

optimisation constraint to update the properties of these materials according to the following relations

$$B_r(T) = B_{r(20)}[1 + \frac{\alpha_{Br}(T - 20)}{100}] \quad (5.43)$$

$$H_c(T) = H_{c(20)}[1 + \frac{\alpha_{Hc}(T - 20)}{100}] \quad (5.44)$$

$$\rho_{cu}(T) = \rho_{cu(20)} \left(1 + \frac{\alpha_{cu}(T_{cu} - 20)}{100}\right) \quad (5.45)$$

5.7 Constraints and penalty function

To ensure the delivery of a feasible design, the value of some parameters must be constrained up to certain maximum or minimum values. During the optimisation search, if the limit of constrained parameters has been violated, a penalty will be added to the objective function. Subsequently, the output value of the objective function will be increased, which indicates that the initialised prime variables at this particular iteration have led to a design with shortcomings and the implementation of this design will be unfeasible.

5.7.1 Armature reaction field

Armature field is the electromagnetic field generated due to the current flowing in the stator conductors. This magnetic field tends to distort the main magnetic field produced from the permanent magnet. The larger the armature current, the larger the distortion of the field. In the design of BLPM motors, an accurate determination of the armature reaction field is mainly required to predict the capability of the permanent magnet to withstand the armature field. Thus, partial or total demagnetisation can be avoided. Another important reason is that, due to the high permeability of the stator

core, a high armature reaction field from the winding may cause excessive flux density in the stator teeth and back-iron and consequently unexpected saturation should be considered. Furthermore, the determination of the armature reaction field is important to define the radial exciting forces, and hence the emitted acoustic noise, and the self- and mutual winding inductances [54].

Under normal operation conditions, the machine rated current is limited by the controller. Therefore, if the magnet thickness and coercivity are sufficiently large, there should be no risk of demagnetisation. However, in some abnormal operation conditions, such as three phase short-circuit, the current is only limited by the primary leakage inductance and winding resistance. This current is the locked-rotor current I_{LR} and is usually many times larger than the rated current. Therefore, a higher current is expected to flow in the winding and the risk of demagnetisation becomes significantly higher.

The impact of the armature reaction field is not limited only by the armature current, but also depends on the location of the permanent magnet and rotor topology. When the permanent magnet is mounted on the rotor surface, the impact of the armature reaction field is relatively weak. This is due to the large equivalent airgap with low permeable permanent magnet, physical airgap and magnet thickness, which in turn sets up a high reluctance in front of the MMF, produced from the stator current and weakening their effects. However, when the permanent magnet is buried in the rotor, the airgap is relatively small and the magnet is covered by high permeability rotor core. Thus, the reluctance of the permanent magnet is reduced and the effects of the armature reaction are higher.

From the foregoing, in order to assess machine performance and obtain a feasible prototype design, it is necessary to facilitate the optimisation process with an accurate analysis of the armature reaction field. It is also important to estimate the worst-case demagnetisation condition in the magnet and the maximum saturation level associated with the stator steel.

5.7.2 Consideration of saturation

As mentioned earlier, a high armature reaction field increases the flux density in the stator teeth and back-iron. Figure 5.14 shows the flux density in stator teeth under load and no-load conditions. Using the same stator geometries, the difference in flux density between the two cases was 0.35T. If this field is neglected, it will result in underestimation of the current needed to produce the rated torque. It will also lead to significant variation between the actual and the calculated core loss. Hence, errors are produced in the estimated efficiency and the actual performance of the machine. Therefore, it is important to consider the additional magnetic field produced from the armature and constrain the maximum flux density in the stator lamination according to the saturation point associated with the core material.

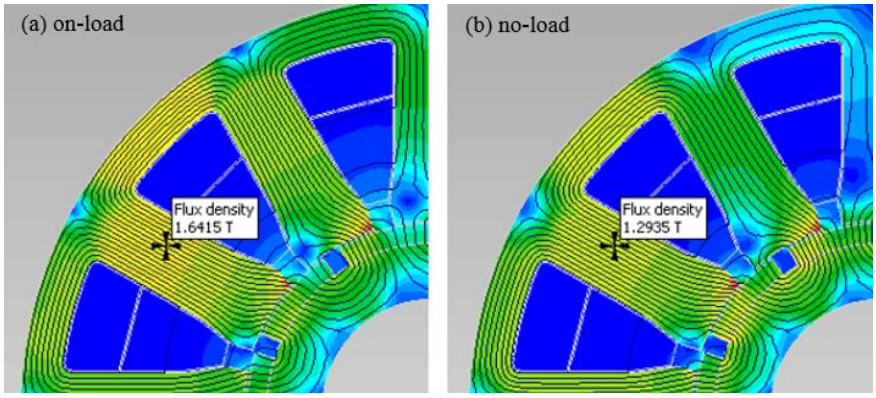

Figure 5.14 Plot of flux densities calculated by FEA at (a) full load and (b) no load operating conditions

The magnitude of the armature field is a product of magnetomotive force produced from the armature winding and airgap permeance. The permeance varies due to the presence of the slot opening. Instead of using a complex nonlinear total field, it is assumed that the airgap under the pole is uniform. Therefore, if the fringing effect was neglected, the maximum flux density in the stator teeth and back-iron is the linear sum of the magnetic field produced by the permanent magnet and the armature field given by (5.46)

$$B_{max} = B_{g(1)} + B_{arm} \tag{5.46}$$

B_{arm} is the flux density produced from the armature reaction and can be determined as in (5.47).

$$B_{arm} = \frac{\mu_0 \, \mu_r \, MMF_{arm}}{g'} \tag{5.47}$$

Where MMF_{arm} is the magnetomotive force produced from the armature, g' is the equivalent airgap length. Then, the MMF_{arm} can be determined under certain load condition as (5.48)

$$MMF_{arm} = \frac{3\sqrt{2}}{\pi} \frac{k_w \, N_{ph} \, I_{ph}}{p} \tag{5.48}$$

In this design, the maximum allowed flux density in the stator and rotor core were constrained according to the magnetic properties of the steel lamination. At the first stage of the analytical design, the width of the stator teeth and the thickness of the stator and rotor back-irons have been determined based on the knee point of the BH curve. However, to ensure unsaturated steel, a conditional formula (5.49) has been added to the design to prevent saturation.

$$B_{core} \leq B_{max} \tag{5.49}$$

For non-oriented silicon steel, the typical value of the maximum flux density is 1.6T. Therefore,

$$B_{max} \leq 1.6 \tag{5.50}$$

And the maximum flux density constrained at each component as follows

$$B_{TW,max} \leq B_{max}$$

$$B_{Sebi,max} \leq B_{max}$$

$$B_{Rebi,max} \leq B_{max}$$

Where $B_{TW,max}$, $B_{Sebi,max}$ and $B_{Rebi,max}$ are the maximum permissible flux in the stator teeth, stator back-iron and rotor back-iron respectively.

5.7.3 Protection from demagnetisation

Figure 5.15 shows demagnetisation characteristics of NdFeB 230/220h. The B-H curve is linear and repeatable for negative values of field intensity H up to the value H_k at which the magnetic polarisation vector M collapses [66]. The corresponding value of flux density is B_k; both B_k and H_k are temperature-dependent.

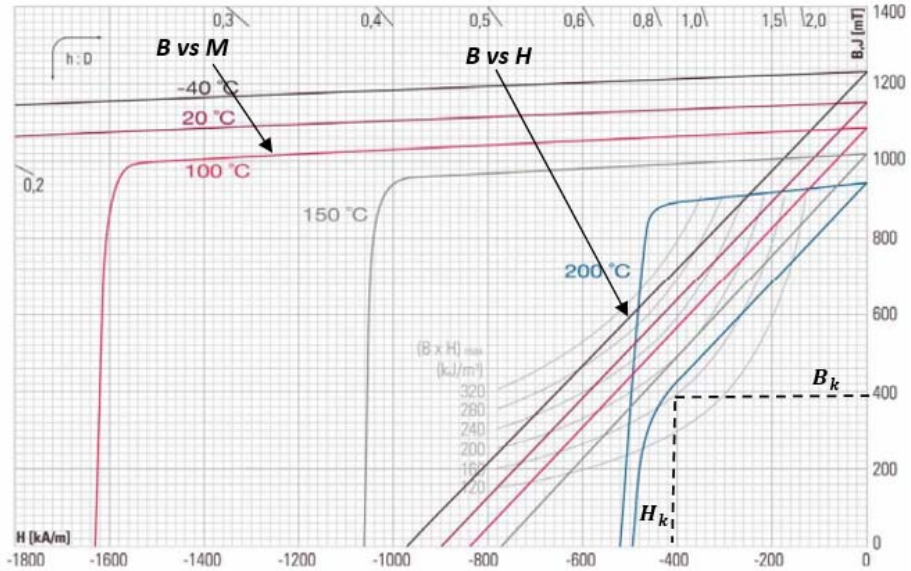

Figure 5.15 Demagnetisation characteristics of NdFeB 230/220h grade

To effectively protect the magnet from demagnetisation, the maximum permissible current under steady state and under fault conditions should be constrained against reverse fields exceeding the value H_k. Under steady-state conditions, to avoid reverse field exceeding H_k, the maximum allowed current should be less than the demagnetisation current. Therefore, the maximum phase current should be constrained according to the condition in (5.51)

$$I_{max} < I_{demag} = \frac{p\pi}{6\,\mu_0\mu_r\,(k_w\,N_{ph})} \times \left(B_m h_m - B_k(g + h_m)\right) \tag{5.51}$$

However, under fault conditions, such as three-phase short circuit, the current is limited only by the winding phase resistance and leakage inductance. Hence, it is preferred to design a large leakage inductance to limit the fault current. Subsequently, the magnet thickness should be estimated properly to withstand the high current resulting from the fault condition. Normally, the worst-case assumed is locked-rotor condition with locked rotor current I_{LR} flowing. In this case, the MMF_{arm} at locked-rotor current should be considered and the operating point of the permanent magnet must not be lower than B_k so that

$$MMF_{arm(LR)} < \frac{(h_m + g)}{\mu_0\mu_r} \times (B_m - B_k) \tag{5.52}$$

Where, $MMF_{arm(LR)}$ is the magnetomotive force produced by the armature under locked-rotor current, the locked-rotor current I_{LR} for star-connection winding is calculated as (5.53)

$$I_{LR} = \frac{V_t}{\left(R_{ph} + X_{LKG}\right)} \tag{5.53}$$

Where X_{LKG} in the reactance due to slot and end-winding leakage inductances.

5.7.4 Maximum temperature

As illustrated earlier, the properties of the magnetic material degrade proportionally with temperature rise. In permanent magnet machines, the temperature should be kept under the maximum limit to avoid deterioration in the machine's performance.

Permanent magnet and winding insulation materials are the most sensitive parts for temperature rise. From the demagnetisation characteristic of the permanent magnet, as shown in Figure 5.15, the maximum operating temperature is 200C°. If the magnet is designed to operate at this temperature, the magnet remanence and coercivity will decline at the rate of reversible temperature coefficients α_{Br} and α_{Hc}. This suggests that under an operating temperature of 200˚C, the actual remanence is 0.99 T and coercivity is 520 kA/m. Subsequently, the machine's ability to produce torque and withstand demagnetisation will deteriorate significantly. Therefore, the maximum operating temperature of the magnet was assigned as 140˚C

$$T_{PM} \leq 140°C \tag{5.54}$$

The copper resistivity increased proportionally with the increase of copper temperature. Hence, the copper loss will increase proportionally. Furthermore, a sustained 10°C increase in temperature reduces the insulation life by approximately 50%. Therefore, if the winding temperature was not constrained, an underestimation would be expected in machine performance. This will proportionally shorten the life of the machine and make the design invalid for long term running. Normally, electric machines are designed for a life time of 20 years. With the use of Class-F insulation material, the maximum temperature of the winding should not exceed 150°C. If we

allow 10°C for safety margin, the maximum winding temperature should not increase above 140°C.

$$T_{Cu} \leq 140°C \tag{5.55}$$

5.7.4.1 Maximum magnet mass

The final constraint was the maximum weight of the permanent magnet material. The machine cost is of the utmost important among the performance indices. Therefore, instead of calculating the actual cost of the machine active materials, the maximum weight of the magnet was constrained as it is the most cost effective material.

$$W_{Mag} \leq 0.53\ kg \tag{5.56}$$

5.8 Objective function

To determine the best out of a set of designs, it is not enough to say that the lightest or the cheapest or smallest is best, since a single objective rarely distinguishes overall design fitness. All of the objectives of two or more motors must be evaluated and the design with the best overall combinations of objectives will be determined to be the best motor design. Therefore, the fitness of a single design should be evaluated on the basis of multi-objectives function and a comparison among the set of designs should be based on the output value of this function.

As the objectives of the design were to minimise the machine weight, volume, cost and maximise the efficiency, the output of the objective function is determined and the fitness of each output is sorted out ascendingly. However, in some cases, where some of the objectives have more importance than others, a coefficient factor can be added to this objective to indicate its significant contribution. For example, if the design is more concerned about the volume than the weight, the volume can be

multiplied by a magnificent factor to indicate its contribution. Thereafter, these objectives should be added up to give the output of the multi-objective function as (5.57)

$$Output = W_{total} + W_{mag}\times 20 + 10\times Volume + (100 - \eta) + penalties \quad (5.57)$$

Where W_{total} is the total weight of the machine, W_{mag} is the magnet weight, "$Volume$" is the machine volume and "$penalties$" is the penalty added due to the violation of any design constraints. In the objective function (5.57), a magnificent factor of 20 and 10 have been used respectively to indicate the contribution of the volume and magnet weight and hence the machine cost, in the objective function.

6 Chapter 6: Bees Algorithm in the optimisation of electric machine design

6.1 Background

The methodology for the analytical design and all the steps in the design process for the BLPMSM were presented in the previous chapter. This chapter describes the method used to set parameters for the bees algorithm that will enable it to search efficiently for optimal values of the prime variables, as well as to evaluate their relative fitness and resulting attributes. In the subsequent chapters, the new optimised motor, based on prime variables generated in this chapter will be outlined and evaluated using FEA analysis.

6.2 Introduction

Scholars have employed various optimisation strategies to search for optimal machine parameters. The most widely used of these are genetic algorithms and particle swarm optimization, whereas the bees algorithm is an algorithm recently developed at Cardiff University, UK. The algorithm has undergone a number of improvements and is now widely applied in the solution of many complex optimization problems in engineering and manufacturing.

This work represents a new application for the bees algorithm in electric machine design. This chapter describes the basic searching criteria employed in the bees algorithm, along with an explanation of the influence of each parameter on the searching criteria. Some of these algorithm parameters are manipulated and modified in the course of the chapter in order to attain an optimal electric machine design. Finally, a number of recommendations are provided to ensure compatibility of the algorithm parameters with the values of the prime variables and search space in electric machine optimisation.

6.3 Bees Algorithm

While searching for an optimal solution, the bees algorithm follows a number of steps, as shown in the flowchart in figure 6.1. The searching processes start by spreading a number of scout bees (n) randomly in the search space. The fitness of the sites visited by (n) are evaluated according to an objective function and ranked in ascending or descending order, depending on whether the optimisation function needs to be minimised or maximised. According to these criteria, the sites with the highest fitness values are chosen as the selected sites (m) and the bees that subsequently visit these sites are chosen to perform neighbourhood searches. For this neighbourhood search, the selected sites (m) are classified into two sub-groups: elite sites (e) and non-elite sites (m-e). Then, the algorithm conducts a neighbourhood search around the selected (m) sites by assigning more forager bees (nep) to search near to the elite sites (e) and fewer bees (nsp) to search near the non-elite sites (m-e).

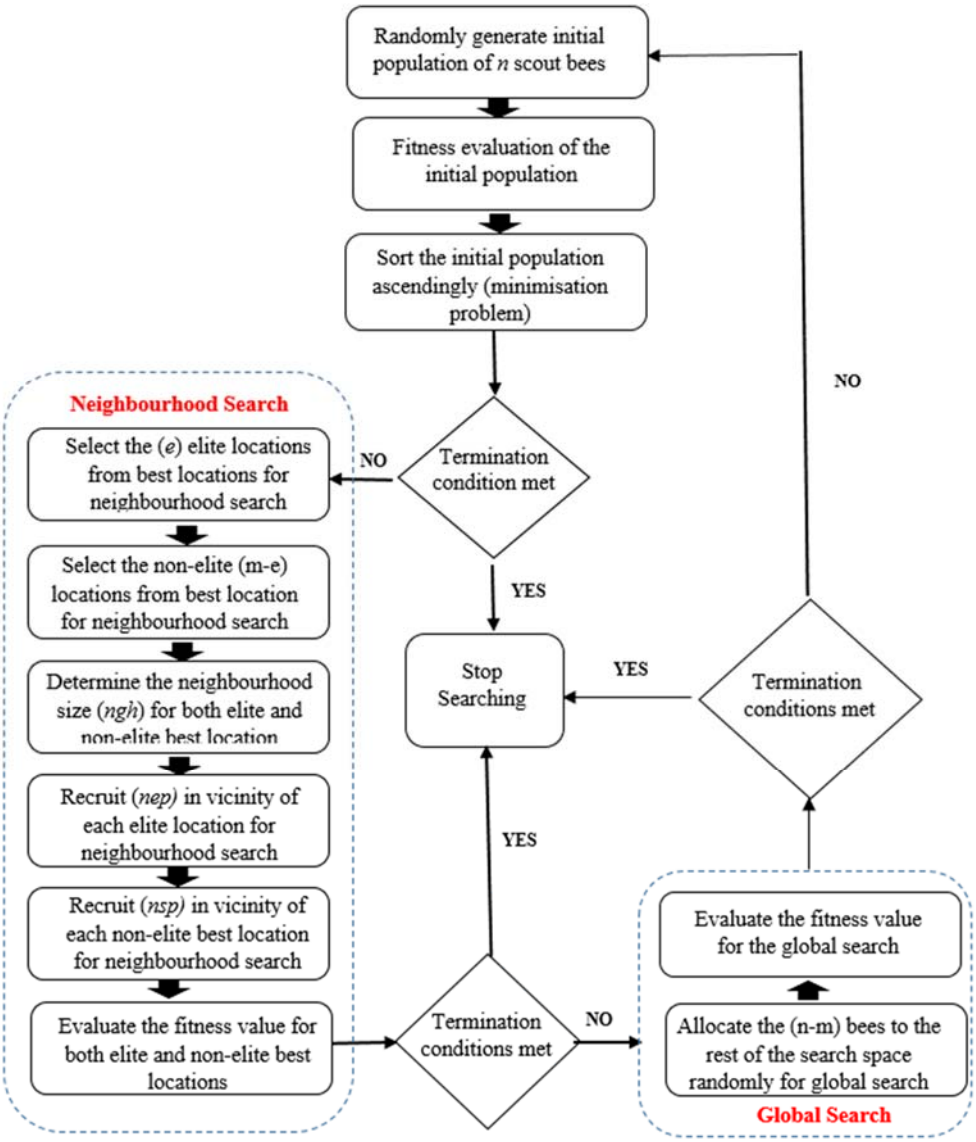

Figure 6.1 Flow chart of Bees Algorithm search criteria

Finally, in order to avoid bees being trapped at the local optima, the un-selected scout bees (n-m) are used to explore the global space search randomly. These steps are repeated until the stopping criterion is met.

From the above, it is shown that the bees algorithm performs a combination of exploitative neighbourhood searches and explorative global searches; a combination that demonstrates the strong ability of the algorithm to handle complex multi-objective

optimisation problems quickly, efficiently and reliably. According to this strategy, the searching effort is concentrated on those best, elite (e), sites that represent the more promising solution. Together with scouting, this differential recruitment is a key aspect of the bees algorithm.

6.3.1 Setting parameters of Bees Algorithm

In its standard version, Bees Algorithm requires setting the values of six parameters that must be systematically tuned to ensure an effective and compatible search for the optimal prime variables. These parameters are, the number of scout bees (n), the number of selected sites (m), number of selected elite sites (e), number of bees recruited for each elite site (nep), number of bees recruited for non-elite sites (nsp) and neighbourhood size (ngh). (El-Gallad et al., 2002) stated that properly chosen parameter values could positively influence the accuracy of the solutions and time consumed for the search process [78]. Therefore, in order to obtain the optimal solution for the optimisation problem, the algorithms' parameters need to be tuned carefully.

6.3.2 Optimisation search space

At the beginning of each cycle, the algorithm randomly initialises candidate values for the prime variables in the form of groups and spreads them in the optimisation search space. Each candidate group has a number of values equal to the number of prime variables in the optimisation problem. The number of groups is equal to the number of scout bees (n). Thus, with (4) prime variables and (50) scout bees, the optimisation will initialise 50 groups, each one containing four values, one for each prime variable.

Then, each group of the prime variables is transferred to the optimisation problem to evaluate their fitness, as shown in Figure 6.2. The optimisation problem here is the analytical design and constraints written in the form of formulae and conditional statements. However, at the end of this step, the groups will be sorted ascendingly, according to their fitness; the lower the objective function output, the greater the fitness group is.

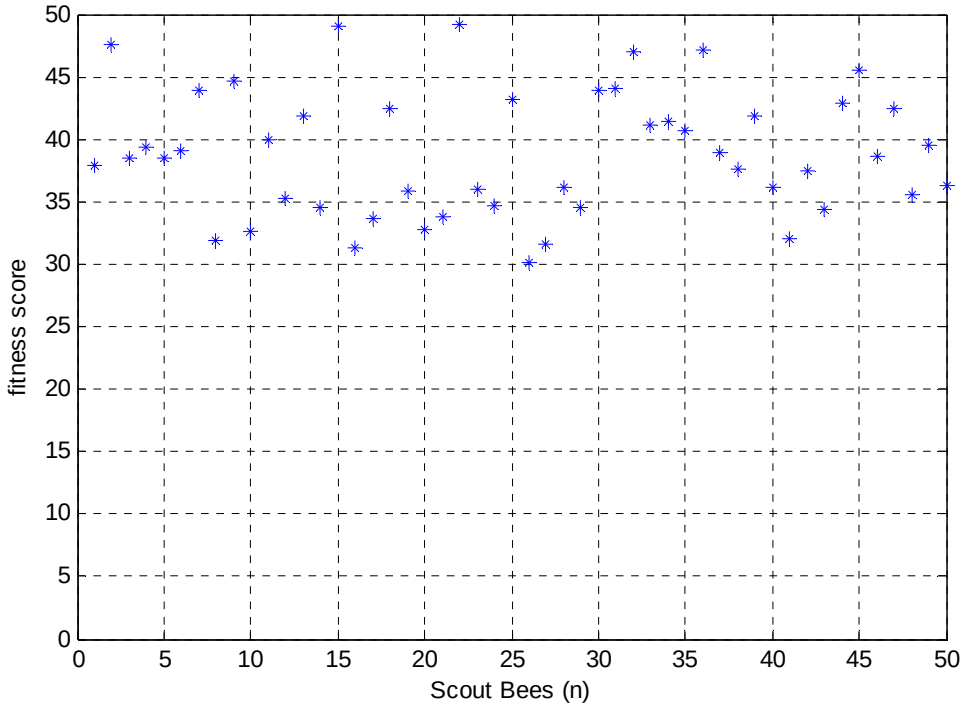

Figure 6.2 Population of 50 scout bees with their fitness evaluation

However, the search space of an optimisation is not an open space $(-inf, +inf)$; instead, there are specified global lower and upper bounds (min, max) for each prime variable. In fact, these bounds depend mainly on the designer expectation of the final design, the available resources for each prime variable, and on the dimensions of the machine.

For instance, if the current density was among the prime variables, the search space of current density J should be compatible with the recommended cooling strategy available for the design, so that, (5-7.5) A/mm^2 for natural cooling, (7.5-10) A/mm^2 for ventilation, and (10-15) A/mm^2 for water jacket, etc. Another example, when there is limited space available for the machine, is that the bounds of the axial length and stator outer-diameter should be appropriately assigned to place the machine.

Table 6.1 Upper and lower value of the prime variables bounds

Prime Variable	**Maximum bounds**	**Minimum bounds**
Inner diameter, D	150	50
Axial length, L	150	50
PM thickness, h_m	8	4
Current density, J	7.5	5

Table 6.1 shows the maximum and minimum boundaries of each prime variable as assigned in the optimisation. As shown in the table, the stator inner diameter D and axial length L have been given wider space search bounds (50-150); ~150% higher than the correspondent values in the benchmark design. This was for two reasons, on one hand, widening the boundaries allows the optimisation to attempt numerous alternative combinations that might produce a design with higher power density. On the other hand, wider boundaries take advantage of the nonlinear relation between the stator inner diameter and machine volume, therefore increases the power to volume ratio in the machine. Furthermore, with 50 scout bees and 100mm between the lower and upper boundaries limit for L and D, the optimisation will spread the values with average of 2mm between each two candidates' solution for both L and D, as shown in

Figure 6.3. The difference of 2mm in both parameters is sufficient to show a tangible difference in the machine output performance; suggesting that the number of scout bees is appropriate, with the assigned boundaries, to achieve optimisation of both axial length and inner diameter.

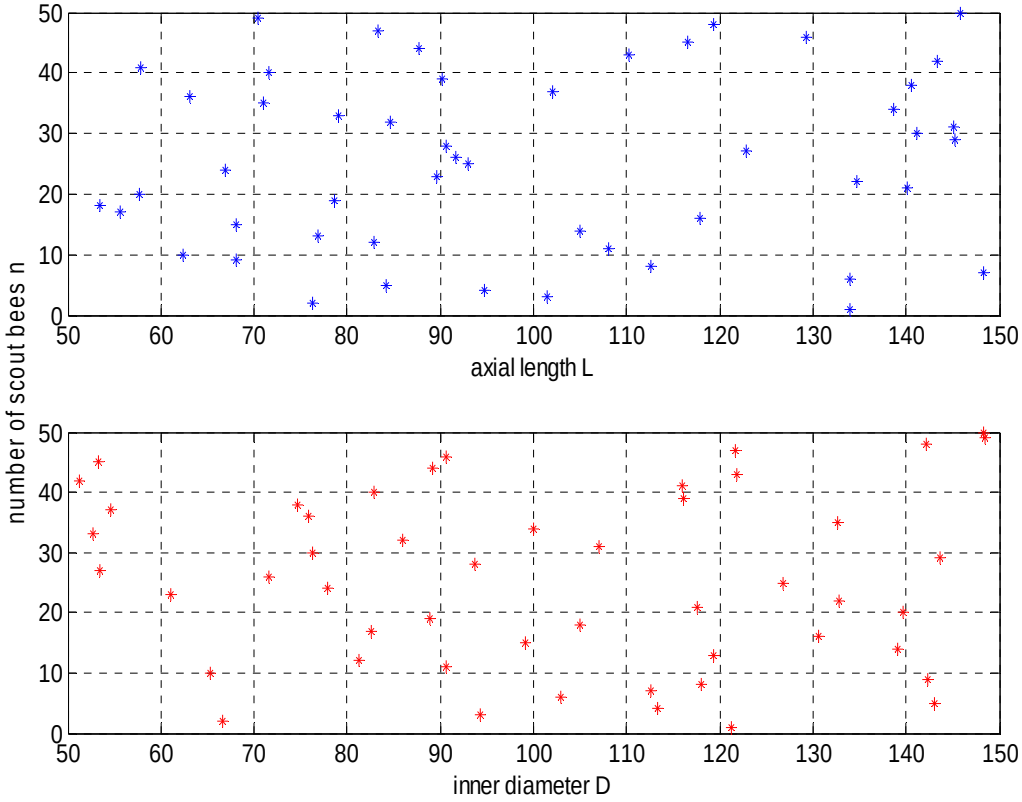

Figure 6.3 Average value between two candidates' solution for L and D

While the upper and lower values for D and L have been set for a wide bounds range, the bounds for the magnet thickness h_m and current density J were comparatively small. Regarding the current density, the available cooling for the machine is natural, so that maximum current density cannot exceed 7.5 A/ mm^2. However, the minimum bound value was set to 5 A/mm^2 to enhance the power density in the optimised design. Also, the bounds for magnet thickness were relatively small. This is to ensure the

optimisation will generate a cost-effective prototype that can resist demagnetisation with the available source of cooling.

In comparison with the prime variables D and L, the average value between each two candidates' solution for h_m and J was very small, 0.08 and 0.05 respectively. As shown in Figure 6.4, the candidate values are close to each other, so it looks as though the optimisation solution is trapped in local optima. However, the intensive search resulting from the average value being close does not cause a bad effect, as long as it is appropriate for the other parameters.

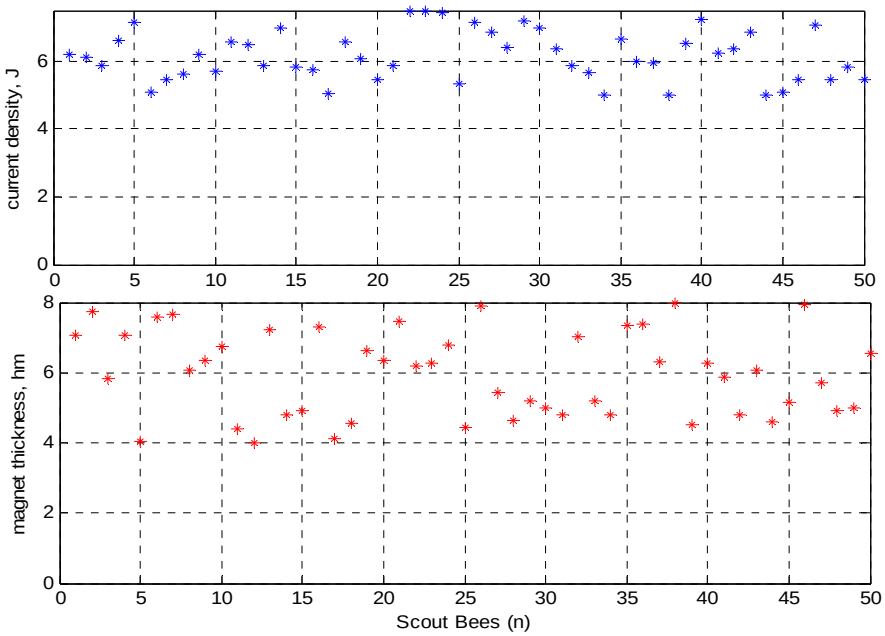

Figure 6.4 Average value between two candidates' solution for hm and J

Therefore, in order cover the whole search space, the number of scout bees (n) must be proportional to the maximum difference between the bounds of the prime variables. In our case, the maximum difference (100) was in the prime variables D and L. Therefore, the number of scout bees was set to 50 to ensure the coverage of all values in the space search.

However, after allocating appropriate maximum and minimum bounds for each prime variable, the fitness of each group will be evaluated and sorted in ascending order and transferred to the next intensive neighbourhood search.

6.3.3 Neighbourhood search

After sorting the fitness of prime variables combinations ascendingly, the algorithm begins the neighbourhood search or local search around the most promising sites i.e. selected sites (m) as shown in Figure 6.5. The number of selected sites (m) is classified into two sub-groups: elite-sites (e), which represents the top-ranking sites that have the best fitness with the most minimum output of the objective function, and non-elite sites $(m - e)$ that represents the sites with lower fitness value just below the elite sites, as shown in Figure 6.6.

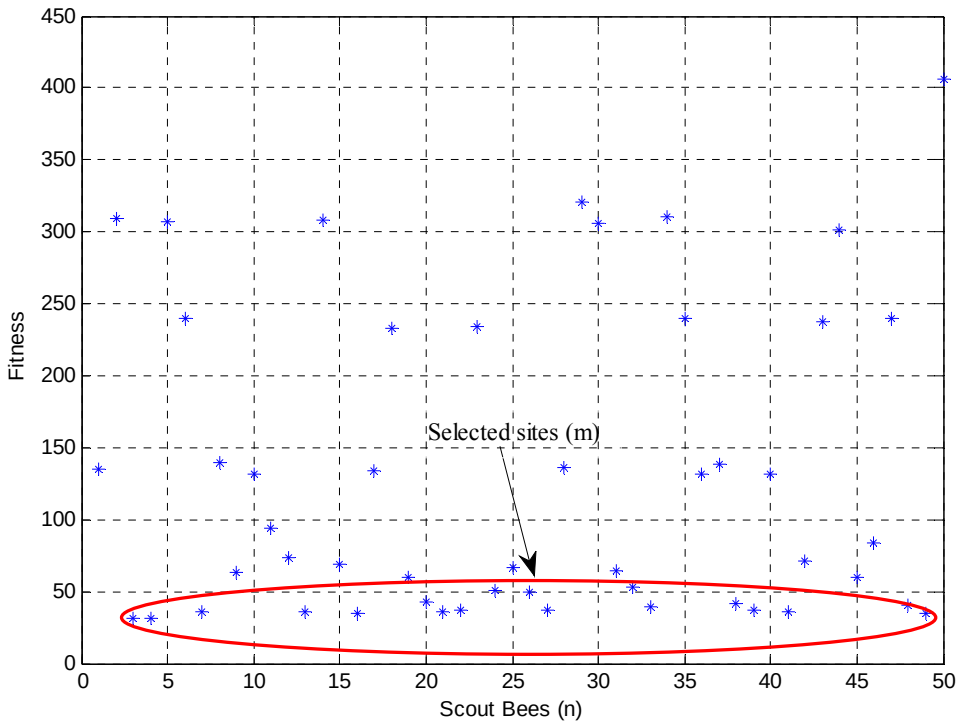

Figure 6.5 Sorting selected sites ascendingly according to their fitness

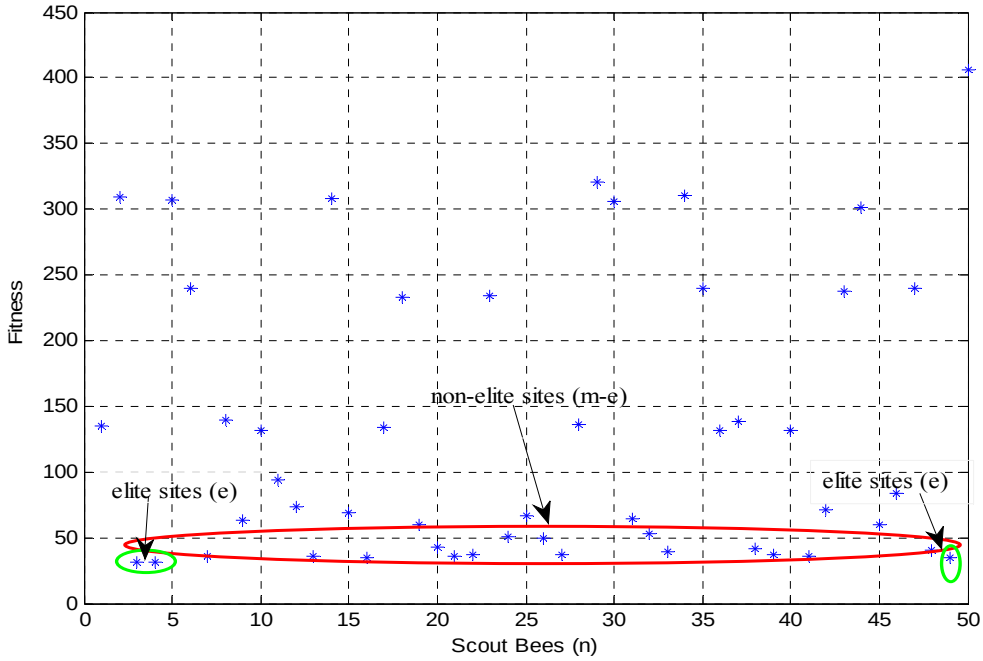

Figure 6.6 Sorting elite selected and non-selected sites according to their fitness

In the neighbourhood search, the dimension of the patch around selected sites (m) for each prime variable is performed as Equation (6.1)

$$U(:,1) = (m1 - ngh) + (2 \times ngh \times random(size(m1,1),1)) \quad (6.1)$$

Where $U(:,1)$ is the index values for the new selected site, $m1$ is the selected site, ngh is the distance between the selected site and the new search value.

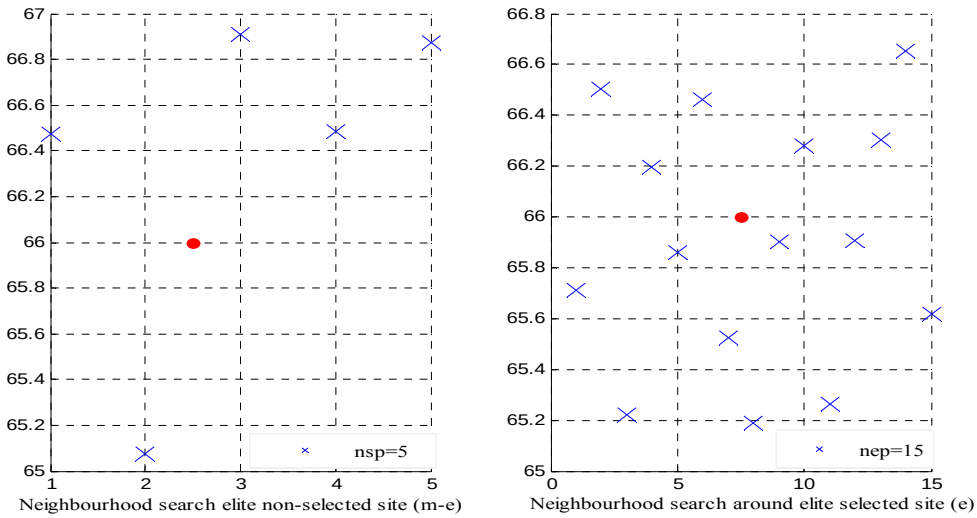

Figure 6.7 Neighbourhood search around elite selected and elite non-selected sites

Although the same neighbourhood search procedure is performed around the elite-sites (e) and non-elite sites ($m - e$), the number of bees recruited to search around each group is different, as shown in Figure 6.7. As the elite sites (e) represent the most promising sites, for the sake of speeding up the optimisation search processes, it is more convenient to intensify the search around their landscape by assigning the number of bees (nep) that is higher than the bees recruited (nsp) to search around the non-elite sites. However, the quality of the neighbourhood search around the selected sites (m) is not only limited by the number of elite or non-elite sites nor the recruited bees to search around their landscapes, but also significantly influenced by the size of neighbourhood search (ngh). A smaller neighbourhood size could intensify the exploitation effort, while a larger one could reach better solutions quickly. A smaller step (neighbourhood) size might lead to a slow convergence of the algorithm, while a larger one might miss out the spaced peaks [79].

In fact, in electric machine optimisation, the selection of neighbourhood size (ngh) depends on the bounds of the parameters being optimised and the influence of the step size on the overall machine performance. An example is clearly seen in the two parameters L and h_m. Figure 6.8 shows the new promising values generated from neighbourhood search for L and hm when the neighbourhood size (ngh) is set to 0.25 and 4.0. In both cases, the same number of bees (15) was recruited to search around elite values 66 for L and 6 for h_m. Comparatively, the axial length of the machine is much longer than magnet thickness and the bounds of machine axial length L are much wider than h_m, as shown in Table 6.1.

As shown in Figure 6.8, when neighbourhood size (ngh) was set to a small value (0.25), the maximum and minimum optimal values for L were very close to each other, between 65.85 and 66.25. It seems that an excessively small step size caused the bees to become trapped in local optima. Hence, if any of these values were generated in the final optimal solution, a machine length of 66.0mm would be adopted, as $\pm 0.25mm$ in the axial length would not have a significant difference on the machine output. In the opposite case, the new promising values for h_m range between 5.9mm and 6.2mm. In this case, the difference between the two values 0.3mm has a whether reasonable effect on the cost and demagnetisation protection and therefore on the objective function.

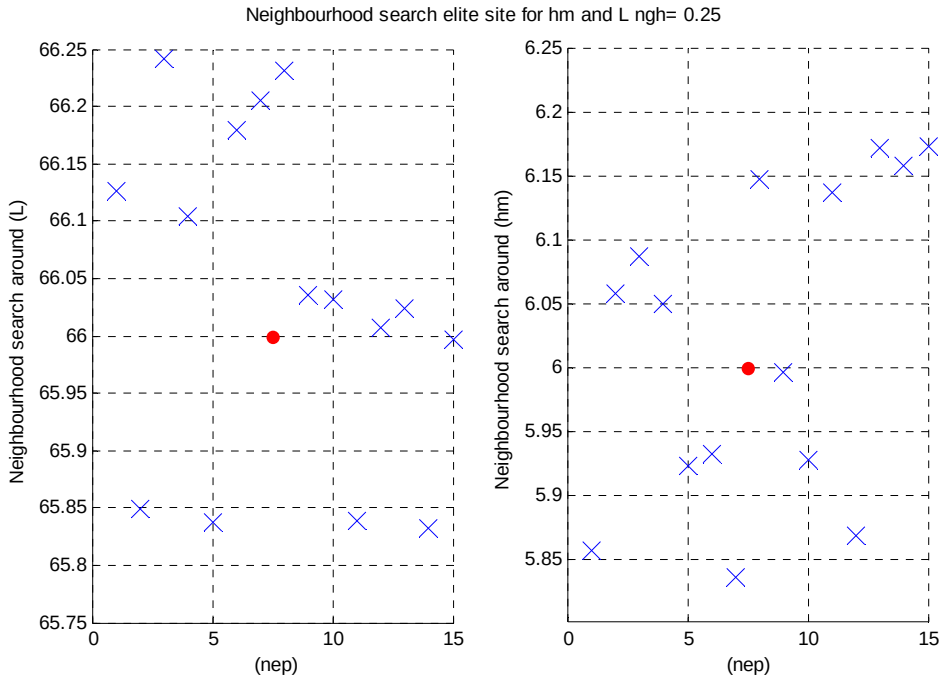

Figure 6.8 Neighbourhood search around selected L and h_m, ngh=0.25

On the other hand, as shown in Figure 6.9, when the neighbourhood size (ngh) was set to a relatively higher value (4.0), the new promising values for L ranged between

62mm and 70mm. Hence, each individual value represents different axial length that relatively can have a reasonable impact on machine performance. Consequently, it can guarantee that the neighbourhood search was consumed with evaluating a genuine dimension of the machine. In the opposite case for prime variable h_m, when ngh was set to 4, many of the new solutions generated have violated the bounds of the parameter h_m and therefore the constraints. Consequently, these solutions will be rejected as they cause additional penalty on the objective function.

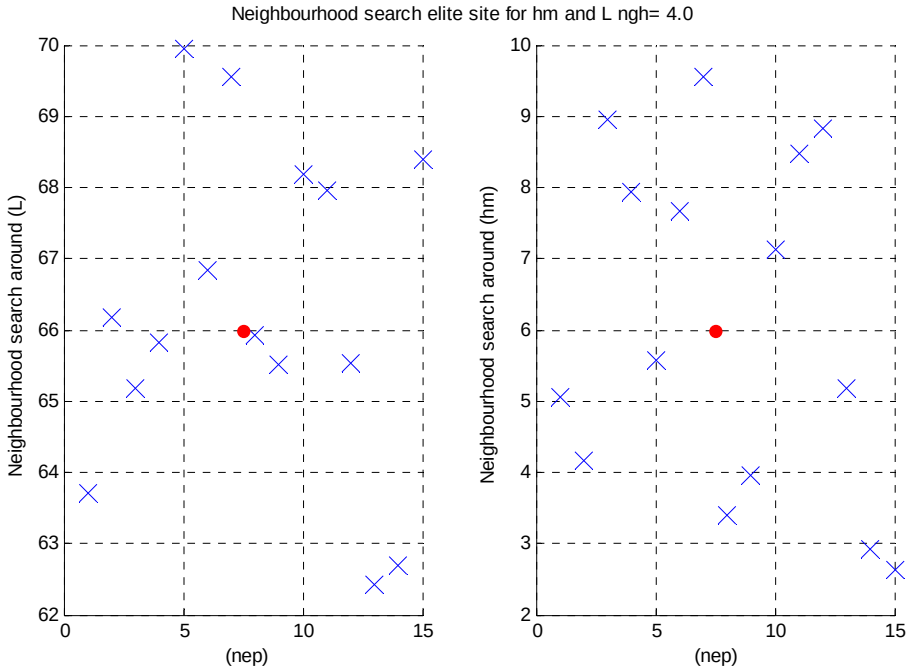

Figure 6.9 Neighbourhood search around selected L and h_m, ngh=4.0

However, the neighbourhood size (ngh) is not necessarily to be kept constant throughout the optimisation. The adaption of large ngh value for prime variable with broad bounds can help the bees to reach an optimum solution faster and more efficiently and will influence their value on the objective function. On the other hand, for prime variables with narrow and limited bounds, a smaller value of ngh can avoid

the algorithm generating new promising values outside the prime variable bounds and intensify the search on more optimal solutions.

6.3.4 Global search and stopping criteria

After completing the neighbourhood search, the algorithm allocates the rest of the bees $(n - m)$ to perform a global search to the non-best locations. The global search is necessary to avoid bees being trapped at local optima. At the end of each iteration, a new list of scout bees was formed, comprising the fittest solutions from each neighbourhood (neighbourhood search results), and the new randomly generated solutions (global search results). As the number of iterations (itr) increased, the convergence to the optimal solution increased progressively. Figure 6.10 shows how the optimal values of each prime variable keep changing throughout optimisation. Also, it is shown how the objective function outputs improved after each iteration, until it reaches its optimal value at iteration 28 in Figure 6.11. All the solutions found after this iteration have objective function outputs greater than the value achieved at iteration 28. The reason for the optimisation to continue the search is that the stopping criteria were set to the maximum number of iterations (50). In the case of a small number of iterations that have been adopted, the algorithm will not have enough chance to explore the entire search space to achieve an optimal solution. Therefore, the higher the number of iterations, the greater the cover of the optimisation search space.

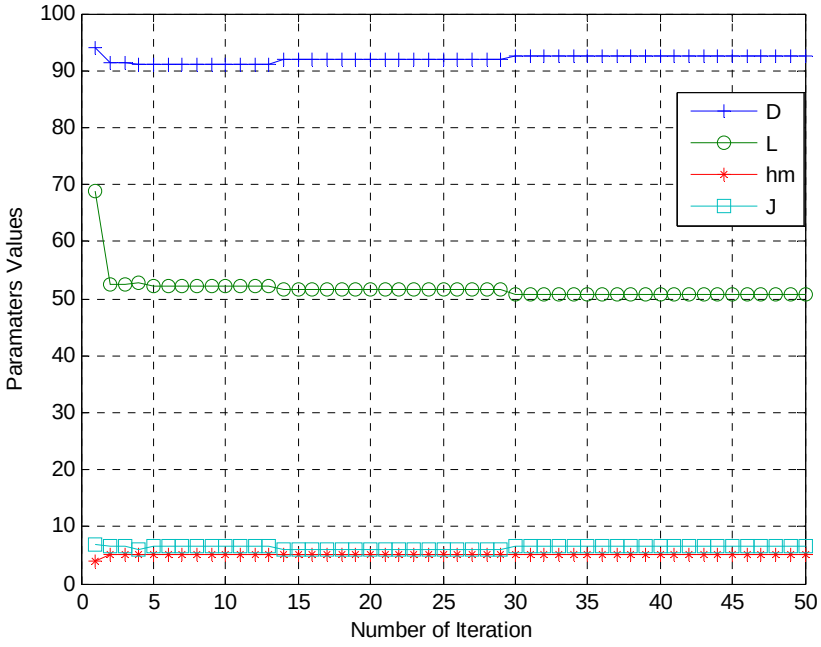

Figure 6.10 The optimal values of prime variable at each iteration

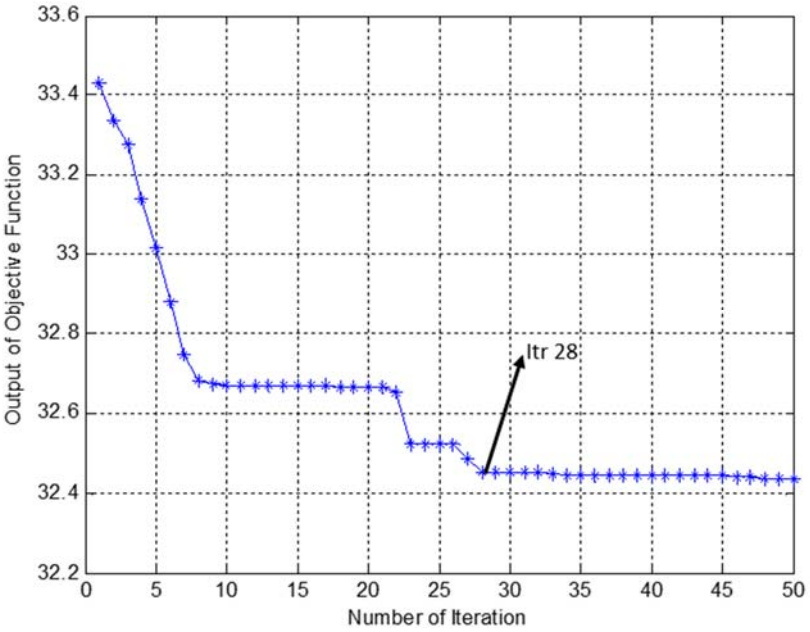

Figure 6.11 The output of the objective function for 50 iterations

Finally, Table 6.2 shows how the Bees Algorithm parameters were set for the purpose of this machine case. However, if the optimisation target was modified to search for

different prime variables or the operating condition of the machine has been changed, the optimisation parameters should be changed to suit the new search criteria accordingly.

Table 6.2 The BA parameters setting as used in this research.

Parameter	Value
Scout bees, n	50
Selected bees, m	10
Elite bees, e	2
nep	15
nsp	5
ngh1 (for $\boldsymbol{h_m}$ and J)	0.25
ngh2 (for D and L)	4
No of iteration	50

6.4 Comparison between Bees and Genetic Algorithms in the optimisation of electric machine design

According to "No Free Lunch Theorem", if an algorithm performs well on certain class of problems; then it necessarily pays for that with degraded performance on the set of all remaining problems [3]. Therefore, there is no ideal algorithm, which works perfectly for all optimization problems; instead the perfect optimization is the one that able to cover all the searching space efficiently with less number of iterations as well as avoids stagnation on local solutions. Therefore, this section focuses on comparing between Bees Algorithm (BA) and Genetic Algorithm (GA) in terms of computational efficiency and ability find optimal solution for electric machine design with less number of iterations.

6.4.1 Design operational conditions and specifications

To compare between two optimisation algorithms fairly, an objective function with similar fitness value must be predefined as benchmark for both optimisations. In this comparison, however, a target electric machine design with certain operational conditions and objectives that are specified by "FReedomCAR and Vehicle Technologies" FCVT was selected as a benchmark. The operational conditions of the target machine were detailed by "Unique mobility Technologies Inc" UQM [80] as shown in Table 6.3 and graphically illustrated in figure 6.12. Thus, the motor should develop 262.5Nm torque at constant torque region below 2000 rpm and 55 kW at constant power region between 2000 and 10000 rpm. The peak operating profile is required over the entire voltage range of 200V-400V (typical value of 325V), and maximum current of 400A.

Table 6.3 UQM requirements for traction motor

Requirement	Specification
Maximum speed [rpm]	10,000
Peak Power@20% Max. speed [kW]	55
Battery Operation Voltage [V-dc]	200-450
Max. motor current [A]	400
Characteristics Current [A]	<400
BackEMF@100%Max.speed [V-LL]	<600
Life [year]	>15
Ambient Temperature [˚C]	-40 to +105

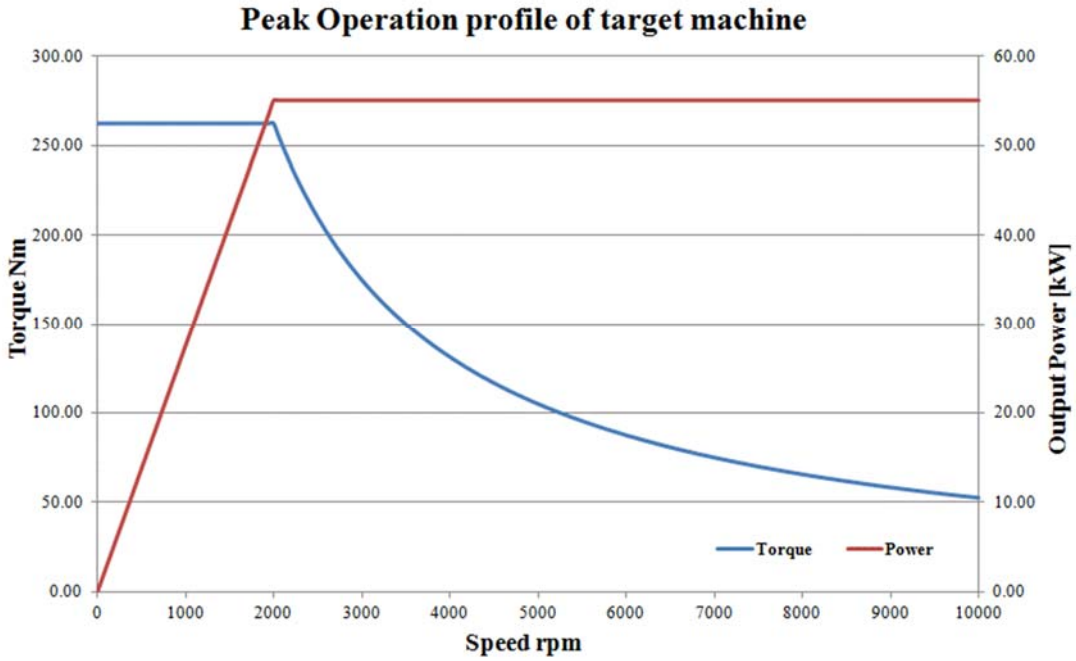

6.12 Design characteristics for output power and torque vs speed

However, the target machine specifications are given in Table 6.4 in terms of weight (W), volume (V), efficiency (η) and cost (S). The total weight of the machine and volume should be less or equal to 20 kg and 4.4 litres respectively and the minimum efficiency is 93%. The cost of the machine was provided from approved supplier based on 200.000 motors annually. The total cost is assumed for the prices of steel laminations 6.45 $/kg, copper 9.27 $/kg and permanent magnet 44.85 $/kg. However, the maximum cost of the materials shouldn't exceed 176 $/KW. Therefore, these four performance indices will be reformulated into one multi-objective formula to determine the benchmark fitness value as in Equation (6.2). However, an additional toe four performance indices, a penalty was added to the objective function to indicates for any violation in the main four indices or any other constraints in the algorithm.

$$Output = W + V + S - (1- \eta) \times 100 + (pn) \quad (6.2)$$

Table 6.4 specifications of the target machine design

Performance Index	UQM Specification	Objective specifications
Weight (W)	> 2.75 [kw/kg]	≤ 20
Volume (V)	> 12.5 [kw/Liter]	≤ 4.4
Efficiency (η) [%]	> 93	≥ 93
Cost (S) [$]	< 3.2 [$/kW]	≤ 176

6.4.2 Objective function

The procedure of the analytical model method as previously shown in figure 5.1 has been used to calculate the electromagnetic and thermal parameters of the target machine. In the analytical model six prime variables were considered that are; the stator inner diameter (D), machine axial length(L), thickness of permanent magnet(h_m), number of conductor per slot(Nc), current density(J) and current advance-angle (δ).

The method of calculating the machine's weight and volume has been specified in UQM report. Thus; the weight of the machine is referred to active materials in the stator and rotor core laminations, copper in the stator windings and magnets only. The volume calculation includes a simple cylindrical where the diameter is the outer diameter of the stator and a length over the axial end-turn of the winding. According to the design specifications, the value of the objective function that satisfies the design specifications is the sum of the maximum value of each performance index and equal to (193.4).

6.4.3 Optimisation Results analysis and comparison

Both BA and GA are stochastic process algorithms that depend on random initialization of the prime variables. Therefore, to assess the ability of an algorithm to cover the search space, the number of iterations, the maximum and minimum boundaries of the prime variables and the stopping criteria must be the same for both optimisations. The other optimization searching parameters, such as number of scout bees in the BA and populations in the GA, have been tuned to generate best fitness values that compatible with each algorithm searching criteria. Following this procedure, the parameters for both optimisations were set as shown in Table 6.5. The number of iterations assigned for each algorithm is 100. These allow the optimization to cover wider search-space area looking for the optimal solution. In the BA, the number of scout bees (50) was used to evenly participate between the local search with 25 bees (*nep*+*nsp*) and in the global search with another 25 bees (n-m). Also, the neighbourhood size in BA and the migration factor in GA were set to 1 which means that a search will be implemented around each proposed elite and best prime variable values within a radius of one unit.

Table 6.5 Setting parameters of the Optimization algorithms

Parameter	BA	Parameter	GA
No of Iterations	100	Generation	100
Scout Bees (n)	50	Population	50
No. of selected elite I	2	Elite count	2
No. of Selected Best (m)	10	Mutation	10
No. of bees around m (nep)	15	Crossover	40
No. of bees around e (nsp)	10		
neighbourhood size	1	Migration factor	1

The quality assessment of both algorithms will be assessed according to their computational efficiency to solve the optimization problem and absolute differences between the resulted best fitness value from each run and the benchmark value. Both optimisations algorithms were run for 10 times and the values of the objective function obtained from each run are shown in Table 6.6.

Table 6.6 Setting parameters of the Optimization algorithms

BA Fitness Value	GA Fitness Value
192.3	190.1
194.7	195.1
192.3	190.2
192.4	196.3
190.5	191.2
191.2	194.6
191.5	193.2
194.4	191.2
191.2	196
191.1	198.1

Using the best fitness value (193.4) as a benchmark to evaluate the output of the objective functions; both BA and GA were able to find optimal solution within the 10 runs. However, the computational efficiency of an intelligent algorithm is evaluated as the number of runs needed for the algorithm to find optimal solution that is better than a benchmark value. Providing that the number of iterations in BA is equal to the number of generations in GA; and the number of scout bees in BA is equal to the number of populations in GA; the results showed that BA was able to find objective function value that is better than the benchmark objective value in 8 runs while GA has found it in 5 runs only. Thereafter, the probability to find good optimal solution in

BA is higher than GA (80% vs 50%). Furthermore, considering the average value of the obtained objective function from each algorithm, BA has shown the lowest average fitness value (192.16) comparing with (193.6) for GA and out of the total runs the standard deviation of BA was lower than GA (1.01 vs 2.82) respectively as shown in Table 6.7.

Table 6.7 Results from BA and GA

	Best fitness	**Worst fitness**	**Average fitness**	**Probability [%]**	**Std. Deviation**
BA	190.5	194.7	192.16	80	1.40
GA	190.1	198.1	193.6	50	2.82

As stated before, the perfect optimization is the one that is able to cover all the searching space efficiently with less number of iterations. The searching space in the BA is mainly determined by the number of iterations and number of scout bees and neighbourhood size while in GA it is determined by the number of generations, population size and migration factor. To observe the effect of covering the searching space, the parameters for both optimizations were tuned again as shown in table 6.8, and the obtained results were recorded from 10 runs as shown in table 6.9.

Table 6.8 New Setting of Optimization algorithms

Parameter	**BA**	**Parameter**	**GA**
No of Iterations	50	Generation	50
Scout Bees (n)	20	Population	20
No. of selected elite (e)	2	Elite count	2
No. of Selected Best (m)	5	Mutation	10
No. of bees around m (nep)	8	Crossover	40
No. of bees around e (nsp)	4		
neighbourhood size	± 0.5	Migration factor	± 0.5

Table 6.9 Results from new setting of BA and GA

	Best Fitness	**Worst fitness**	**Avg. fitness**	**Std. Deviation**
BA	192.5	201.3	195.5	3.85
GA	197.5	218.6	206.2	9.9

The results show the best fitness value obtained from BA (192.5) was lower than the benchmark value and the average value obtained from BA is lower than that in the GA 195.5 and 206.2 respectively. However, comparing the worst fitness values in both algorithms with the benchmark, a big variation can be observed in GA and its standard deviation is much higher than BA.

From multiple runs of the algorithms, the obtained results show that BA has better computational efficiency and higher probability to find solution with better fitness than the benchmark fitness. Also, the average best fitness value achieved from BA also was lower than this value achieved by GA. When the space search is reduced; BA has shown higher ability to cover the search space and find more fitness solution.

7 Chapter 7: Optimisation results and verification of optimised BLPMSM

7.1 Introduction

In the previous chapters, the analytical design methodology in the design of BLDC motor and all the parameters setting for BA in the search process have been described. In this chapter, the optimal prime variables generated from running BA are used to build a new BLPMDC prototype. All the dimensions and electromagnetic, as well as thermal, analysis of the new optimised motor will be evaluated and verified based on FEA.

7.2 BA Results

Each motor design has a set of prime variables that fully describe the construction of the motor. The design prime variables are determined through a combination of neighbourhood and global search processes. The local search is performed around the most promising sites that having minimum objective function and the global search is performed randomly in the space search to avoid optimisation being trapped on local optima. Thus, the entire search space within the scaled range of upper and lower bounds is efficiently searched thoroughly.

At the end of each iteration cycle, a new combination of prime variables i.e. elite sites having the most minimum objective function output, is saved as the best. Thus, at each cycle, a better motor design is determined to dominate the previous design. If the fitness of the objective function lowers fitness value, the combination of the prime variable from the previous iteration will dominate the new one. Thus, the fitness of the objective function never decreases. Table 7.1 shows the optimal prime variables and the output of the objective functions generated from running the optimisation five times. The table also includes evaluation of the performance indices weight, volume, magnet weight and efficiency achieved at each run. From the table, it can be observed that although objective functions have approximately the same outputs value at all runs, the optimisation generates different optimal values for the prime variables.

Table 7.1 Generated optimal prime variables from BA

Parameters	Benchmark parameters	Result-1	Result-2	Result-3	Result-4	Result-5
D [mm]	58.3	82.25	81.5	82.44	81.93	83.15
L [mm]	114	50.87	51.08	50.05	50.16	50.4
h_m [mm]	4	5.88	5.87	5.93	5.96	5.85
J [A/mm^2]	5.5	6.9	6.9	7.12	6.88	7.33
Total mass [kg]	7.92	6.69	6.64	6.64	6.62	6.67
Magnet mass [kg]	0.53	0.407	0.404	0.405	0.406	0.404
Volume [Litre]	1.64	1.015	1.008	1.00	1.00	1.017
Efficiency [%]	90.2	89.17	89.03	89.04	89.00	89.2
Objective Function	44.92	35.81	35.78	35.73	35.76	35.75

As shown from the results, the stator inner diameters and machine axial lengths were different from each other and ranged between (81.5mm-83.15mm) and (50.05mm-51.8mm) respectively. The values of magnet thicknesses and current densities were very close to each other and ranged between (5.85mm-5.96mm) and (6.88-7.33) A/mm^2 respectively.

In terms of the performance indices, each run has one best value either for total weight, volume, magnet weight or efficiency. The lowest motor weight was achieved at the fourth (6.62kg) and therefore the least volume at the same run (1.00 Litre). In terms of magnet weight and efficiency, the best values were achieved at the second and fourth runs respectively. Thus, if the main target for the optimisation was to search for minimum weight and volume only, the prime variables from the fourth run will be suitable. And if the main target for the optimisation was to search for maximum efficiency, the second or fourth run would be more suitable. However, when the optimisation has multi objectives, a single performance index is not sufficient to distinguish design fitness; instead, the combination of all the performance indices must be evaluated and the design, with the overall minimum value of the objective function, will be determined as the best motor design. Therefore, the best fitness value of the objective function, which combined all the performance indices, was achieved at the third run with objective function value of (35.73). Hence, the prime variables in the third run will be used to create the optimised motor.

7.3 Analytical design verification

In this section, an analytical design example of the optimised machine is presented to describe how the four optimal prime variables are used to generate the complete

machine design. The 1.75kW BLDC is designed to produce a torque of 26.1 N.m at 640rpm. The proposed machine is designed to have full pitch concentric winding around nine slots in the stator. The optimal values for the four prime variables as shown in Table 7.2, with the minimum objective function generated from the third run, will be used to build the construction machine.

Table 7.2 Values of prime variables generated from BA optimisation

Parameters	**Result-3**
D [mm]	82.44
L [mm]	50.05
h_m [mm]	5.93
J [A/mm^2]	7.12

As described in previous chapters, values of several machine dimensions have been selected outside the optimisation search to eliminate the search process and to ensure that all component dimensions will fit together. The values of these predetermined parameters are kept unchanged throughout the optimisation search. Furthermore, several constraint values of magnetic and thermal parameters have been involved in the optimisation problem. Therefore, if the boundaries of the constraints have been violated throughout the optimisation search, a penalty will be added to the objective function to indicate that this design is unfeasible and, therefore, the generated prime variables will be excluded from the optimisation.

7.3.1 Airgap flux density calculation

In addition to the length of electromagnetic airgap g and the properties of the permanent-magnet material represented by B_r and μ_m, the calculation of the airgap

flux density requires the dimensions of the stator inner diameter D, the active machine length L and the thickness of the permanent magnet h_m, all generated from the optimisation. A typical value of airgap 0.5mm was chosen for 1.75kW at 640rpm BLDC machine, which is the same value used in the benchmark design. The residual flux density B_r for the permanent magnet NdFeB 230/220h at 20° is 1.16T. However, the PM operating temperature is estimated to be 140°. Therefore, with temperature reversible coefficient α_{Br} of -0.08%K, the residual flux density is inclined to 1.0486T and the relative permeability μ_r is 1.1.

$$B_r(T) = B_{r(20)}[1 + \alpha_{Br}(T - 20)/100]$$

$$B_r(140) = 1.16\times\left[1 - \frac{0.08\times(140 - 20)}{100}\right] = 1.0486T$$

In the surface mounted rotor, the effective length of the airgap g' is determined by taking the Carter coefficient k_c into account. As shown in Equation (3.28), the Carter coefficient is calculated with consideration that the equivalent airgap length g_{eq} is equal to the physical length of the airgap g and the thickness of the permanent magnet h_m and its relative permeability μ_r as follows:

$$g_{eq} = g + \frac{h_m}{\mu_r} = 0.5 + \frac{5.93}{1.1} = 5.89mm$$

The width of the slot-opening B_{so} is assumed to be 2mm. Thus, based on Equation (3.29) the tooth pitch τ_s is

$$\tau_s = \frac{\pi.D}{N_m} = \frac{\pi.82.44}{9} = 28.777mm$$

And from 3.30, the factor γ is expressed as

$$\gamma = \frac{4}{\pi}\left[\frac{B_{so}}{2\,g_{eq}}\tan^{-1}\left(\frac{B_{so}}{2\,g_{eq}}\right) - \ln\sqrt{1+\left(\frac{B_{so}}{2\,g_{eq}}\right)^2}\right]$$

$$\gamma = \frac{4}{\pi}\left[\frac{2}{2\times 5.89}\tan^{-1}\left(\frac{2}{2\times 5.89}\right) - \ln\sqrt{1+\left(\frac{2}{2\times 5.89}\right)^2}\right] = 0.0183$$

The Carter coefficient k_c is then calculated per 3.28

$$k_c = \frac{\tau_s}{\tau_s - \gamma.g_{eq}} = \frac{28.777}{28.777 - 0.0183\times 5.89} = 1.0038 \cong 1.00mm$$

And equivalent length of the airgap g',

$$g' = g\times k_c = 0.5\times 1 = 0.5mm$$

For accurate determination of the airgap flux density, a reluctance factor should be considered to compensate for the dropped MMF in the magnetic circuit due to saturation in the stator lamination. The reluctance coefficient depends mainly on the machine size with typical value higher than unity and range between (1.0-1.2). However, for small electric machines like this prototype, this factor can be neglected if the steel is not saturated. As the maximum limit of saturation in the magnetic circuit has been constrained through optimisation, this factor can be omitted without affecting any deviation in the airgap flux density.

The leakage factor f_{LKG}, which accounts for the magnetic flux-lines that return to the PM without linking the stator winding, is considered. Again, this factor depends on

the machine size with a typical value lower than unity and ranges between (0.9-1.0). Therefore, a leakage factor of 0.95 has been considered.

Finally, with the selected value of 0.83 for the magnet coverage coefficient α_p, all the parameters are now known to calculate the flux density airgap B_g at temperature 140° based on Equation (3.34).

$$\mathrm{B}_g = \frac{f_{LKG} \,.\, \alpha_p \,.\, \mathrm{B}_r}{1 + \frac{f_{LKG} . g' . \mu_m . \ \alpha_p}{h_m}}$$

$$\mathrm{B}_g = \frac{0.95 \times 0.83 \times 1.05}{1 + \frac{0.95 \times 0.5 \times 1.1 \times 0.83}{5.93}} = 0.7706T$$

The first harmonic of the airgap flux density $B_g(1)$ is calculated as in Equation (3.36)

$$B_g(1) = \frac{4}{\pi} Bg \ sin\left(\frac{\pi . \alpha_p}{2}\right)$$

$$\frac{4}{\pi} \times 0.7706 \times sin\left(\frac{\pi \times 0.83}{2}\right) = 0.9463 \ T$$

7.3.2 Tooth width and stator and rotor lamination thickness

From the first harmonic value of the airgap flux density, the widths of stator teeth T_w and the thicknesses of the stator and rotor back-irons S_{ebi} and R_{ebi} can be determined. The calculation of these dimensions requires the value of the fundamental flux-per-pole $\Phi_{(1)}$ produced by the permanent magnet, which can be determined from Equation (5.3)

$$\Phi_{(1)} = B_{g(1)} . A_g$$

$$\Phi(1) = \frac{2}{\pi} \frac{L.\pi D B_g(1)}{Np}$$

$$\Phi(1) = \frac{2}{\pi} \times \frac{50.05\times \pi \times 82.44 \times 0.9463}{8} = 0.9761\times10^{-3}\, Wb$$

7.3.2.1 Thicknesses of stator and rotor yokes

Based on the properties of steel laminations, the average flux density in the steel due to permanent magnet excitation should not exceed the knee point B_{knee}. For most non-oriented steel, this value ranges between (1.3-1.45) T. However, as shown in Figure 5.6, the B_{knee} for M330-35A steel is read off as 1.35T. The lamination stacking factor k_s has a typical value of 0.95 that is considered to compensate for the gaps between laminations. Therefore, S_{ebi} and R_{ebi} can be computed as Equations (5.4) and (5.5)

Stator back-iron S_{ebi}

$$S_{ebi} = \frac{\Phi_{(1)}}{2\, B_{knee}\ \mathrm{L}\, k_s}$$

$$S_{ebi} = \frac{0.9761\times10^{-3}}{2\times 1.35 \times 50.05 \times 0.95} = 7.603mm$$

And the rotor back iron R_{ebi}

$$R_{ebi} = \frac{0.9761\times10^{-3}}{2\times 1.35 \times 50.05 \times 0.95} = 7.603mm$$

7.3.2.2 Width of the teeth

Unlike the stator and rotor back-irons, the stator teeth width is determined from the maximum flux achieved when the centre of the rotor pole is aligned with the centre of

the stator teeth. Therefore, a concentration factor i.e. k_{ds} is considered to compensate for the difference between the one-pole pitch τ_p and stator teeth pitch τ_{TW}. The concentration factor k_{ds} is calculated as shown in Equation (5.7)

$$k_{ds} = \frac{\tau_p}{\tau_{TW}} = \frac{\pi.\frac{D}{Nm}}{\pi.\frac{D}{Nm} - Bs0}$$

$$= \frac{\pi.\frac{82.44}{9}}{\pi.\frac{82.44}{9} - 2} = 1.1614$$

Accordingly, the stator teeth width can be determined as Equation 5.6

$$T_w = \frac{\Phi_{(1)} \times k_{ds}}{B_{knee} \text{ L } k_s} = \frac{0.9761 \times 10^{-3} \times 1.1614}{1.35 \times 50.05 \times 0.95} = 17.66mm$$

7.3.3 Back EMF calculation

The winding factor k_w for non-overlapping concentrated winding with nine slots and eight poles was calculated as 0.945. At no-load condition, the induced RMS voltage is the function of number of turns-per-phase N_{ph}. At this stage of optimisation, the number of turn is unknown; how to determine the number of turns in series per phase will be explained later. However, the induced voltage in the stator winding is calculated per Equation (5.9)

$$EMF_{(1)} = \frac{2\pi f}{\sqrt{2}} \left(k_w . N_{ph}\right) \text{B}_{(1)} \times \frac{2}{\pi} \times \frac{\pi DL}{Np}$$

$$EMF = \frac{2\pi \times 42.66}{\sqrt{2}} \left(0.945. N_{ph}\right) \times 0.9463 \times \frac{2}{\pi} \times \frac{\pi \times 82.44 \times 50.05}{8}$$

Therefore, the induced EMF in terms of number of turns-per-phase is

$$= 0.1748\, N_{ph}\ [V]$$

7.3.4 Inductance calculation

The total inductance L_s is the sum of the airgap inductance L_{sg} and slot leakage inductance L_{sl} and the end-winding inductance L_{ew} as shown in Equation 5.11

$$L_s = L_{sg} + L_{sl} + L_{ew}$$

All the inductance parameters required the value of number of turns-per-phase N_{ph} and machine dimensions that are still unknown. However, in terms of N_{ph}, the synchronous inductance can be computed as (5.12):

$$L_{sg} = \frac{3}{\pi}\left(\frac{k_w\, N_{ph}}{p}\right)^2 \frac{\mu_0}{g_{eq}}\, DL$$

$$\frac{3}{\pi}\left(\frac{0.945\times N_{ph}}{4}\right)^2 \frac{4\pi\times10^{-7}}{5.89} \times 82.44\times50.05 = 5.638\times10^{-8} \times(N_{ph})^2\ H$$

The slot leakage inductance L_{sl} is computed as (5.13)

$$L_{sl} = \frac{2\,\mu_0\, L\,\left(N_{ph}\right)^2}{p.q}\,\lambda_{sl}$$

The coefficient λ_{sl} i.e. slot leakage permeance coefficient depends on the slot shape. Figure 7.1 shows all the dimensions associated with the rectangular slot shape used in the optimised motor. Therefore, for a rectangular slot, λ_{sl} can be computed as Equation (5.14)

$$\lambda_{sl} = \left(\frac{2}{3}.\frac{H_{s2}}{B_{s1}+B_{s2}} + \frac{2H_{s1}}{B_{s0}+B_{s1}} + \frac{H_{s0}}{B_{s0}}\right)\frac{1+3\beta}{4}$$

A typical value of the slot opening height H_{s0} was selected as 1.5mm. The heights of the slot tang H_{s1} can be calculated from the tooth tang angle α and the difference between tooth pitch τ_{TW} and tooth width T_w. For small electric machines, the tooth tang angle ranges between 30° to 35° [10]. In the optimised design, the angle selected was 30° to reduce the slot height.

$$H_{s1} = \frac{1}{2}\times(\tau_{TW} - T_W)\times \tan(\alpha)$$

$$H_{s1} = \frac{1}{2}\times(26.77 - 17.66)\times \tan(30) = 2.63mm$$

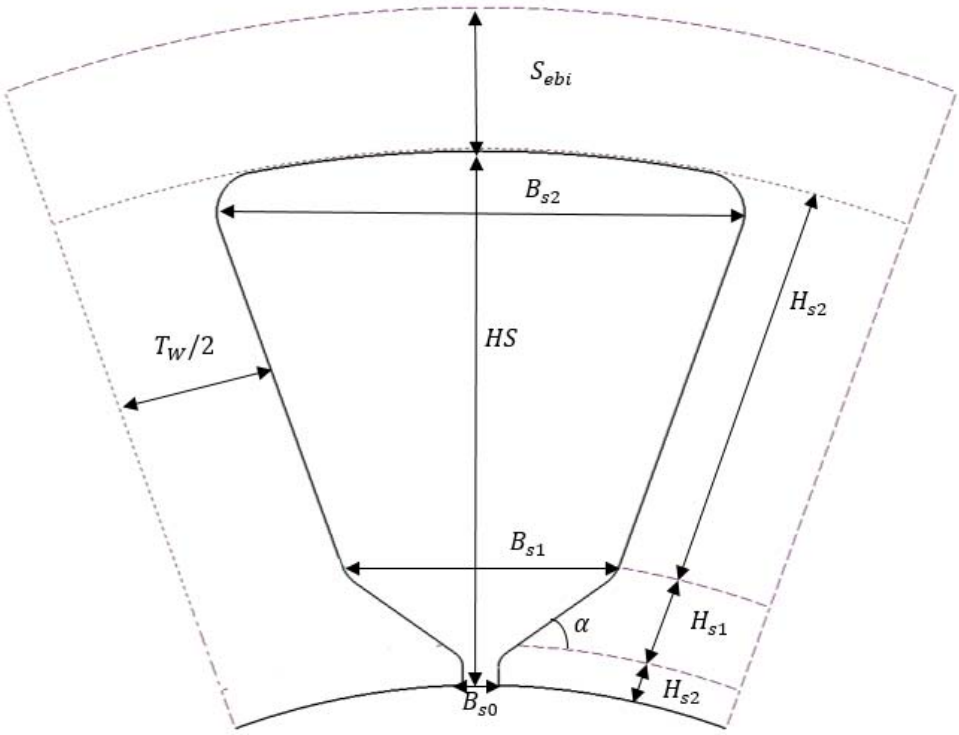

Figure 7.1 Dimensions of the rectangular slot shape

At this stage, the value of H_{s2} and B_{s2} are still unknown and can be assumed equal to the double of T_w and B_{s1} respectively without affecting the inductance values. The coefficient β is the ratio of the coil-pitch over one pole-pitch Nm/p.

$$\lambda_{sl} = \left(\frac{2}{3}.\frac{35}{14.23+28.5} + \frac{2\times2.63}{2+14.23} + \frac{1.5}{2}\right)\frac{1+3\times1.125}{4} = 1.18$$

Therefore, with q equal to 0.375

$$q = Nm/Np/3 = 9/8/3 = 0.375$$

The slot leakage inductance in terms of N_{ph} is equal to

$$L_{sl} = \frac{2\times4\pi\times10^{-7}\times50.05\times10^{-3}\times\left(N_{ph}\right)^2}{8\times0.375}\times1.18\,H$$

The end-winding inductance can be computed as Equation (5.15)

$$L_{ew} = \frac{\mu_0\,\tau_c\,N_{ph}^2}{16}\ln\left(\frac{\pi\ {\tau_c}^2}{4\ H_s B_{sm}}\right)$$

With one slot pitch, the coil pitch τ_c can be calculated as

$$\tau_c = \frac{(D+H_{s2})\times\pi}{Nm} = \frac{(82.44+35)\pi}{9} = 40.99mm$$

The slot mean width B_{sm} is also calculated as

$$B_{sm} = \frac{B_{s1+}B_{s2}}{2} = \frac{14.23+2*14.23}{2} = 21.35mm$$

The total slot height H_s is the sum of the assumed value of H_{s0} H_{s1} and H_{s2}

$$L_{ew} = \frac{4\pi\times10^{-7}\times40.99\times N_{ph}^2}{16}\ln\left(\frac{\pi\times40.99^2}{4\times39\times21.35}\right)\ H$$

7.3.5 Calculation the number of turn and current

In Chapter 4, it has been shown how the phasor diagram for the synchronous machine is constructed and ruled by Equation (5.8)

$$\overline{V_t} = \overline{EMF} + \left(R_{ph} + jX_s\right).\overline{I_{ph}}$$

Since the terminal voltage V_t is known and all the inductances and EMF values are described in terms of number of turns-per-phase N_{ph}, the phasor diagram can be solved to match with this relation. Compared to synchronous reactance, the value of phase resistance R_{ph} is very small; thus, it can be omitted in this relation. Thus, all the values in the phasor diagram relation can be put on one side of the equation and N_{ph} on the other side. In this machine design, N_{ph} was solved as 591 turns and the values of the back-EMF and inductances were calculated accordingly.

The generated back-EMF

$$EMF = 0.1748 \times 591 = 103.28\ V$$

Synchronous inductance

$$L_{sg} = 4.638 \times 10^{-8} \times (591)^2 = 0.0162\ H$$

Slot-leakage inductance

$$L_{sl} = 0.0427\ H$$

End-winding inductance

$$L_{ew} = 0.0021\ H$$

Total inductance is

$$L_s = L_{sg} + L_{sl} + L_{ew}$$

$$L_s = 0.0162 + 0.0427 + 0.0021 = 61mH$$

Finally, the RMS phase current I_{ph} is calculated as

$$I_{ph} = \frac{P_{out}}{3.EMF_{(1)}} = \frac{1750}{3 \times 103.28} = 5.648A$$

7.3.6 Slot height calculation

According to Equation (5.16), the calculation for conductor cross-sectional area A_{wire} requires the value of current density J which was generated from optimisation and the RMS phase current I_{ph}.

$$A_{wire} = \frac{I_{ph}}{J} = \frac{5.648}{7.12} = 0.8225\ mm^2$$

The conductor diameter D_w can be calculated as in Equation (5.17)

$$D_w = \sqrt{\frac{4 \times A_{wire}}{\pi}} = 1.005mm$$

The closest standard AWG wire is 18 with a diameter of 1.0233mm and correspondent cross-section area A_{wire} is 0.8225mm^2. For a slot with double layer, the total copper cross section area is computed as

$$A_{Cu} = \frac{A_{wire}\ .N_{ph}}{q.p} = \frac{0.8225 \times 591}{0.375 \times 4} = 324.06\ mm^2$$

Therefore, with slot fill factor K_{fill} of 0.5, the total slot area that is needed to fit winding conductors is

$$A_{slot} = \frac{A_{Cu}}{K_{fill}} = 648.12\ mm^2$$

The geometrical area of one slot is calculated as

$$A_{slot} = \left(H_{s2} \times \frac{B_{s1} + B_{s2}}{2}\right) + \left(H_{s1} \times \frac{B_{s0} + B_{s1}}{2}\right) + (B_{s0} \times H_{s0})$$

The values of $B_{s0}, B_{s1}, H_{s0}\ H_{s1}$ are already known. Assuming the slot with parallel teeth side, the values B_{s2} can be calculated as

$$B_{s2} = \frac{\pi\left(D + 2 \times (H_{s0} + H_{s1} + H_{s2})\right)}{N_m} - T_w$$

Then, if the value of B_{s2} and total area found from the slot factor (648.12mm^2) compensated into the formula for the geometrical area of one slot, the value of H_{s2} would be determined. However, using the above procedure, the values of B_{s2} and H_{s2} were 32.82mm and 26.96mm respectively.

Then, the stator outer diameter OD can be calculated as

$$OD = D + 2 \times (H_{s0} + H_{s1} + H_{s2} + S_{ebi})$$

$$OD = 82.44 + 2 \times (1.5 + 2.63 + 26.96 + 7.6) = 159.845mm$$

7.3.7 Machine weight and volume

The total weight of the machine refers to machine active materials consisting of stator core, rotor core, stator windings and magnet only. The other components, such as

frame, shaft and insulation material, are not included in the calculations of weight and power density.

Table 7.3 Mass density of active materials in the optimised machine

Active material	**Mass density [kg/m^3]**
M330-35A	7800
NdFeB 230/220h	7425
Copper	8954

Table 7.3 shows the mass density of active materials used in the machine parts. The weight of the stator is composed of back-iron weight $Wt_{S_{ebi}}$ and teeth weight Wt_{Tw} calculated as follows:

$$W_{S_{ebi}} = \frac{\pi}{4} x(OD^2 - (OD - 2{\times}S_{ebi})^2){\times}L{\times}M_{Steel}$$

$$W_{S_{ebi}} = \frac{\pi}{4} x(159.845^2 - (159.845 - 2{\times}7.6)^2){\times}50.05{\times}7800{\times}1e-9$$

$$W_{S_{ebi}} = 1.42\text{kg}$$

The stator teeth have the same material as the back iron, the total weight of the teeth can be computed as

$$W_{Tw} = \left(Hs0{\times}\left(\frac{\pi D}{Nm} - Bs0\right) + Hs1{\times}\left(\frac{\pi D}{Nm} - Bs0 - Tw\right) + Hs2{\times}Tw\right){\times}Nm{\times}L {\times}M_{Steel}$$

$$W_{Tw} = \left(1.5{\times}\left(\frac{\pi{\times}82.44}{9} - 2\right) + 2.5{\times}\left(\frac{\pi{\times}82.44}{9} - 2 - 17.66\right) + 24.98{\times}17.66\right){\times}9 {\times}50.05{\times}7928{\times}1e-9 = 1.899\text{kg}$$

The weight of the rotor back-iron also has the same lamination material, calculated as

$$W_{R_{ebi}} = \frac{\pi}{4} x(D_r^2 - (D_r^2 - 2\times \mathrm{R}_{ebi})^2)\times L\times M_{Steel}$$

Where D_r is the rotor core outer diameter calculated as

$$\mathrm{D}_r = D - 2\times(h_m + g)$$

Equal to

$$\mathrm{D}_r = 82.44 - 2\times(5.935 + 0.5) = 69.57mm$$

And the rotor core weight is

$$W_{R_{ebi}} = \frac{\pi}{4} x(69.57^2 - (69.57^2 - 2\times 7.6)^2)\times 50.05\times 7928\times 1e-9 = 0.5780\mathrm{kg}$$

For the bread-loaf magnet shape, the area of permanent magnet A_m is calculated as the sum of the blue rectangular A_{m1} and the red top chord A_{m2} as shown in Figure 7.2

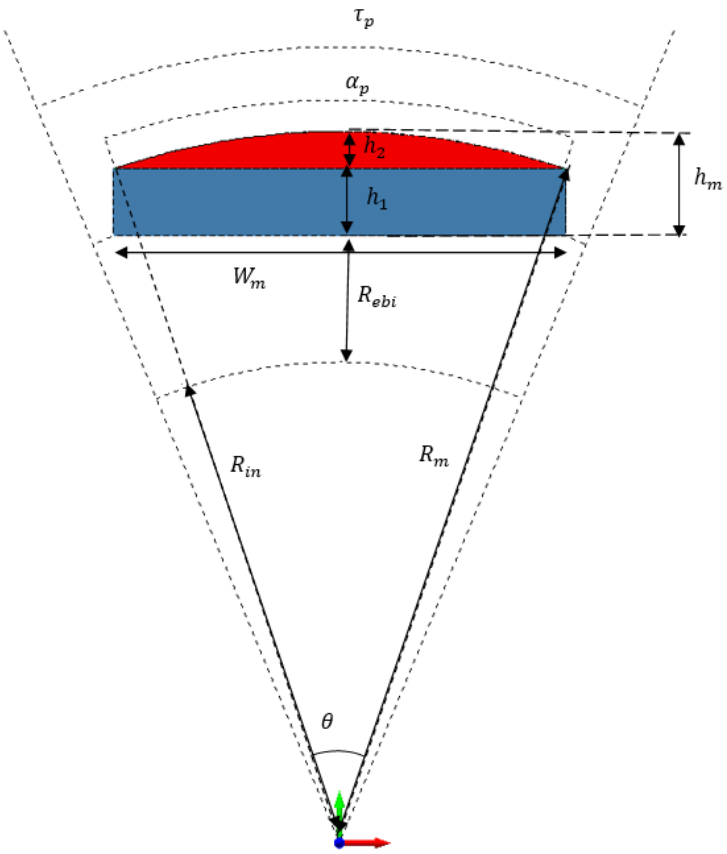

Figure 7.2 Dimensions of one-pole segment of the optimised motor

The area of the blue rectangular shape $Am1$ can be calculated from the magnet base width Wm and the magnet-side height $h1$

$$Am1 = Wm \times h1$$

$$Wm = 2 \times R_m \times \sin\left(\frac{\theta}{2}\right)$$

Where R_m is the magnet outer radius and θ is the magnet pitch in degree

$$R_m = \frac{D}{2} - g = 40.72mm$$

$$\theta = \frac{360}{N_p} \times \alpha_p = \frac{360}{8} \times 0.83 = 37.35°$$

$$Wm = 2 \times 40.72 \times \sin\left(\frac{37.35}{2}\right) = 26.07mm$$

$$h1 = R_m - \sqrt{(R_m)^2 - \left(\frac{W_m}{2}\right)^2} = 2.14mm$$

$$A_{m1} = 26.81 \times 3.66 = 98.86\ mm^2$$

The red chord area A_{m2} can be calculated as

$$A_{m2} = \frac{1}{2}\ (R_m)^2 \times (\theta - \sin\theta)$$

$$A_{m2} = \frac{1}{2} \times (40.72)^2 \times (0.6709 - 0.6217) = 73.47\ mm^2$$

Then, the total area of one magnet pole A_m is

$$A_m = A_{m1} + A_{m2} = 98.27 + 40.80 = 139.07mm^2$$

And the permanent magnet weight is

$$W_{mag} = N_p \times A_m \times L \times M_{PM}$$

$$W_{mag} = 8 \times 139.08 \times 50.05 \times 7425 \times 10^{-9} = 0.405\ kg$$

The total weight of copper W_{Cu} can be estimated as

$$W_{Cu} = 3 \times l_{turn} \times A_{wire} \times N_{ph} \times M_{Cu}$$

l_{turn} is the length of one turn estimated as

$$l_{turn} = 2(L + l_{end})$$

l_{end} is the length of one end-winding connection that can be estimated as

$$l_{end} = \frac{\pi(D + H_S)}{Nm}$$

$$l_{end} = \frac{\pi(82.44 + 31.01)}{9} = 39.63mm$$

And one turn length is equal to

$$l_{turn} = 2 \times (50.05 + 39.63) = 179.36mm$$

The total weight of copper W_{Cu} is

$$W_{Cu} = 3 \times 179.36 \times 0.8225 \times 591 \times 8954 \times 10^{-9} = 2.342kg$$

Finally, the total active weight W_{total} of the machine is

$$W_{total} = W_{S_{ebi}} + W_{Tw} + W_{R_{ebi}} + W_{PM} + W_{Cu}$$

$$W_{total} = 1.42 + 1.899 + 0.578 + 0.405 + 2.342 = 6.64kg$$

The machine volume consists of the calculation of the volume of a simple cylindrical where the diameter is the outer diameter of the stator and length over the axial length.

$$Voulme = \pi\left(\frac{OD}{2}\right)^2 \times (L)$$

$$Voulme = \pi\left(\frac{159.84}{2}\right)^2 \times 50.05 = 1.00\ Litre$$

7.3.8 Losses and efficiency calculation

7.3.8.1 Copper loss

The copper resistivity ρ_{cu} at 20°C is $1.68\times10^{-8}\ \Omega.m$. The phase resistance R_{ph} is calculated as

$$R_{ph} = \rho_{cu}\times N_{ph}\times\frac{l_{turn}}{A_{wire}}$$

$$R_{ph} = 1.68\times10^{-8}\times591\times\frac{179.36}{0.8225} = 2.165\ \Omega$$

The copper loss P_{cu} is computed as

$$P_{cu} = 3R_{ph}\left(I_{ph}\right)^2$$

$$P_{cu} = 3\times2.165\times5.64^2 = 207.24W$$

7.3.8.2 Iron Loss

Total core loss P_{core} of the electric machine is the sum of hysteresis loss P_{hys}, eddy-current loss P_{edd} and anomalous loss (the term “excess loss” is often used also).

$$P_{core} = P_{edd} + P_{hys}$$

As the electric frequency in the optimised machine is small, 42.7Hz, the core loss is also expected to have small value. The total core loss is characterised by the Steinmetz Equation with separate terms for hysteresis and eddy-current losses:

for hysteresis loss, as

$$P_{hys} = k_h \, f^{\propto} \, B_{max}^{\mathcal{B}} \quad W/kg$$

And for eddy current loss as

$$P_{edd} = k_e \, (f.B_{max})^2 \quad W/kg$$

Where k_h, k_e , $\propto$ and $\mathcal{B}$ are material parameters generally found by curve fitting. The "anomalous loss" is associated with domain wall movement and is not often accounted for in empirical expressions of the iron loss. In the Steinmetz Equation, the coefficient k_e is used to compensate for this anomalous loss.

The values of the Steinmetz coefficients in the above equations are given in the material properties data sheet available in "MagNet software" as follows

$k_h = 0.0075437$

$k_e = 3.11146 \, e^{-5}$

$\propto = 1.29522$

$\mathcal{B} = 1.79624$

Therefore, with estimated maximum magnetic flux density in the stator and rotor lamination core, the hysteresis loss is estimated as

$$P_{hys} = 0.0075437 \times 42.6^{1.29522} \times 1.6^{1.79624} = 2.266 \text{ W/kg}$$

And the eddy current loss

$$P_{edd} = 3.11146\, e^{-5} \times (42.6 \times 1.6)^2 \;\; = 0.1449\, W/kg$$

The places of the core loss are in the stator teeth and stator back-iron; therefore, the total core loss of the machine is

$$P_{core} = (P_{edd} + P_{hys}) \times (Wt_{S_{ebi}} + Wt_{Tw})$$

$$P_{core} = (0.1449 + 2.266) \times (1.42 + 1.898) = 8.00W$$

7.3.9 Efficiency

The machine efficiency is calculated from the output power and losses as

$$\eta = \frac{P_{out}}{P_{out} + P_{cu} + P_{core} + P_{wind} + P_{fric}}$$

For small machines, the friction and windage losses are small, particularly as most stators are potted with epoxy resin, thus windage loss is significantly eliminated; friction loss is proportional to speed. Therefore, in small machines with comparatively low speed friction and windage, losses are completely omitted. Thus, the formula for machine efficiency will account for core and copper losses only as follows

$$\eta = \frac{P_{out}}{P_{out} + P_{cu} + P_{core}}$$

$$\eta = \frac{1750}{1750 + \ 207.244 + 8.08} = 89.04\%$$

7.3.10 Armature reaction field

A relatively simple method to evaluate the effect of armature reaction field for a three-phase PMSM is presented here. The flux density due to the armature reaction can be determined as

$$B_{arm} = \frac{\mu_0 \, \mu_r \, MMF_{arm}}{g'}$$

For a common stator of nine slots and three-phase shifted 120° and nine coils connected to complete the winding, the magnetomotive force due to armature winding can be calculated as

$$MMF_{arm} = \frac{3\sqrt{2}}{\pi} \frac{k_w \, N_{ph} \, I_{ph}}{p}$$

$$MMF_{arm} = \frac{3\sqrt{2}}{\pi} \frac{0.945\times 591\times 5.64}{4} = 1065 \, A.Turn$$

Finally, the flux density due to armature reaction is calculated as

$$B_{arm} = \frac{4\pi\times10^{-7}\times1.1\times1065}{5.89\times10^{-3}} = 0.249 \, T$$

The extra flux density due to armature reaction will be added to the flux at knee point B_{knee} of the steel to limit the maximum flux density B_{MAX} in the stator and rotor lamination. B_{MAX} is a constraint value that must not be violated through the

optimisation search. Thus, with a value of 1.35T for the B_{knee}, the value of B_{Max} for this design is 1.599T, which is less than the assigned constraint point 1.6T.

7.3.11 Demagnetisation current

At rated operating conditions, the magnet should be safe from the risk of demagnetisation. Neglecting current harmonic effects, the demagnetisation current is estimated as Equation (5.51) [66]

$$I_{demag} = \frac{Np\,\pi}{6\,\mu_0\mu_r\left(k_w\,N_{ph}\right)}\times\left(B_r h_m - B_k(g + h_m)\right)$$

The knee point B_k of the permanent magnet at the operating temperature can be determined directly from the demagnetisation curve of magnet material as shown in Figure 7.3.

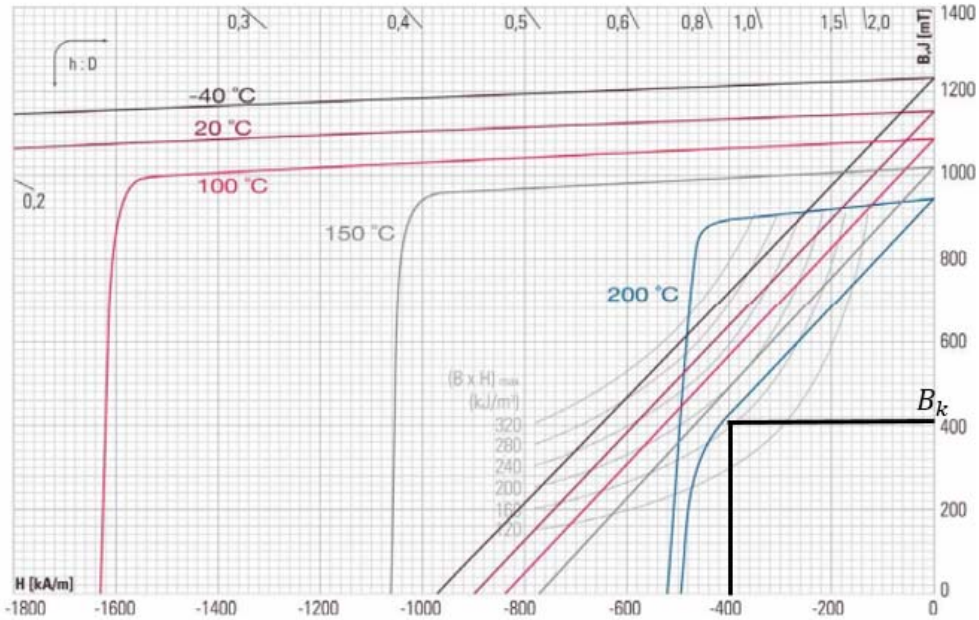

Figure 7.3 Demagnetisation characteristics of NdFeB 230/220h grade showing the knee point at 200°C.

As shown in the graph, the magnet has potential demagnetisation risk at temperature 200°C and B_k of 0.4T. However, at the operating temperature 150°C, the corresponding value of B_k was in the third quadrant of the demagnetisation curve, lower than 0T. Therefore, as the supplier provides demagnetisation curve for the second quadrant only, the value for B_k is assumed 0T. Under this assumption, the demagnetisation current I_{demag} at the operating temperature can be estimated as

$$I_{demag} = \frac{8\pi}{6\times 4\pi\times 10^{-7}\times(0.945\times 591)}\times\left(1.0486\times 5.93 - 0\times(0.5 + 5.935)\right)$$
$$= 37.114A$$

As the demagnetisation current I_{demag} is almost seven times higher than the rated phase current I_{ph}, there is no risk of demagnetisation at normal operating conditions. However, if the operating temperature has changed, it is the designer's responsibility to check for the new demagnetisation current.

Furthermore, in the analytical model, the risk of demagnetisation was considered at fault condition that may occur in the inverter e.g. faulty diode. At fault condition, the current is only limited by the winding phase resistance R_{ph} and leakage reactance i.e. locked-rotor current I_{LR}. In this case, the winding current will be significantly increased and, consequently, the high armature field will suppress the field generated from the permanent magnet B_m. Thus, to avoid the risk of demagnetisation, the permanent magnet should be thick enough to withstand the armature reaction field at locked-rotor condition.

The locked-rotor current I_{LR} is calculated as Equation (5.53)

$$I_{LR} = \frac{V_t}{R_{ph} + jX_{LKG}}$$

jX_{LKG} is the leakage reactance and calculated as

$$X_{LKG} = 2\times\pi\times f\times(L_{sl} + L_{ew})$$

$$X_{LKG} = 2\times\pi\times 42.66\times(0.0422 + 0.002) = 11.85\ \Omega$$

$$I_{LR} = \frac{151}{2.157 + j11.85} = 12.53\ A$$

The value of I_{LR} is lower than demagnetisation current I_{demag}. This shows a good potential of there being no total risk of demagnetisation. However, the possibility of partial demagnetisation still exists. Therefore, to ensure there is no demagnetisation risk at all at this fault condition, the magnetomotive force at locked-rotor condition $MMF_{arm(LR)}$ should be calculated and must be lower than the magnetomotive force produced from the permanent magnet as shown in Equation (5.52), so that

$$MMF_{arm(LR)} < \frac{(h_m + g)}{\mu_0\mu_r}\times(B_m - B_k)$$

Per to Equation (5.48), the $MMF_{arm(LR)}$ can be calculated as

$$MMF_{arm(LR)} = \frac{3\sqrt{2}}{\pi}\frac{k_w\ N_{ph}\ I_{LR}}{p}$$

$$MMF_{arm(LR)} = \frac{3\sqrt{2}}{\pi}\frac{0.945\times 591\times 12.53}{4} = 2362\ A.turn$$

The magnetomotive force of the permanent magnet is

$$\frac{(h_m + g)}{\mu_0\mu_r}\times(B_m - B_k)$$

$$\frac{(5.935 + 0.5)\times 1e-3}{4\pi\times 10e-7\times 1.1} \times (1.0486 - 0.4) = 3019.7\ A.turn$$

Therefore, as the magnetomotive force produced from the permanent magnet is higher than that from the armature reaction, the magnet will be safe from any partial demagnetisation at fault condition.

7.3.12 Temperature rise

The thermal model is designed to ensure the suitability of the machine design in terms of keeping the temperature of components within certain limits at rated operation conditions. The thermal model and thermal network, as detailed in the previous chapter, have been used to estimate the temperature in the machine components, particularly, magnet and winding. To avoid the temperature rising above specific limits, the maximum temperatures have been constrained within the model. With ambient temperature of 40°C, the maximum estimated temperature in the magnet T_{PM} was 128°C and in the winding T_{Cu} 135°C and 140°C in the end-winding T_{EW}.

7.3.13 Penalties and Objective function

The main rule of the objective function is to evaluate the overall design and assign its fitness, so it can be compared with other results from other designs. In its context, the objective function has the main performance index that reflects the design priorities. In this optimisation, the main objective was to enhance the machine power density, in terms of weight, volume, and efficiency. Therefore, the objective function was written to reflect this target as follows:

$$Output = W_{total} + W_{mag}\times 20 + 10\times Voulme + (100 - \eta) + penalties$$

Based on the analytical calculation, the output of the objective function is

$$Output = 6.64 + (0.405 \times 20) + (1.00 \times 10) + (100 - 89.04) + penalties$$

The values of penalties have been added to the objective function to alert to any violation in the optimisation constraints. In the case of one constraint having been violated, the output of the objective function will be increased by "1000". Hence, any design with one constraint violation will be excluded.

The optimisation has many constraints to limit the maximum value of some parameters, including $T_{Mag} \leq 140°C$, $T_{Cu} \leq 140°C$, $W_{Mag} \leq 0.53\ kg$ and $B_{max} \leq 1.6$.

The results from the analytical model show that the average temperature in the magnet T_{Mag} was calculated as 128°C and in the winding coil-side T_{Cu} was 135°C, with maximum temperature rise in the end-winding T_{EW} as 140°C. The weight of the permanent magnet material was calculated as 0.4051kg and the maximum flux density in the stator core was 1.599T. Therefore, upon these results, as none of the constraints have been violated, the total penalties will be 0 and the output of the objective function will be the sum of the performance indices only. Thus, the objective function is

$$Output = 6.64 + (0.405 \times 20) + (1.00 \times 10) + (100 - 89.04) + 0 = 35.73$$

7.4 Validation of analytical approach based on Finite Element Analysis

Having achieved the optimal geometrical dimensions, electromagnetic and thermal parameters through analytical design, it is often useful to verify the optimisation results with more highly accurate simulation e.g. Finite Element Analysis FEA. FEA

is a numerical technique based on partial differential equations of a continuum domain that is discretised into a finite number of parts known as elements. Hence, FEA has good accuracy and higher reliability. FEA has been applied to analyse electric machines to improve performance and efficiency.

Therefore, to validate electromagnetic parameters generated from optimisation, it is important to accurately build a machine model with the same dimensions and input parameters. Many software packages are available on the market to simulate electric machine design, such as “MotorSolve” and “MagNet” provided from “Infolytica”. The simulation through this software can be performed through 2D or 3D analysis, particularly for electric machines, as the axial dimension through z-axis is uniform, apart from end-winding; thus, FEA-2D analysis is relevant to simulate the model. In another case, for example, where skewing is applied or rotor overhangs stator length, it is necessary to use 3D analysis to validate results. For the purpose of the optimised machine, MotorSolve has been used to build the optimised model and MagNet used to perform the simulation. Both software packages are provided by Infolytica.

Figure 7.4 shows the final model as built on “MotorSolve”. The geometrical dimensions, as obtained from the optimisation, have been entered to build the final structural design of the machine. Electric current, available voltage and speed can also be specified for the design. In addition, the material can be selected from the library or material property entered to create a new material.

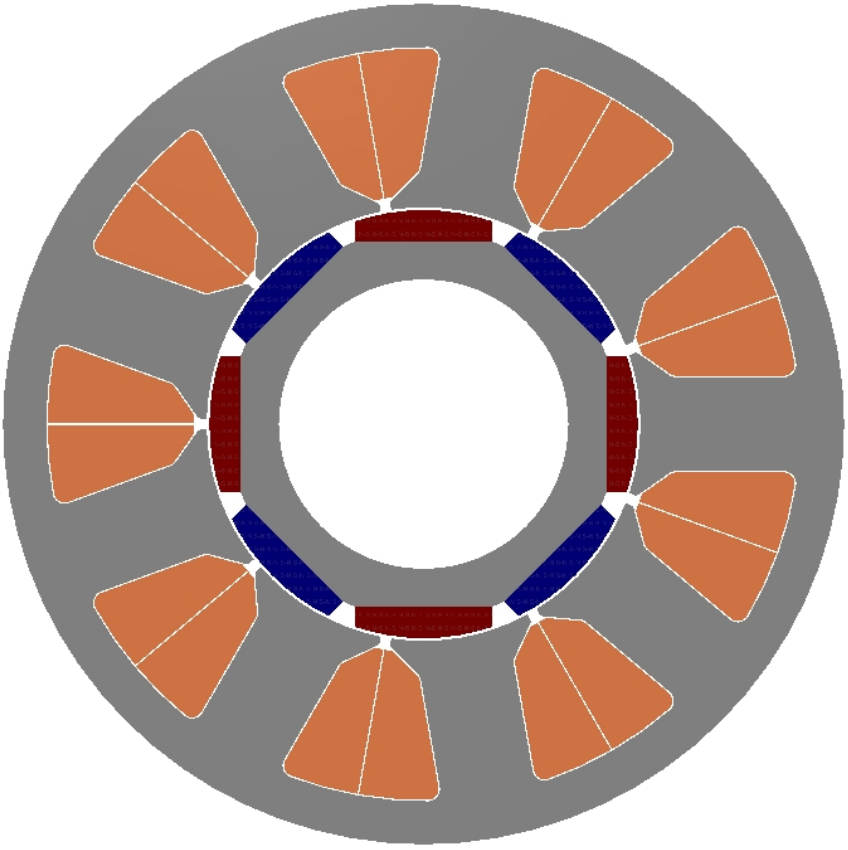

Figure 7.4 Structural design of the optimised electric machine model

7.4.1 FEA simulation

Compared with FEA analysis, the analytical model based on several simplifications and hypotheses is still limited in accurately evaluating the electromagnetic parameters in electric machines. Therefore, in order to facilitate the analysis of an electric machine, many numerical solutions based on the finite element method FEM were developed. Generally speaking, with precise dimensions and appropriate component meshing size, FEM is currently the most accurate method to validate electromagnetic design through 2D/3D simulations.

Having created the structural model of the machine with the generated optimal dimensions from BA, appropriate material properties and winding configurations, an

FEA simulation can be run at specific operation temperature to solve the electromagnetic parameters for different operating conditions.

7.4.2 Airgap flux density

The magnetic flux density in the airgap is the first magnetic parameter to be calculated in the analytical design. Based on its value, the other machine electromagnetic parameters and geometrical dimensions were calculated. Hence, any divergence in the airgap flux density can lead to under- or over-estimation on other parameters. Based on FEA analysis, the waveform of the airgap flux density was generated as shown in Figure 7.5.

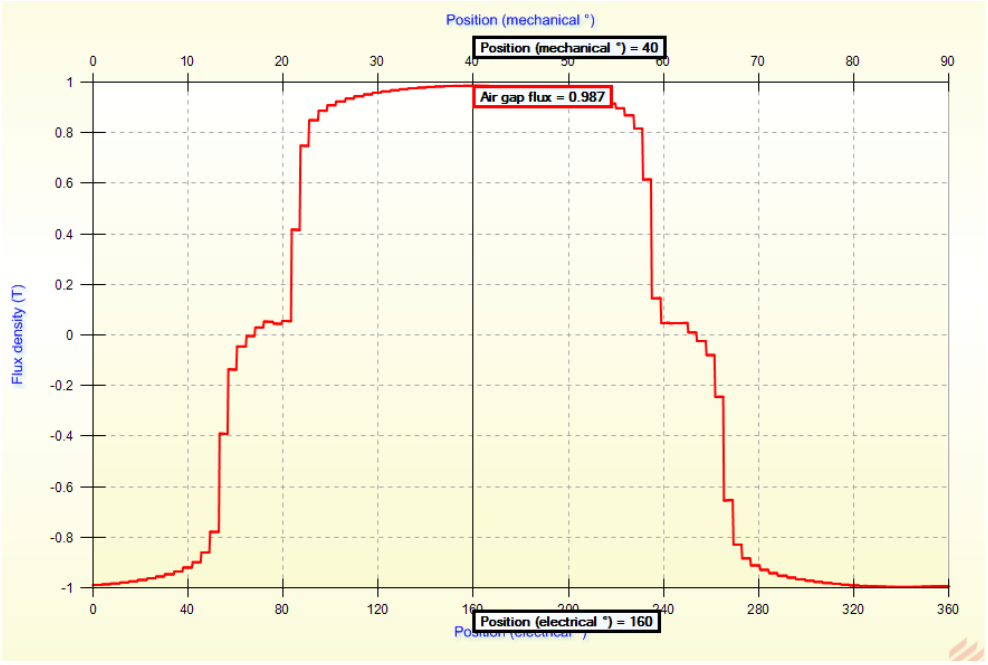

Figure 7.5 Waveform of Airgap flux density as generated from FEA simulation

As shown in Figure 7.5, the slot-effect has no major contribution to the waveform shape. This is due to the small ratio between the selected number of slots and poles

1.125. Therefore, the first fundamental airgap flux density is equal to 0.987T, as shown in the harmonics content amplitude in Figure 7.5.

7.4.3 Inductance

Using 2D analysis of the electric machine model, the FEA analysis can generate the value of total inductance as a function of the current without giving particular information of the types of these inductances, whether it is airgap inductance or slot inductance. However, the end-winding inductance is calculated separately. The value of maximum self-inductance, including airgap inductance and slot inductance, as shown in Figure 7.6, was read off as 65.5mH and the end-winding inductance was 1.84mH, as shown in end-winding parameters in Table 7.4.

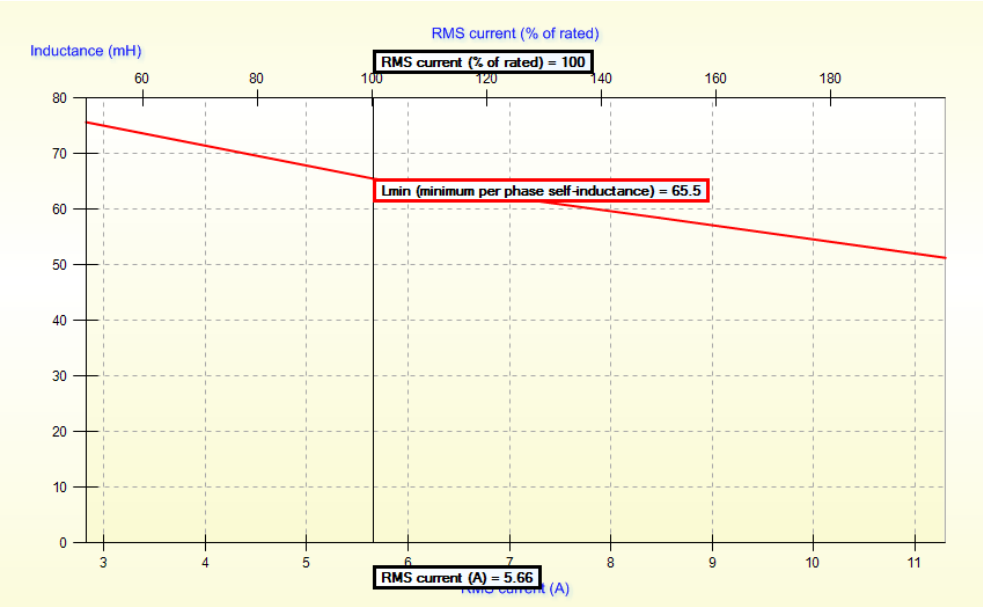

Figure 7.6 Total self-inductance as generated from FEA

Table 7.4 End-winding parameters of the optimised design

Stator End Windings		
Outer diameter	141	mm
Height	10	mm
Fill factor	85.2	%
Resistance	0.977	Ω
Inductance	1.84	mH

7.4.4 Back-EMF

In Chapter 5, the bread-loaf magnet shape, with varying thickness in the direction of magnetisation, was selected to enhance the generated voltage to have a shape close to the ideal sinusoidal waveform. Figure 7.7 shows the normalised back-EMF generated from the optimised machine, along with the ideal sinusoidal waveform. The graph shows that the generated voltage was very close to the ideal waveform with a deviation of 0.03 degrees. Therefore, the sinusoidal voltage and current will enhance the machine power density and reduce the torque ripple in the generated torque.

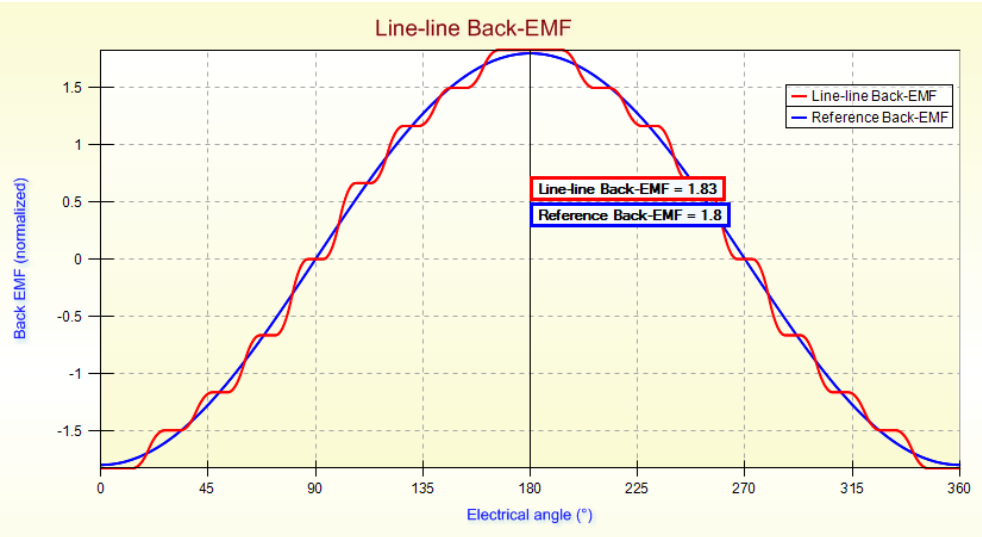

Figure 7.7 Normalised line-line back-EMF compared with ideal sinusoidal waveform

At no-load condition, the peak line-line $V_{peak\ (L-L)}$ amplitude of back-EMF waveform generated from FEA, as shown in Figure 7.8, was 260.2V.

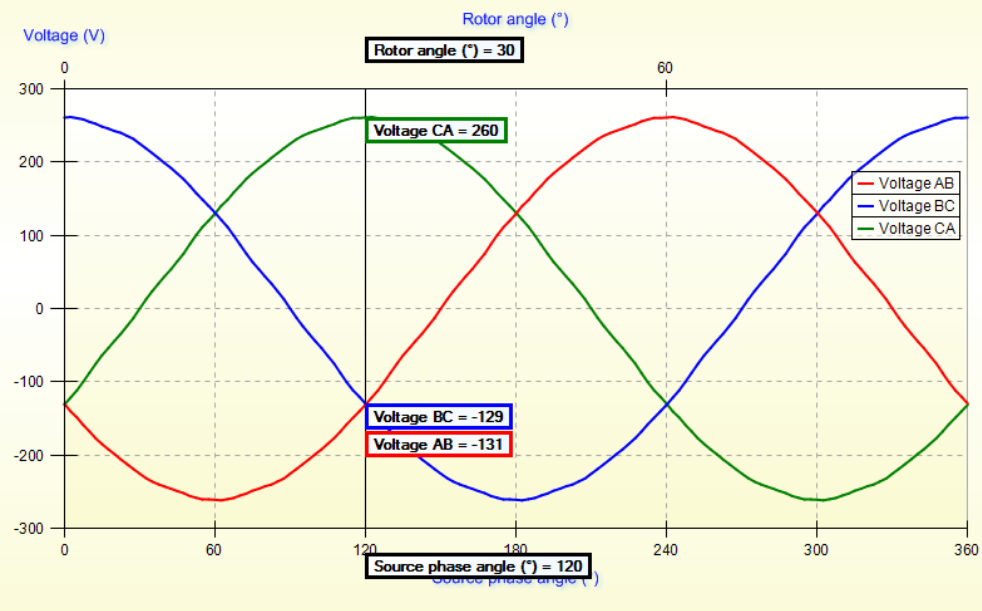

Figure 7.8 Waveform of generated back-EMF from FEA

The generated voltage waveform is almost sinusoidal; therefore, the fundamental RMS value can be calculated directly as

$$E_{rms} = \frac{V_{peak\ (L-L)}}{\sqrt{2}\sqrt{3}} = \frac{260.2}{2.449} = 106.23V$$

7.4.5 Torque

Assuming the ideal sinusoidal current, at rated operation condition the FEA simulation for the generated electromagnetic torque is shown in Figure 7.9. With maximum value T_{max} of 28.0Nm and minimum value T_{min} of 26.5, the average torque value T_{avg} is calculated as 27.25 N.m.

Figure 7.9 Waveform of Electromagnetic torque as generated from FEA

In Chapter 5, the magnet coverage ratio α_p was selected to produce minimum MMF harmonic to minimise the torque distortion caused by the ripple and cogging torque. The torque ripple can be calculated from the maximum and minimum torque, as shown in Figure 7.9. Therefore, the percentage of torque ripple is equal to 5.5%.

$$T_{ripple} = \frac{T_{max} - T_{min}}{T_{avg}} = \frac{28.0 - 26.5}{27.25} = 5.5\%$$

The cogging torque was also analysed at zero current, as shown in Figure 7.10. The maximum cogging torque was 0.148 Nm. Compared with the benchmark design (0.4Nm), the cogging torque was significantly reduced.

Figure 7.10 Cogging torque of the optimised motor at zero current

The torque/speed curve of the optimised machine has been simulated over a range of speed increment 50rpm, as shown in Figure 7.11. The simulation shows that source voltage has the capability to keep the stall torque constant up to base speed. However, at base speed 640, the generated torque was 0.9Nm higher than the required torque. At this speed, if the motor is thermally safe, any extra torque will enhance the machine performance for quick acceleration.

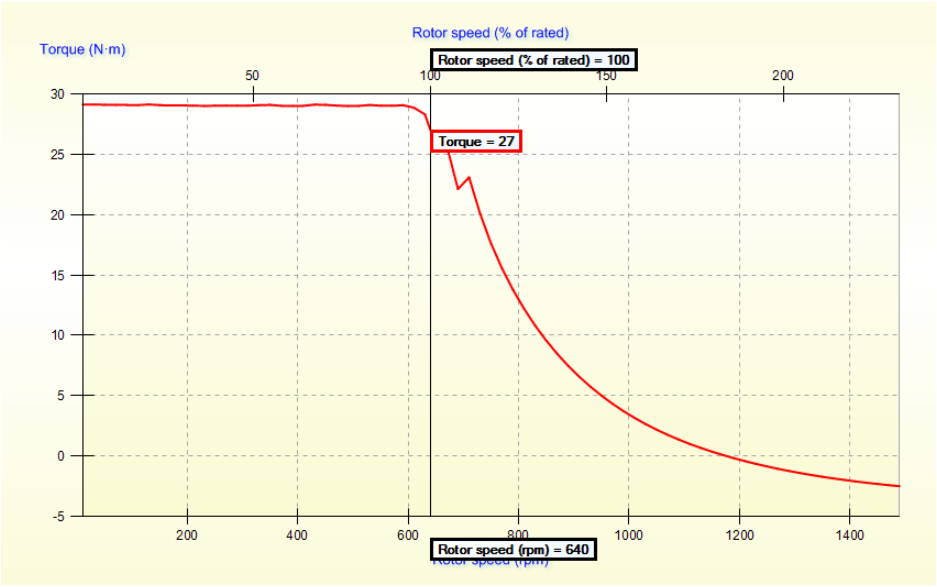

Figure 7.11 Torque Vs speed curve of the optimised motor

In the field weakening, after base speed, the torque starts reducing because of increasing current in d-axis. Assuming field oriented control, optimal advance angles should be applied at each speed to find the maximum torque and keep the power constant up to a maximum speed of 2400rpm. With constant output power, the torque required at 2400rpm is (6.69Nm). At maximum speed, the generated torque at different advance angles from 0° to 90° was simulated on FEA, as shown in Figure 7.12. The figure shows that the required torque was achieved at 62.5° advance angle.

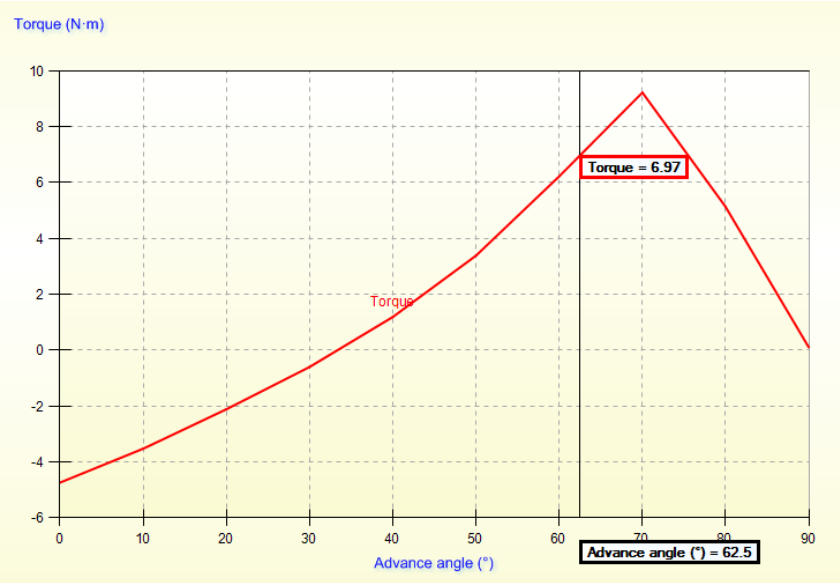

Figure 7.12 Peak torque at each speed at optimal advance angle

As the maximum advance angle is now known, the generated torque can be analysed on FEA to examine the machine performance in terms of torque and output power. The torques were over the full speed range from 0 to 2400rpm with six different advance angles between 0° and 62.5°, as shown in Figure 7.13. The results show that torque gradually reduced on each occasion the speed and advance angle increased.

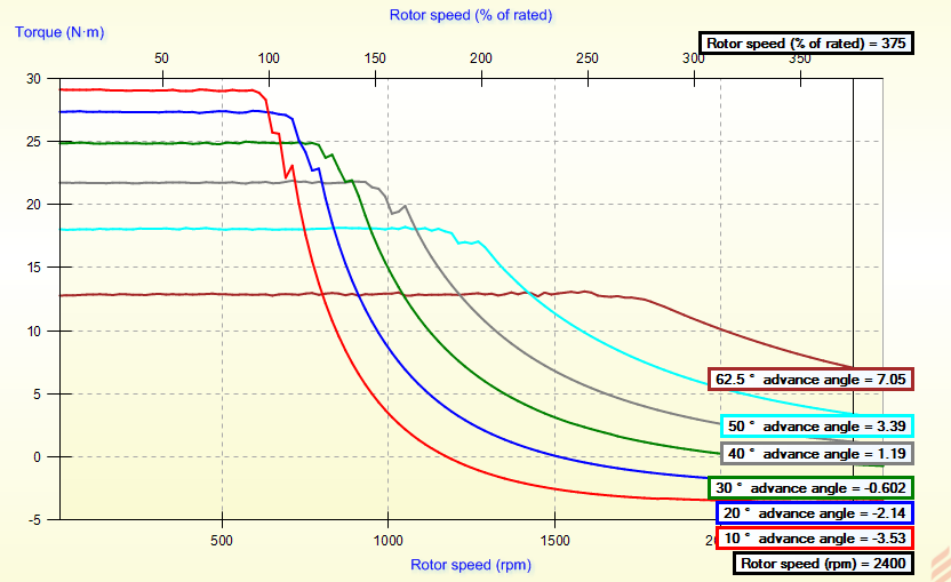

Figure 7.13 Generated torque over full speed range at different advance angle

The output power was also examined over the full speed range and different advance angle, as shown in Figure 7.14. The FEA simulation shows that the motor can generate the required power at base-speed 640rpm and higher power over the field weakening region up to the full speed 2400rpm. The higher generated power in the field weakening region is desired to drive the vehicle over uphill and cruising operations.

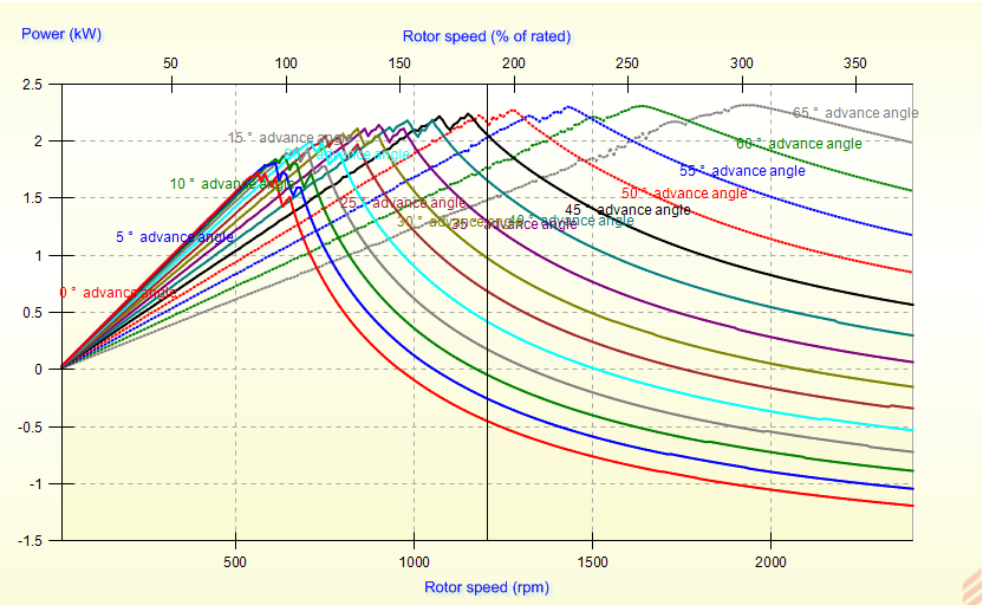

Figure 7.14 Generated power over full speed range at different advance angles

From the above graphs for torque and power over the full speed range and different advance angles, the operation characteristics of the optimised motor for torque and power over the full speed range can be plotted as shown in Figures 7.15 and 7.16 respectively. Both plots show that the motor at the rated current has the capability to generate higher torque and power.

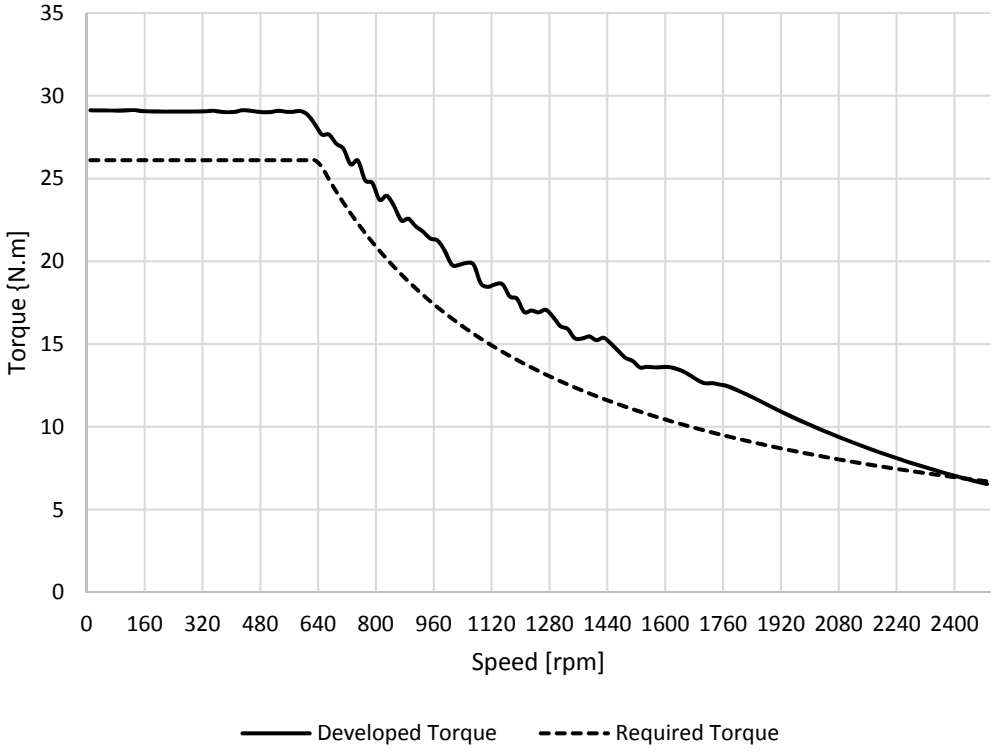

Figure 7.15 Torque/Speed characteristics of the optimised motor over the full speed range

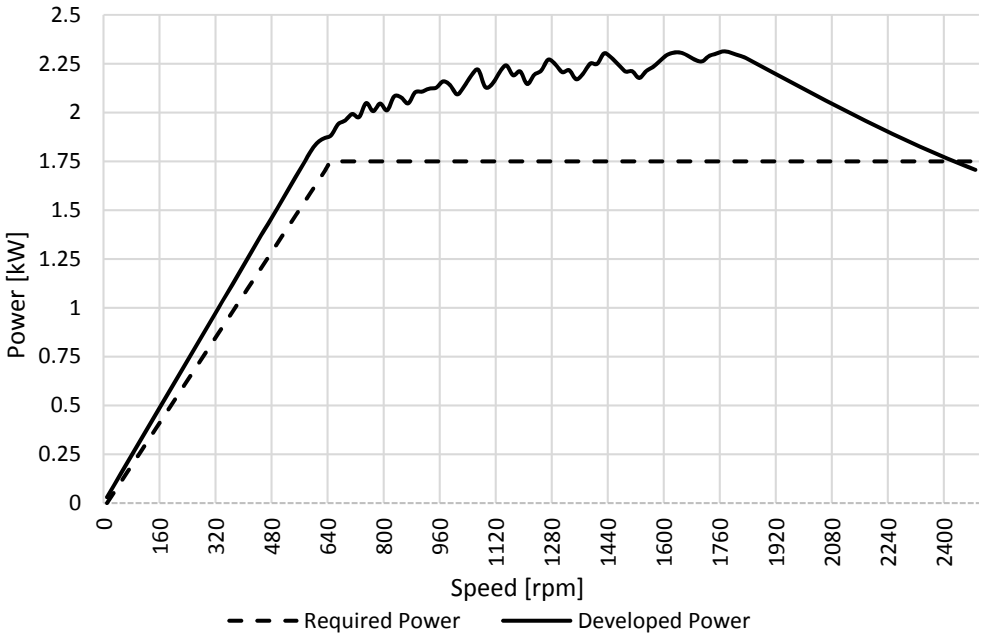

Figure 7.16 Power/Speed characteristics of the optimised motor over the full speed range

7.4.6 Losses

At load condition, FEA generates the sum of losses containing the copper and iron losses, including hysteresis and eddy current losses. The total losses, as generated from FEA, are 226W, as shown in Table 7.5. The maximum loss was in the copper 211W (~93.3%) and the total iron loss is 9.4W (6.7%).

Table 7.5 Component losses generated from FEA.

	8 poles/9 slots
Loss - Total (kW)	0.226
Loss - Winding (kW)	0.211
Loss - Iron (kW)	0.00941
Loss - Stator back iron (kW)	0.00361
Loss - Stator teeth (kW)	0.00557
Loss - Rotor back iron (kW)	0.000234
Loss - Magnet 1 (kW)	0.00488

7.4.7 Saturation and demagnetisation analysis

Taking into account all sources of flux from the permanent magnet and armature reaction, the maximum flux density in the stator lamination can be observed at load condition in FEA flux function analysis as shown in Figure 7.17. The maximum flux density was observed in the stator yoke of 1.64T. The highest flux density of 1.7T was observed in a smaller width area i.e. stator teeth-tip.

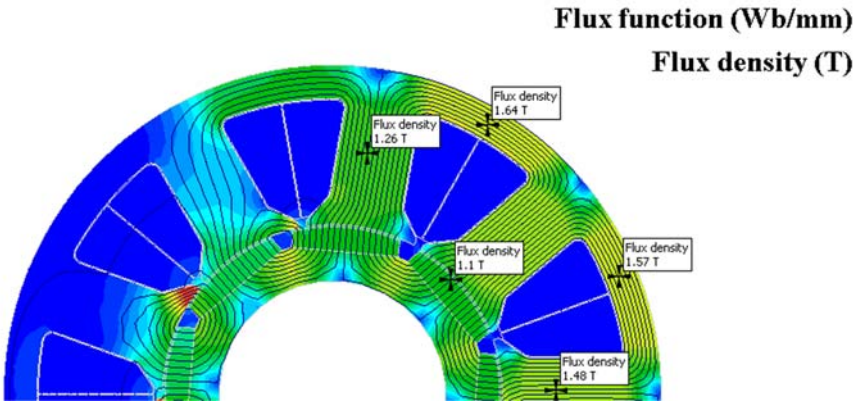

Figure 7.17 Flux distribution in the optimised machine components

With regard to demagnetisation, at rated operation temperature 150°C, the demagnetisation current was calculated in the analytical design as 37.14A. This current value is much higher than the rated current. This means the magnet is protected from demagnetisation at normal operating condition. However, at fault condition, the locked-rotor condition was assumed and the current was limited by the phase resistance R_{ph} and leakage inductance, i.e. L_{sl} and L_{ew} only. The locked-rotor current I_{LR} was calculated as 10.78A. As the locked-rotor current is lower than the demagnetisation current, the permanent magnet is expected to withstand demagnetisation. Therefore, using the locked-rotor current, the optimised machine was analysed under fault condition to ensure there is no partial demagnetisation. The

results, as shown in Figure 7.18, show that there is no risk of demagnetisation at any magnet pole. This indicates that the magnet is safe under fault condition.

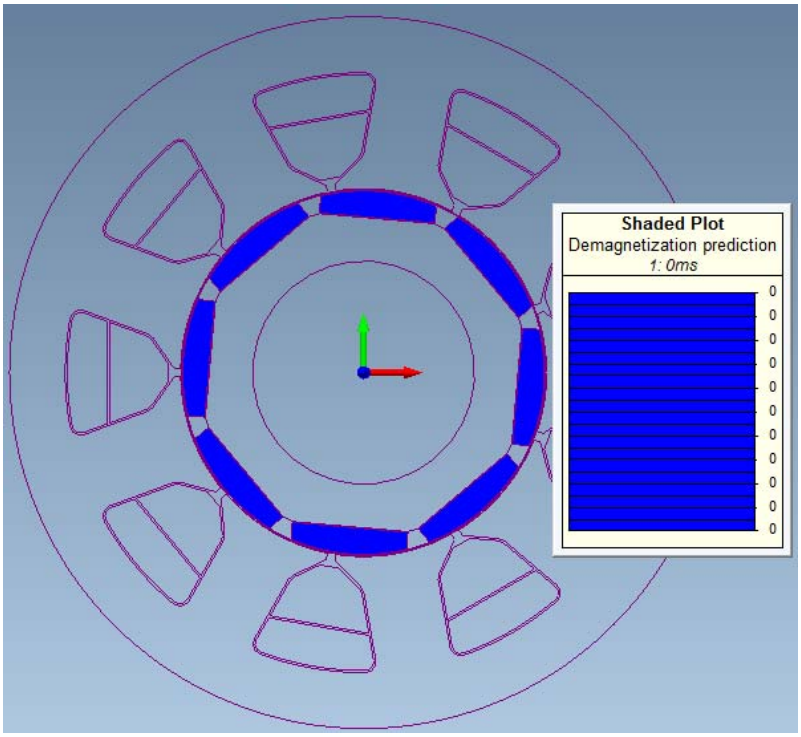

Figure 7.18 Demagnetisation test of the optimised motor under fault condition

7.4.8 Efficiency map

Performance analysis represented by an efficiency map was created for the optimised design. The data points for each efficiency were taken from 50rpm to 2400rpm with 50rpm increment and from 0 N.m increasing in 5N.m increment to a final torque value at each speed. By increasing the current from 0 to its maximum value and advance angle from 0 to 62.5 to reach the highest torque at each speed, the minimum efficiency was read off 90% at the base speed 640rpm and higher efficiencies of ~94% were developed through the field weakening region up to maximum speed, as shown in Figure 7.19.

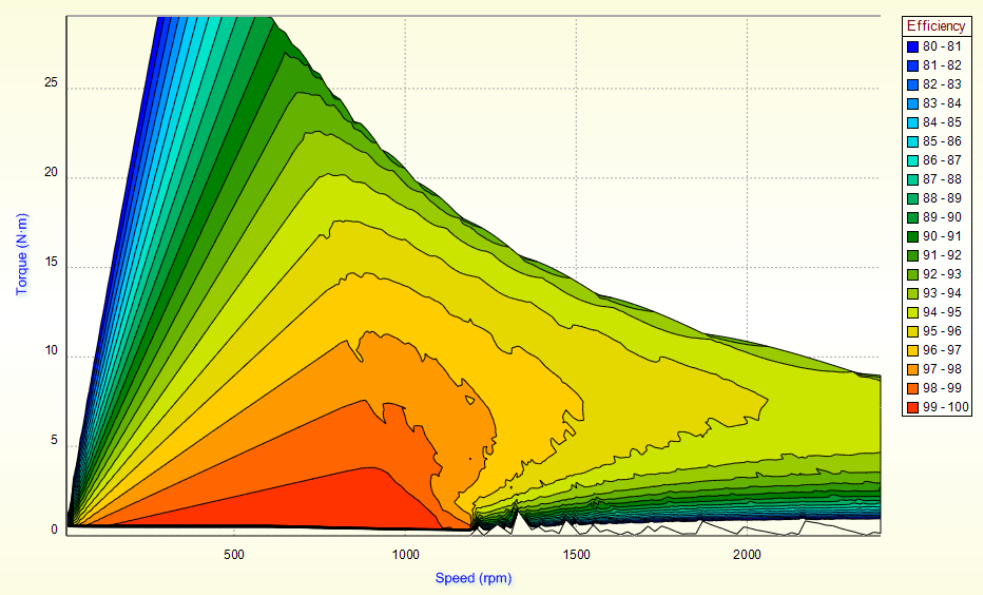

Figure 7.19 Efficiency map of the optimised design

7.4.9 FEA thermal analysis

After the definition of the machine dimensions and materials, FEA thermal analysis under rated loading condition was simulated with natural cooling. To reach temperature stability, the simulation was run for 180 minutes over 180 cycles. The temperature rises, as shown in Figure 7.20, illustrate that maximum temperatures were read-off 135°C and 134°C at the end-winding and magnet respectively. In other machine components, the temperatures range between 121°C in the rotor back-iron and 125°C in the stator core.

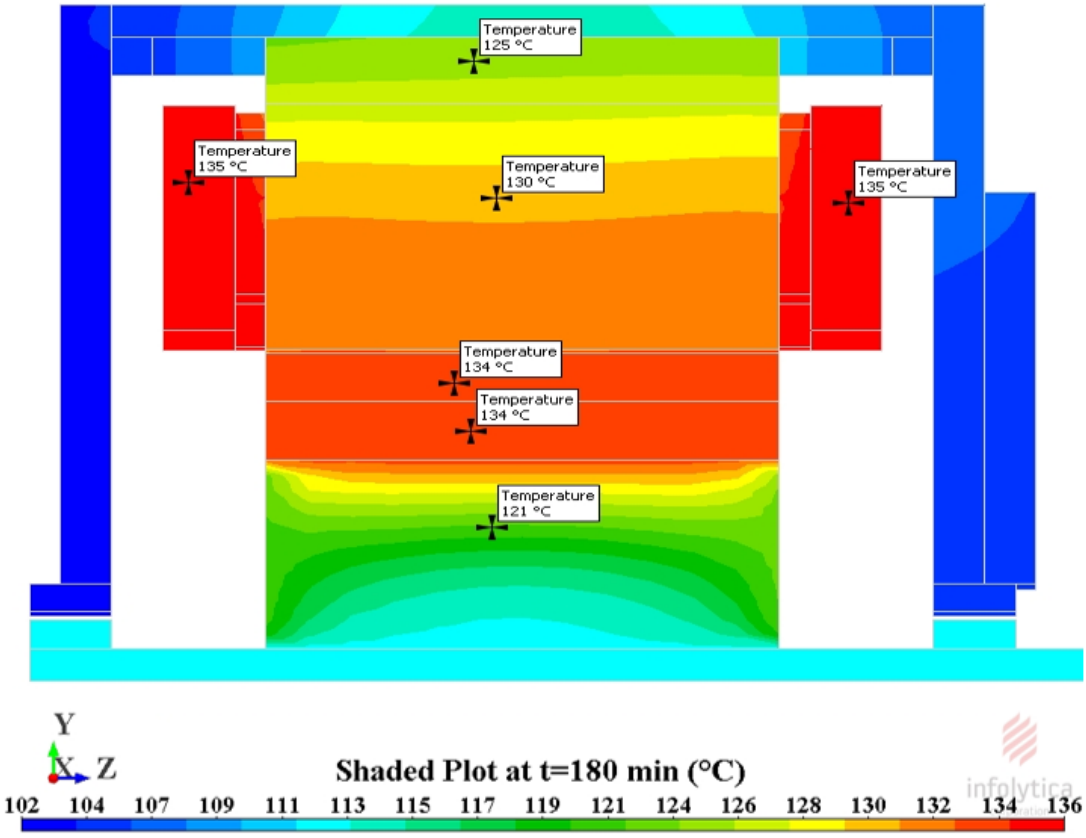

Figure 7.20 FEA thermal analysis of the optimised machine at load condition

7.5 Comparison of the results of analytical design with FEA simulation

As mentioned earlier, the FEM analysis is required to validate the parameters evaluated in the analytical model. The comparisons between the analytical results and the FEA computations are summarised in Table 7.6. The deviation is within a range of 10%, which is acceptable for a first order analytical modelling [12]. The maximum deviation was in the end-winding inductance and iron loss at 8% and 6% respectively.

Table 7.6 Comparison of results from analytical and FEA simulations

Parameters	Analytical result	FEA results	Deviation %
Airgap flux density [T]	0.946	0.987	4.2%
Back-EMF [V]	103.28	106.23	2.8%
Torque [N.m]	26.1	27.25	4.2%
Inductance [mH]	60.4	65.5	7.8%
End-winding Inductance [mH]	2.1	1.84	8%
Iron loss [W]	8.8	9.41	6%
Winding Losses [W]	207.244	211	2.2%
Total losses [W]	215.25	226	4.8%
Max flux density [T]	1.6	1.64	2.4%
Efficiency [%]	89.04	90	1%
Magnet Temp. [°C]	128	134	4.5%
End-winding Temp. [°C]	140	135	3.7%

The first fundamental of airgap flux density B_{g1} was underestimated in the analytical model by 4.2%, probably because of the flux leakage factor considered as 95% of the magnetic flux participating in the energy conversion. The FEA simulation of the optimised machine, as shown in Figure 7.21, shows only a very small portion of flux having been leaked between magnet poles. Therefore, a leakage factor higher than 0.95 should be considered for a small machine. The other reason that might have caused underestimation of the airgap flux density is the effect of saturation factor on the magnetic circuit, which was completely neglected in the analytical approach.

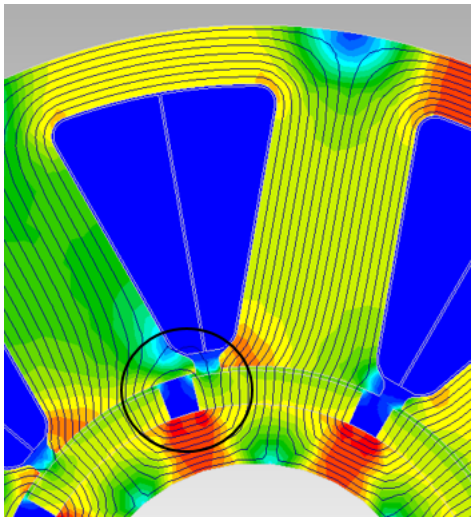

Figure 7.21 FEM analysis of the magnetic flux leakage between poles

However, as the airgap flux density was the first parameter estimated in the analytical approach, other machine dimensions and parameters were calculated based on its value. An underestimation of the airgap flux density is expected to be reflected in the other parameters with linear or nonlinear relationships. This can be clearly seen in the value of the back-EMF and the maximum flux densities of the stator yoke and teeth in Table 7.6. The generated back-EMF and maximum flux density were underestimated in the analytical design, with almost the same ratios of the airgap flux density, 2.8% and 2.4% respectively.

The inductance and iron loss in both stator back-iron and stator teeth were also underestimated in the analytical design, due to the deflection of the airgap flux density. However, due to the non-linear relation between the flux density and both inductance and iron loss, the ratios of deviations were higher at 8% and 6% respectively.

The total losses in FEA analysis also show a slight deviation of 5.8% in comparison with the analytical design. The first reason is the under estimation of the iron loss. However, the second reason is the eddy current loss in the magnet that has been

entirely neglected in the analytical approach; this is also clearly seen in the magnet temperature that increased by 4.5% in the FEA analysis.

In spite of the variation between the analytical and FEA results, the electromagnetic and thermal FEA simulations show that the performance of the optimised machine, using the optimal prime variables generated from BA, is capable of delivering the required powers and torques at rated operation condition without any overheating in the machine components. Therefore, the final optimised machine design is considered as appropriate and compatible with the required specifications.

7.6 Evaluation of performance indices

As shown in the previous section, the FEA analysis shows that both desired levels of torque and output power were achieved in the optimised design. Moreover, efficiency was slightly improved and temperatures in different active parts of the machine were lower. Therefore, it is apparent that the analytical model was accurately designed to achieve the output specifications of the machine within a limited operating temperature. However, the main objective of the optimisation was to find an alternative optimal machine design that had higher power density and efficiency. In other words, we need to minimise the machine weight while retaining the output power and efficiency at a higher, or at least the same, level as the benchmark design. To compare the overall achievement of the optimisation, the performance indices of both optimised and benchmark machines need to be compared. Table 7.7 shows the comparison of the performance indices for both machine designs.

Table 7.7 Performance indices comparison of the optimised and benchmark designs

Performance index	Optimised design	Benchmark design	Achievement
Total weight [kg]	6.64	7.92	19%
Magnet Weight [kg]	0.4051	0.53	24%
Volume [L]	1.0	1.64	39%
Efficiency [%]	89.04	90.2	1%
Objective Function	35.73	44.92	20.5%

Although the outer diameter in the optimised design was increased from 124.9mm in the benchmark to 159.8mm in the optimised design, the machine axial length was reduced from 114mm to 50.05mm. Compared with the benchmark design, the weight of the optimised machine was reduced by 19%. Hence, the reduction in the machine weight was mainly due to the optimisation of the machine axial length *L*. However, the reduction in the machine weight led to an improvement in the machine power-density kW/kg. Both benchmark and optimised machines generated the same output power 1.75kW; the weight of the optimised machine was 19% lower than the benchmark design. Thus, the power density of the optimised machine improved from 0.221 kW/kg to 0.263 kW/kg.

The improvement of the machine weight was also reflected in the machine volume. Although similar end-winding extension 10mm was assumed for both machines, the volume of the optimised machine was 39% smaller. This also led to improvement in the power-to-volume ratio from 1.067 kW/Litre in the benchmark design to 1.75Kw/litre in the optimised machine.

Low cost and high efficiency are extremely desirable in electric machine design for automotive applications. In the industrial market, they are the most important criteria to attract customers. Due to fluctuation in the magnet prices over the years, the cost of the machine was not calculated in the optimisation problem and therefore not included in the objective function. Instead, as the permanent magnet is the most cost effective part of the machine, this performance index was replaced by the weight of magnets. For the sake of fair comparison, the same grade of magnet (NdFeB 230/220h) was considered in both benchmark and optimised designs.

As shown in the formula of objective function, the performance index, weight of magnet W_{mag}, has been multiplied by magnificent factor 20 to indicate the importance of this index. Furthermore, the maximum magnet's weight was constrained in the analytical model to the maximum weight of the benchmark design. As shown in Table 7.7, optimisation could reduce the weight of the permanent magnet by 24%. Taking into account the reduction weight in the other machine materials, the cost of the new optimised machine would be lower than the benchmark design.

From a scientific point of view, the reduction in the permanent magnet has a significant effect on the output power of the machine, making it lower. However, in the optimised design, the equivalent number of turns per phase was higher compared with the benchmark design. Therefore, the reduction in the magnetic-loading was on account of the electric-loading, as shown in Equation 2.1.

However, due to the optimisation of the machine length, the reduction of the expensive permanent magnet weight was not only on account of the increase in weight of the cheaper copper from 1.69kg in the benchmark design to 2.34kg in the optimised

design. It was, in fact, on account of the increase in weight of the lamination steel, which resulted from increasing the ratio between the stator outer and inner diameters. Hence, this can enhance the cost index of the motor, as the steel is much cheaper than magnet and copper.

Finally, despite the inverse relation between efficiency and overall machine weight, compared with the benchmark design, the results show that the optimised machine has maintained the same efficiency. Thus, the improvements gained on the other performance indices have prevented the optimisation from further improving efficiency.

7.7 Chapter summary

In this chapter, the optimal prime variables generated from BA were used to build the new optimised machine. A comprehensive electromagnetic and thermal analysis was presented, based in the analytical approach as described in Chapter 4. The results from the analytical design were verified based on FEA analysis. The output power, losses, torque of the new optimised design were also assessed and validated through FEA analysis.

Compared with the benchmark design, the new optimised machine has benefited from lighter weight and smaller volume and, therefore, higher power density and higher power-to-volume ratio. Moreover, the cost of the optimised machine was lower due to the optimisation of permanent magnet weight that needed to generate the specified output power. Also, the simulation of the torque and power throughout the range speed show that the optimised machine has maintained the same efficiency as in the benchmark design.

8 Chapter 8: Conclusions, Contribution and Recommendation for future work

8.1 Conclusions

The design of electric machines is a complex task and a comprehensive process, consisting of electromagnetic, mechanical and thermal models that cannot be designed separately from each other. The optimisation of an electric machine design involves evaluation of continuous and discreet variables that have nonlinear relations in most cases. The optimisation problem usually involves multi-objectives that conflict with each other, such as weight, cost and efficiency. This makes the objective function of the optimisation problem non-linear and having no analytical expressions.

In this thesis, Bees Algorithm has been introduced and applied to search for optimal parameters of electric machines. Unlike other stochastic optimisation algorithms that has strength to perform either global search or local search; the Bees Algorithm has the ability to perform both exploitative neighbourhood search and explorative global search for constrained optimisation problem with multi-objective function. The ability to perform global and local searches makes the Bees Algorithm to be considered as a practical approach when selecting optimisation algorithm to solve engineering problems.

Generally, Stochastic optimisation has the disadvantage of being not efficient due to their large computation time and large numeric field processes. In contrast, the Bees Algorithm has only six parameters and comparatively needs less programming efforts. In addition, as the best optimisation is the one that is able to efficiently survey the search space and produce the optimal solution with minimum number of iterations. The calibration procedure revealed that the search space of the Bees Algorithm can be significantly reduced when the six algorithm parameters are tuned compatible with the available resources and the expectation of the final design. Furthermore, as the optimal solution of engineering problems is generally exist around local search, special attention should be paid to calibrate the parameters associated with the neighbourhood search. The results show that when solving problem with comparatively diverse boundaries, the adaption of particular neighbourhood size of each prime variables helped the bees to avoid overshooting and significantly increase the optimisation's performance to find better solutions quickly and efficiently.

The specifications of the new optimised machine are based on the benchmark design of 1.75kW at 640rpm used for traction application. The objective of the optimisation was to find an alternative prototype with higher power density and efficiency and lower cost. Based on the optimal prime variables generated from Bees Algorithm, the analytical model was evaluated and the electromagnetic and thermal parameters were verified by FEA computation.

The results show that the new optimised motor is capable of meeting the requirements of the design specifications at rated operating conditions. The performance indices of the new optimised design were evaluated and compared with their corresponding

values in the benchmark design. The comparison shows that the new optimised machine has maintained the same efficiency as in the benchmark design and power density and the volume-to-power ratio were improved by 16% and 39% respectively. In the objective function, the cost of the machine was represented by the weight of the permanent magnet materials. Compared with the benchmark design, the cost of the optimised machine was reduced by 24%.

The conclusion from each chapter was summarised as follow:

Chapter 1 has provided a general background of electric machine design and optimisation and given brief information about the objective of this research.

In Chapter 2, the old traditional method to design electric machines has been reviewed. It has shown that this method has been mainly based on typical sizing equations and data from typical curves for a limited number of materials that do not reflect modern improvement in applications, materials and power electronics. It has been shown that the design of electric machines, through the traditional method, has insufficiency by carrying out a separate thermal analysis that was not connected with magnetic and electric loadings throughout the design process. Also in this chapter, brief descriptions of search procedure of the most widely applied optimisation algorithms in the electric machine design have been presented and compared with the searching criteria of Bees Algorithm. The survey presented in this section has shown the need for developing a machine design and optimisation algorithm that can reflect modern improvement in the electric machine design and efficiently search for the optimal solution. Finally, the most significant developments in electric machine optimisation on the last decade were surveyed in this chapter, including surrogate modelling of electric machine and

direct and stochastic search for both single- and multi-objective design optimisation problems.

Chapter 3 has studied the different numerical and analytical methods used to compute magnetic field problem and addressed the key factors for each proposed method. The advantage and disadvantage of integrating these methods with algorithm to search for optimal solution has been illustrated. It has been concluded by this review that FEA is the most accurate method currently used to analyse electromagnetic and thermal behaviour of electric machines. However, due to the long computational time, FEA cannot be integrated into the optimisation process. This chapter has also presented the characteristics of permanent magnet materials and their behaviours in magnetic circuit at different operation conditions. Finally, a full analysis of a magnetic circuit in a surface mounted permanent magnet machine and the determination of airgap flux density value have been illustrated by the means of "Equivalent Magnetic Circuit".

Chapter 4 provided full assessments of the benchmark machine used in traction applications. The electromagnetic and thermal analysis of the benchmark design has been carried out throughout FEA analysis. The characteristics of torque, power and efficiency of the benchmark has been simulated over full speed range. Finally, the performance indices of the benchmark design in terms of power density, power-to-volume ratio, and torque constant have been evaluated as compared with the optimised design.

In Chapter 5, the full analytical model of surface mounted permanent magnet machine with good accuracy has been developed. First, the proposed analytical model has illustrated the method of determining optimal values for some of the electric machine

parameters prior to optimisation search to reduce the optimisation search space and to enhance the machine performance. This includes the selection of the number of slots and poles, magnet shape and magnet-arc to pole-arc ratio. Moreover, the analytical design has been prepared to accurately calculate all electromagnetic, thermal and losses of the electric machine. The analytical model has also been integrated with constraints and penalty functions to ensure the delivery of a feasible design and to protect the machine from deteriorating under certain operating conditions. Finally, the multi-objective function has been designed to reduce the machine weight, volume and cost and increase the efficiency.

Chapter 6 has presented the criteria that Bees Algorithm follows to search for optimal variables. Throughout this chapter, the definition of optimisation terms associated with Bees Algorithm has been explained and the influence of each parameter on the algorithm performance was evaluated. The method of setting parameters for Bees Algorithm to effectively search for optimal electric machine design has been detailed. The relation between the algorithm parameters, search space boundaries and the variables in the optimisation problem has been explained and recommendation of how to set these parameters, particularly for electric machines, has been suggested. Also, in term of computational efficiency and probability to find optimal solution, the Bees Algorithm was compared with genetic algorithm using predefined objective value.

Chapter 7 shows the optimal prime variables generated from Bees Algorithm with best fitness objective function. The optimal values have been used as input for the optimisation problem, analytical model, to evaluate electromagnetic and thermal parameters for the new optimised electric machine. The resulting parameters of the

new optimised electric machine have been verified throughout the proposed analytical design method and their values verified by FEA analysis. The performance indices of the new optimised machine have been evaluated and compared to their corresponding values in the benchmark design. The results show that the new optimised machine has better power density and lower volume. Results also show that the amount of permanent magnet materials used in the new optimised machine was lower than that in the benchmark design. Subsequently, the cost of the optimised machine is lower than the benchmark design. Furthermore, despite the reduction in the weight and volume of the new optimised machine, the efficiency was equal in both optimised and benchmark motors. Moreover, the performance of the new optimised machine has been assessed over full speed range and the results show that the new optimised machine has the capability of developing the required torque on the constant torque region and the required power along the constant power region.

8.2 Contributions

The main scientific achievements and contributions of this research are summarised as follows:

1. To explain the traditional machine design method and highlight the drawback of applying this method on the light of modern improvement of materials, applications and power electronics. To present a comprehensive literature review of the optimisation algorithms most utilised in electric machine design with emphasis on their different search criteria and their ability to reflect constraints and specifications.

2. To compute a comprehensive analytical design model for surface-mounted permanent magnet machine that covers all the evaluation of electromagnetic and thermal parameters based on the values of four prime variables. The model also includes constraints and penalties to guarantee the production of a visible prototype design. The model is based on specified design requirements and actual material properties and does not need manual design iterations.
3. A novel application of Bees Algorithm in electric machine design. With carefully tuning six parameters the algorithm has the ability to effectively perform a combination of exploitive neighbourhood search and explorative global search. Based on the optimisation problem and prime variables, parameters setting pattern have been suggested to efficiently search for an optimal solution to the electric machine design problem.
4. The Bees Algorithm was compared with Genetics Algorithm to find optimal solution for a predefined objective value. Providing that both algorithm have been set with the same number of populations and iterations to search the same space; the results from multiple runs show that the probability and the computational efficiency to find an optimal solution, with higher fitness value than benchmark objective was 80% in BA comparing with 50% in GA. Also, on the same analysis, the standard deviation of the average fitness values obtained from BA was 1.4 comparing with 2.82 in GA. Furthermore, When the search space of the optimisation problem was increased; again, BA has shown higher ability to cover the search space and find a fitness solution that better than GA.

5. Design of a new electric machine that comparatively benefits from light weight, small volume, low cost and high efficiency. Compared with the benchmark design, the new designed machine, with the same materials, has the capability to generate the same output power and torque at the same efficiency while it has 19% higher power density, 39% lower volume and 24% lower cost.

8.3 Recommendation for future work

The calculation of the airgap flux density was underestimated in the analytical model. Subsequently, this caused deviation in the values of other parameters that mainly depend on the airgap flux density to be evaluated, such as back EMF, current, saturations. Therefore, it is necessary to construct a more accurate "equivalent magnetic circuit" to estimate the airgap flux density. For example, an evaluation of magnetic field in the airgap solved in Fourier series and taking into account the harmonics components could generate more accurate results. The evaluation of the losses of the machine can be improved further by additional evaluation of eddy current loss of permanent magnet. The thermal analysis could also be improved further by adopting a thermal network with a higher number of nodes that consider the heat distribution in all directions.

9 References

[1] “C. C. Chan, “The state of the art of electric and hybrid vehicles,” Proc. IEEE, vol. 90, no. 2, pp. 247–275, Feb. 2002.”.

[2] “T. M. Jahns et al., "Design and Experimental Verification of a 50 kW Interior Permanent Magnet Synchronous Machine," Conference Record of the 2006 IEEE Industry Applications Conference Forty-First IAS Annual Meeting, Tampa, FL, 2006, pp. 1941-1948.”.

[3] “Honda, Y., Nakamura, T., Higaki, T. and Takeda, Y., “Motor design considerations and test results of an interior permanent magnet synchronous motor for electric vehicles,” IEEE Industry Applications Society Annual Meeting IAS ’97, vol. 1, New Orleans, LA,”.

[4] “Husain I. Electric and Hybrid Vehicles Design Fundamentals. CRC Press, ISBN 0-8493-1466-6; 2003”.

[5] “Zhu ZQ, Howe D. “Electrical machines and drives for electric, hybrid, and fuel cell vehicles”, Proceedings of the IEEE 2007; 95(4): 746–65.”.

[6] “Design Methodology for Small Brush and Brushless DC Motors Jérôme Cros, Mehdi Taghizadeh Kakhki, Geraldo C.R. Sincero, Carlos A. Martins, Philippe Viarouge”.

[7] “M. G. Say, Performance and design of AC machines: Pitman, London, 1970, ISBN: 273 40199 8.”.

[8] “V. B. Honsinger, "Sizing equations for electrical machinery," IEEE Transactions on Energy Conversion, vol. 2, pp. 116-121, May 1987.”.

[9] “Gieras, Jacek F. Permanent magnet motor technology: design and applications / Jacek F. Gieras. -- 3rded.”.

[10] “F. Fu and X. Tang, Induction machine design handbook: China Machine Press, 2002.”.

[11] “William H Yeadon, Bradley M Frustaglio,"Electromagnetic system and devices-current density," SMMA Fall Conference 2010”.

[12] “Jannot, X.; Vannier, J.-C.; Marchand, C.; Gabsi, M.; Saint-Michel, J.; Sadarnac, D., "Multiphysic Modeling of a High-Speed Interior Permanent-Magnet Synchronous Machine for a Multiobjective Optimal Design," Energy Conversion, IEEE Transactions on , v”.

[13] “Wolpert, D.H.; Macready, W.G. No free lunch theorems for optimization Evol. Comput. IEEE1997, 1, 67-82.”.

[14] “G. F. Uler, O. A.Mohammed, and K. Chang-Seop, “Design optimization of electrical machines using genetic algorithms,” IEEE Trans. Magn., vol. 31, no. 3, pp. 2008–2011, May 1995.”.

[15] “Pham, D.T.; Ghanbarzadeh, A. Multi-Objective Optimisation Using the Bees Algorithm. In Proceedings of the IPROMS 2007 Conference, Cardiff, UK, 2013 July 2007.”.

[16] “N. Bianchi, S. Bolognani and P. Frare, "Design criteria of high efficiency SPM synchronous motors," IEEE Transactions on Energy Conversion, vol. 21, pp. 396-404, June 2006.”.

[17] “C. Blache and D. Paccard, "Magnetic structure design method," IEEE Transactions on Magnetics, vol. 29, pp. 2228-31, Sep. 1993.”.

[18] “J. H. Holland, "Adaptahon in natural and Wcial systems", MlT PES, 1992.”.

[19] “S. N. Sivanandam and S. N. Deepa, Introduction to Genetic Algorithms., 1st ed. New York, NY, USA: Springer-Verlag, 2008.”.

[20] “Li, L.; Liu, F. Group Search Optimisation for Application in Structural Design; Springer: Berlin, Germany, 2011.”.

[21] “R. Wrobel and P. H. Mellor, “Design considerations of a direct drive brushless machine with concentrated windings,” IEEE Trans. EnergyConvers., vol. 23, no. 1, pp. 1–8, Mar. 2008.”.

[22] “Y. Ahn, J. Park, C. Lee, J. Kim, and S. Jung, “Novel memetic algorithm implemented with GA (genetic algorithm) andMADS (mesh adaptive direct search) for optimal design of electromagnetic system,” IEEE Trans. Magn., vol. 46, no. 6, pp. 1982–1985, Jun. 2010”.

[23] “Yong-Hwan Oh; Tae-Kyung Chung; Min-Kyu Kim; Hyun-Kyo Jung, "Optimal design of electric machine using genetic algorithms coupled with direct method," Magnetics, IEEE Transactions on , vol.35, no.3,pp.1742, 1745, May1999 doi: 10.1109/20.767366”.

[24] “Eberhart, R. C., Dobbins, R. W., and Simpson, P. K. (1996), Computational Intelligence PC Tools, Boston: Academic Press. 3. Eberhart, R. C., and Kennedy, J. (1995), A new optimizer using particle swarm theory, Proc. Sixth International Symposium on Micro”.

[25] “Shi, Y. H., Eberhart, R. C., (1998), A modified particle swarm optimizer, Proc. of 1998 IEEE International Conference on Evolutionary Computation, Anchorage, AK, in press.”.

[26] “A. A. Arkadan, M. N. ElBsat, and M. A. Mneimneh, “Particle swarm design optimization of ALA rotor SynRM for traction applications,” IEEE Trans. Magn., vol. 45, no. 3, pp. 956–959, Mar. 2009.”.

[27] “Y. Duan and R. G. Harley, “A novel method for multi-objective design and optimization of three phase induction machines,” in Proc. ECCE, 2010, pp. 284–291.”.

[28] “M. Ashabani and Y.-R. Mohamed, “Multiobjective shape optimization of segmented pole permanent-magnet synchronous machines with improved torque characteristics,” IEEE Trans. Magn., vol. 47, no. 4, pp. 795–804, Apr. 2011”.

[29] “J. Seo, C. Im, S. Kwak, C. Lee, and H. Jung, “An improved particle swarm optimization algorithm mimicking territorial dispute between groups for multimodal function optimization problems,” IEEE Trans. Magn., vol. 44, no. 6, pp. 1046–1049, Jun. 2008.”.

[30] “J. Seo, S. Kim, and H. Jung, “Rotor-design strategy of IPMSM for 42 V integrated starter generator,” IEEE Trans. Magn., vol. 46, no. 6, pp. 2458–2461, Jun. 2010.”.

[31] “Pham DT, Ghanbarzadeh A, Koc E, Otri S, Rahim S and Zaidi M. The Bees Algorithm. Technical Note, Manufacturing Engineering Centre, Cardiff University, UK, 2005.”.

[32] “Pham, D.T.; Marzi, H.; Marzi, A.; Marzi, E.; Darwish, A.H.; Lee, J.Y., "Using grid computing to accelerate optimization solution: A system of systems approach," System of Systems Engineering (SoSE), 2010 5th International Conference on , vol., no., pp.1,6”.

[33] “Packianather, M.S.; Yuce, B.; Mastrocinque, E.; Fruggiero, F.; Pham, D.T.;Lambiase, A., "Novel Genetic Bees Algorithm applied to single machine scheduling problem," World Automation Congress (WAC), 2014 , vol., no., pp.906,911, 3-7 Aug. 2014doi: 10.1109/W”.

[34] “Ang, M.C.; Pham, D.T.; Soroka, A.J.; Ng, K.W., "PCB assembly optimisation using the Bees Algorithm enhanced with TRIZ operators," IECON 2010 - 36th Annual Conference on IEEE Industrial Electronics Society , vol., no., pp.2708,2713, 7-10 Nov. 2010 doi: 10.”.

[35] “Tudu, B.; Majumder, S.; Mandal, K.K.; Chakraborty, N., "Optimal unitsizing of stand-alone renewable hybrid energy system using bees algorithm," Energy, Automation, and Signal (ICEAS), 2011 International Conference on , vol., no., pp.1,6, 28-30 Dec. 2011”.

[36] “Anantasate. S.; Bhasaputra, P., "A multi-objective bees algorithm for multiobjective optimal power flow problem," Electrical Engineering/Electronics, Computer, Telecommunications and Information Technology (ECTI-CON), 2011 8th International Conference on”.

[37] “Y. D. Chun, S. Wakao, T. H. Kim, K. B. Jang, and J. Lee, “Multiobjective design optimization of brushless permanent magnet motor using 3D equivalent magnetic circuit network method,” IEEE Trans. Appl. Supercond., vol. 14, no. 2, pp. 1910–1913, Jun. 2004.”.

[38] “L. Hsu, M. Tsai, and C. Huang, “Efficiency optimization of brushless permanent magnet motors using penalty genetic algorithms,” in Proc. IEEE Int. Electr. Mach. Drives Conf., Jun. 2003, vol. 1, pp. 365–369.”.

[39] “K. Han, H. Cho, D. Cho, and H. Jung, “Optimal core shape design for cogging torque reduction of brushless DC motor using genetic algorithm,” IEEE Trans. Magn., vol. 36, no. 4, pp. 1927–1931, Jul. 2000.”.

[40] “M. Lukaniszyn, M. JagieLa, and R. Wrobel, “Optimization of permanent magnet shape for minimum cogging torque using a genetic algorithm,” IEEE Trans. Magn., vol. 40, no. 2, pp. 1228–1231, Mar. 2004.”.

[41] “S. Sonoda, Y. Takahashi, K. Kawagishi, N. Nishida, and S. Wakao,“Application of stepwise multiple regression to design optimization of electric machine,” IEEE Trans. Magn., vol. 43, no. 4, pp. 1609–1612, Apr. 2007.”.

[42] “S. Giurgea, H. S. Zire, and A. Miraoui, “Two-stage surrogate model for finite-element-based optimization of permanent-magnet synchronous motor,” IEEE Trans. Magn., vol. 43, no. 9, pp. 3607–3613, Sep. 2007.”.

[43] “X. Meng, S. Wang, J. Qiu, J. G. Zhu, Y. Wang, Y. Guo, D. Liu, and W. Xu, “Dynamic multilevel optimization of machine design and control parameters based on correlation analysis,” IEEE Trans. Magn., vol. 46, no. 8, pp. 2779–2782, Aug. 2010.”.

[44] “K. Hameyer and R. Belmans, Numerical Modelling and Design of Electrical Machines and Devices, WIT Press, 1999.”.

[45] “W. Ouyang, D. Zarko and T. A. Lipo, "Permanent Magent Machine Design Practice and Optimization," 2006 IEEE conference on Industrial Applications, pp.1905-11, Tampa,FL, 2006.”.

[46] “Yong Li; Jibin Zou; Yongping Lu, "Optimum design of magnet shape in permanent-magnet synchronous motors," Magnetics, IEEE Transactions on , vol.39, no.6, pp.3523,3526, Nov. 2003 doi: 10.1109/TMAG.2003.819462”.

[47] “F. B. Fidel, G. C. Aurelio, and F. Roberto, "Determination of parameters in interior permanent-magnet synchronous motors with iron losses without torque measurement," IEEE Trans. Ind. Appl., vol. 37, no. 5, pp.1265-1272, Sep./Oct. 2001.”.

[48] “K. Yamazaki, "Torque and efficiency calculation of an interior permanent magnet motor considering harmonic iron losses of both the stator and rotor," IEEE Trans. Magn., vol. 39, no. 3, pp. 1460-1463, May 2003.”.

[49] “J. Y. Lee, S. H. Lee, G. H. Lee, J. P. Hong, and J. Hur, "Determination of parameters considering magnetic nonlinearity in an interior permanent manet synchronous motor," IEEE Trans. Magn., vol. 42, no. 4, pp.1303-1306, Apr. 2006.”.

[50] “T. Sebastian, G. R. Slemon, and M. A. Rahman, "Modeling of permanent magnet synchronous motors," IEEE Trans. Magn., vol. 22, no. 5, pp.1069-1071, Sep. 1986.”.

[51] “Rasmussen, C.B.; Ritchie, E., "A magnetic equivalent circuit approach for predicting PM motor performance," Industry Applications Conference, 1997. Thirty-Second IAS Annual Meeting, IAS '97., Conference Record of the 1997 IEEE , vol.1, no., pp.10,17 v”.

[52] “Design of High Performance Permanent-Magnet Synchronous Wind Generators”.

[53] “Design of brushless permanent magnet motor. Miller.”.

[54] “Zhu, Z.Q.; Howe, D., "Instantaneous magnetic field distribution in brushless permanent magnet DC motors. III. Effect of stator slotting," Magnetics, IEEE Transactions on , vol.29, no.1, pp.143,151, Jan 1993 doi: 10.1109/20.195559”.

[55] “T. M. Jahns, Soong, W.L., "Pulsating torque minimization techniques for permanent magnet AC motor drives-a review," IEEE Transactions on Industrial Electronics, vol. 43, pp. 791-794, April 1996.”.

[56] “Z. Q. Zhu, Howe, D, "Influence of design parameters on cogging torque in permanent magnet machines," IEEE Transactions on Energy Conversion, vol. 15,pp. 920-925, Dec. 2000.”.

[57] “Daohan Wang; Xiuhe Wang; Sang-Yong Jung, "Cogging Torque Minimization and Torque Ripple Suppression in Surface-Mounted Permanent Magnet Synchronous Machines Using Different Magnet Widths," Magnetics, IEEE Transactions on , vol.49, no.5, pp.2295,2298,”.

[58] “W. Fei and P. C. K. Luk, “A new technique of cogging torque suppression in direct-drive permanent-magnet brushless machines,” IEEE Trans. Ind. Appl., vol. 46, no. 4, pp. 1332–1340, Jul/Aug. 2010”.

[59] “L. Zhu, S. Z. Jiang, Z. Q. Zhu, and C. C. Chan, “Analytical methods for minimizing cogging torque in permanent-magnet machines,” IEEE Trans. Magn., vol. 45, no. 4, pp. 2023–2030, Apr. 2009.”.

[60] “D. G. Dorrell, M.-F. Hsieh, M. Popescu, L. Evans, D. A. Staton, and V. Grout, “A review of the design issues and techniques for radial-flux brushless surface and internal rare-earth permanent magnet motors,” IEEE Trans. Ind. Electron., vol. 58, no. 9”.

[61] “M. Kamiya, BDevelopment of traction drivemotors for the Toyota hybrid system,[presented at the Int. Power Electronics Conf.,Niigata, Japan, Apr. 4–8, 2005.”.

[62] “I. Boldea and S. A. Nasar, The induciton machine handbook, 1 ed.: CRC express, 2001, ISBN: 0-8493-0004-5.”.

[63] “W. Xiuhe, Y. Yubo, and F. Dajin, “Study of cogging torque in surface mounted permanent magnet motors with energy method,” J. Magn. Magn. Mater, vol. 267, no. 1, pp. 80–85, Nov. 2003.”.

[64] “Y. Yang, X. Wang, R. Zhang, T. Ding, and R. Tang, “The optimization of pole arc coefficient to reduce cogging torque in surface-mounted permanent magnet motors,” IEEE Trans. Magn., vol. 42, no. 4, pp. 1135–1138, Apr. 2006.”.

[65] “K. C. Kim, D. H. Koo, J. P. Hong, and J. Lee, “A study on the characteristics due to pole-arc to pole-pitch ratio and saliency to improve torque performance of IPMSM,” IEEE Trans. Magn., vol. 43, no. 6, pp. 2516–2518, Jun. 2007.”.

[66] “T. A. Lipo, Introduction to AC machine design, 2 ed.: University of Wisconsin Madison, 2004, ISBN: 13: 978-0974547022”.

[67] “Dajaku, G.; Gerling, D., "Determination of air-gap flux density due to magnets using the new analytical model," Electrical Machines (ICEM), 2010 XIX International Conference on , vol., no., pp.1,6, 6-8 Sept. 2010 doi: 10.1109/ICELMACH.2010.5607739”.

[68] “Miller, Tim, "Brushless permanent-magnet motor drives," in Power Engineering Journal , vol.2, no.1, pp.55-60, Jan 1988”.

[69] “J. Saari, “Thermal analysis of high-speed induction machines,” Acta Polytechnica Scandinavia, Electrical Engineering Series no. 90, Dissertation of Helsinki University of Technology, Espoo, Finland, 1998.”.

[70] “K. Altallah, “Rotor loss in Permanent-magnet brushless AC machines, ”IEEE Trans. Ind. Appl., vol. 36, no. 6, pp. 1612–1617, Nov. 2000.”.

[71] “J. D. Ede et al., “Effect of Axial segmentation of permanent magnets on rotor loss in modular permanent-magnet brushless machines,” IEEE Trans. Ind. Appl., vol. 43, no. 5, pp. 1207–1213, Sep. 2007”.

[72] “Wan-Ying Huang; Bettayeb, A.; Kaczmarek, R.; Vannier, J.-C., "Optimization of Magnet Segmentation for Reduction of Eddy-Current Losses in Permanent Magnet Synchronous Machine," Energy Conversion, IEEE Transactions on , vol.25, no.2, pp.381,387, June”.

[73] “J. Nerg, M. Rilla, and J. Pyrhonen, “Thermal analysis of radial-flux electrical machines with a high power density,” IEEE Trans. Ind. Electron., vol. 55, no. 10, pp. 3543–3554, Oct. 2008.”.

[74] “P. H. Mellor, D. Roberts, and D. R. Turner, “Lumped parameter thermal model for electrical machines of TEFC design,” Inst. Electr. Eng. Proc. B, vol. 138, no. 5, pp. 205–218, Sep. 1991.”.

[75] “S. Thieblin, “Analysis and modeling of thermal behavior of an electric motor under variable loads and speeds. Application to an electric vehicle motor,” Ph.D. dissertation, Univ. Poitiers, Poitiers, France, 1997.”.

[76] “Roberts, D. ‘The application of an induction motor thermal model to motor protection and other functions’. PhD thesis, University of Liverpool. 1986”.

[77] “Churchill, S. W., Chu, H. H. S. International Journal of Heat and Mass Transfer, vol. 18, p. 1049. 1972.”.

[78] “El-Gallad, M. El-Hawary, A. Sallam and A. Kalas, "Enhancing the particle swarm optimizer via proper parameters selection," Electrical and Computer Engineering, 2002. IEEE CCECE 2002. Canadian Conference on, 2002, pp. 792-797 vol.2. doi: 10.1109/CCECE.2”.

[79] “Krishnanand, K. N. and Ghose, D. 2009. Glowworm swarm optimization for simultaneous capture of multiple local optima of multimodal functions. Swarm Intelligence 3(2), pp. 87-124.”.

[80] “Advanced Traction Drive Motor Development Phase 1, UQM Technologies, September 2006.”.

10 Appendix

%%%%%%Bees Algorithm %%%%%%%%

```
clc; close all; clear all;

%% Setting the Parameter for the Algorithm
itr=50;                 % number of iterations
n= 50;                  % number of scout bees
e=2;                    % number of elite selected sites
m=10;                   % number of best selected sites
nep=15;                 % number of recruited bees around elite selected patches
nsp=5;                  % number of recruited bees around best selected patches
ngh=1;                  % Patch radius for neighbourhood search


%% Boundaries of prime variables

para1_max=150;          para1_min=50; % Boundaries of Stator inner diameter
para2_max=150;          para2_min=50; % Boundaries of axial length
para3_max=8;            para3_min=4;   % Boundaries of magnet thickness
para4_max=7.5;          para4_min=5;   % Boundaries of current density

F_result=zeros(itr,5);

%% Scoutbees: random search (only once)

U=X_random(n, para1_max, para2_max, para3_max, para4_max,para1_min,
para2_min, para3_min, para4_min );
for S= 1: n
   input = ([U(S,1),U(S,2),U(S,3),U(S,4)]);
   Par_Q(S,1)= BLPMSM_1_75kW_640RPM(input);
end
Q= sortrows([ U(:,1), U(:,2),U(:,3), U(:,4),Par_Q],5);
clear U;
l=0;
```

```
%% Iterations of the algorithm

tic
for k=1:itr                 % iterations
   for j=1:e                % number of elite selected patches
      for i=1:nep           % number of bees around elite patches
         U=bee_dance(ngh, Q(j,1), Q(j,2), Q(j,3),Q(j,4));
        if BLPMSM_1_75kW_640RPM([U(1),U(2),U(3),U(4)])< Q(j,5)
            Q(j,:)=[ U(1),U(2),U(3),U(4),BLPMSM_1_75kW_640RPM(U)];
         end
         l=l+1;
      end
   end

   %
_____________________________________________________________________
_
   for j=e+1:m                      % number of best selected patches
      for i= 1:nsp                  % number of bees around best patches
          U=bee_dance(ngh, Q(j,1), Q(j,2), Q(j,3),Q(j,4));
        if BLPMSM_1_75kW_640RPM([U(1),U(2),U(3),U(4)])< Q(j,5)
            Q(j,:)=[ U(1),U(2),U(3),U(4),BLPMSM_1_75kW_640RPM(U)];
         end
         l=l+1;
      end
   end

   %
_____________________________________________________________________
_

   for j=m+1:n
      U=X_random(n, para1_max, para2_max, para3_max,
para4_max,para1_min,para2_min,para3_min,para4_min);
      Q(j,:)=[U(j,1), U(j,2),U(j,3), U(j,4), BLPMSM_1_75kW_640RPM(U(j,:))];
        l=l+1;
   end

%_____________________________________________________________________
```

```
Q=sortrows(Q,5);

F_result(k,:)= Q(1,:);

end % iterations

Q(1,:)

xxx=1:itr;
figure(1)
plot(xxx,F_result(:,1),'-+',xxx,F_result(:,2),'-o',xxx,F_result(:,3),'-
*',xxx,F_result(:,4),'-s');
grid on
xlabel ('Number of Iteration')
ylabel (' Parameters Values')

figure (2)
plot(xxx,F_result(:,5),'-*');
grid on
xlabel ('Number of Iteration')
ylabel (' Output of Objective Function')

toc
```

%%%%%% Function for random initialisation %%%%%%

```
function X = X_random(n, para1_max, para2_max,para3_max, para4_max,
para1_min, para2_min, para3_min, para4_min )
   X = [para1_min+((rand(n,1)).*(para1_max para1_min)),
para2_min+((rand(n,1)).*(para2_max-para2_min)),
para3_min+((rand(n,1)).*(para3_max-para3_min)),
para4_min+((rand(n,1)).*(para4_max-para4_min))];
end
```

%%%%% Neighbourhood search function %%%%%%

```
function U=bee_dance(ngh,x1, x2, x3, x4)

   U(:,1)=(x1-ngh)+(2*ngh.*rand(size(x1,1),1));
   U(:,2)=(x2-ngh)+(2*ngh.*rand(size(x2,1),1));
   U(:,3)=(x3-ngh)+(2*ngh.*rand(size(x3,1),1));
   U(:,4)=(x4-ngh)+(2*ngh.*rand(size(x4,1),1));

 end
```

% OPTIMISATION PROBLEM FUNCTION

```
function output= BLPMSM_1_75kW_640RPM(para)

clear all; close all; clc;

global Weight Nm Eff Np D S_ebi L hm g f alphap q Kw Nph Pout kcarter miu0
miuR Hs Hs0 Hs1  Bs0 Bs1 Bs2 Rs As Hs2 Tw Phi DiaRYoke SOD BFgap Vt Bg
Bm  ks Br;

%% OPTIMAL PRIME VARIABLES %
para = [82.4408   50.0502    5.9353    7.1266];

% Stator inner diameter
D = para (1);
% Motor axial length /mm
L= para (2);
% magnet Thickness/mm
hm= para (3);
% Current density A/mm2
J= para (4);


%% Rated operating conditions and specifications
Pout=1750;                                  % rated power
rpm = 640;                                  % base speed
Vdc = 380;                                  % DC voltage
Vt= (Vdc-10)/(sqrt(3)*sqrt(2));             % Terminal Voltage
ph=3;                                       % Number of Phase

%% Selected parameters

Nm=9;                                       % Number of slots
Np=8;                                       % Number of poles
alphap=0.83;                                % Pole coverage coefficient
q=Nm/ph/Np;                                 % Slots/phase/pole
g=0.5;                                      % Airgap length /mm
Bs0=2;                                      % slot opening width
f=rpm*Np/120;                               % Frequency
```

```
%% %%%%%Properties of Magnet material %%%%%%

Br20 = 1.16;                        % remanence at 20 degree
miu0=4*pi*1e-7;                     % air permeability
miuR=1.1;                           % magnet permeability
alphaBr = -0.08;                    % magnet reversible temperature coefficient
op_Temp=140;                        % operating temperature
Br= Br20*(1+alphaBr*(op_Temp-20)/100); % remanence at operating temperature

%% %%%%%%% Airgap flux density %%%%%%%%%%
Flkg= 0.95;                  % flux leakage
Bg= Flkg*alphap*Br/(1+ (Flkg*g*miuR*alphap/hm)); % Airgap flux density
BFgap = 4/pi*Bg*sin(pi*alphap/2);          % flat-top Airgap flux density;
fundamental
Bm= Bg/Flkg;                                        % Magnet flux density

%% %%%%%Calculation of teeth width and yoke thickness%%%%

Bknee=1.35;                         %Flux density in stator core
ks=0.95;                            % Stacking factor of the stator iron laminations

% Total magnetic flux per pole produced by the magnets
Phi=BFgap*2*L*D/(Np)*1e-6;

% Thickness of the stator yoke
S_ebi=Phi/(2*Bknee*ks*L)*1e6;
% Thickness of the rotor yoke
R_ebi=Phi/(2*Bknee*ks*L)*1e6;

%Tooth flux concentration factor
kds = (pi*D/Nm)/(pi*D/Nm-(2*Bs0));

% Stator tooth width
Tw=Phi*kds/(Bknee*ks*L)*1e6;

Dmag=D-(2*g);                       % Magnet outer diameter
DiaRYoke = Dmag-2*(hm+R_ebi);       % Rotor inner diameter
Rm = Dmag/2 ;                       % Magnet outer radius
theta = 360/Np*alphap;              % Magnet pitch (degree)
Wm = 2*Rm*sind(theta/2);            % Magnet base width
```

```
hm1 = sqrt(Rm^2 - (Wm/2)^2);                % distance between rotor centre and
top-magnet rectangular
hmt = Rm - hm1;                             % height of the magnet cord
hm2= hm - hmt;                              % distance between magnet top-
magnet rectangular and magnet base
chord_arc = 2*acos(1-(hmt/Rm));

Chord_Area = 0.5*Rm^2*(chord_arc - sin(chord_arc)); % top-magnet chord area

%% %%%%%% Calculation of number of turns and current   %%%%%%

% With full pitch winding, winding factor
Kw=0.945;

% Slot type 3
Hs0 = 1.5;
Hs4 =1.5;
Rs = 0;
Bs1 = pi*(D+2*(Hs0+Hs4))/Nm-Tw;             % slot-bottom width
Ttw = D*pi/9-Bs0;                           % Teeth pitch at D
BsR = (Ttw - Tw);
Tangle = 30;
Hs1 = 0.5*BsR*tand(Tangle);

% Number of total turns per phase
Nph=round(fsolve('turnperphase',200));
NCoil_half=round(ph*Nph*2/Nm/2);            % Number of turns per half slot
NCoil=NCoil_half*2;                         % Number of turns per slot
Nph=NCoil*Nm/2/ph;

% RMS Back EMF
EMF =Nph*4.44*f*Kw*BFgap*2/pi*pi*D*L/Np/1000^2;

% RMS phase current
Ip=Pout/3/EMF;

%% Wire size determination
DW1=sqrt(Ip/J/pi)*2;                        % Wire diameter
G =round(log(DW1/8.24865)/log(0.890526));   % Wire gauge formula
DWG=8.24865*(0.890526)^G;                   % Wire diameter AWG
AWire=pi*DWG^2/4;                           % wire cross section area
```

```
Acu=AWire*Nph/q/(Np/2);                    % Copper area per slot
J=Ip/AWire;                                % Recalculate current density

%% %%%%%%%%%% Calculation of stator slot size %%%%%
Kfill=0.5;                                 % Copper Fill factor
As=Acu/Kfill;                              % Stator slot area per slot
Hs = fsolve('tlength',20);                 % Teeth length
SOD=D+2*(Hs+S_ebi);                        % Stator outer diameter
Hs2 = Hs-Hs0-Hs1;
Bs2 = pi*(D+2*(Hs0+Hs1+Hs2))/Nm-Tw;        % slot-top width
Aslotto=(Bs1+Bs2)*Hs2/2+(Bs2-2*Rs)*Rs+pi*Rs^2/2;

%% %%%%%%%%Calculation of inductance %%%%%%%%
%Magnetising inductance
eg=g+hm/miuR;                              % equivalent length of the airgap

% Carter Coefficient
gamma=4/pi*(Bs0/2/eg*atan(Bs0/2/eg)-1/2*log(1+(Bs0/2/eg)^2));

ts=pi*D/Nm;                                % tooth pitch
Kcarter=ts/(ts-gamma*eg);                  % Carter Coefficient

% airgap inductance
Lsg=3/pi*(q*Nph/q/(Np/2)*Kw)^2*miu0/(g*kcarter+hm/miuR)*(D-2*g)*L/1000;

Bsm=(Bs1+Bs2)/2;                           % slot mean width

% slot leakage inductance
Llslot=q*Np*(Nph*3/Nm*2)^2*miu0*(Hs2*L/3/Bsm+Hs1*L/((Bs1+Bs0)/2)+Hs0*
L/Bs0)/1000;

% End inductance
Llend=q*Np*miu0*(Tw+Bsm)*(Nph*3/Nm)^2/2*log((Tw+Bsm)*sqrt(pi)/(sqrt(2*A
s)))/1000;

% Total leakage inductance
Ll=Llslot+Llend;
Xl=2*pi*f*Ll;

% Total self-inductance
LS = Lsg+Llslot+Llend;
```

```
Xg=2*pi*f*Lsg;

%% %%%%% Calculation of copper loss %%%%%%%%%%%%%
% Resistivity of copper
pcu=1.68*1e-8;

% End length of one turn, assume full pitch winding
Lend = pi*(D+ Hs)/Nm ;
% Lend = 0.55*((0.05*Np/2)*pi*(D+Hs/Np)*Tw/(pi*D/Np)+0.02);
% Wire length of one turn
Lwireturn=L*2+Lend*2;
% Total wire length
Lwire=Nph*Lwireturn;

% Wire resistance
Rph=pcu*Lwire/AWire*1000;
% Armature copper loss
PCu=Ip^2*Rph*3;

%% %%%%%%%% Calculation of active weight %%%%%%%%%%%%

Msteel=7.8*1e3;                                    % steel Mass density
Mcu=8.954*1e3;                                     % copper Mass density
Mpm=7500;                                          % mass density of NdFeB


% Weight of the stator bore in kilogram
WSebi=pi*(SOD^2-(SOD-2*S_ebi)^2)/4*L*Msteel*(1e-9);

% Weight of the stator teeth
WTw=Nm*Tw*Hs*L*Msteel*(1e-9);

% Weight of the rotor yoke
WRebi=pi*((DiaRYoke+2*R_ebi)^2-DiaRYoke^2)/4*L*Msteel*(1e-9);

% Weight of copper
WtCopper=3*Lwire*AWire*Mcu*1e-9;
% Weight of Permanent Magnet
WtMagnet = Np*((hm2*Wm)+Chord_Area)*L/1000^3*Mpm;
```

```
%% Calculate penalty function for saturation
mmfarm = 3*sqrt(2)*Kw*Nph*Ip/(pi*Np/2);
Barm = miu0*miuR *mmfarm/(eg*1e-3);
Bmax = Bknee+Barm;

%% Calculation of core loss
% % Core loss estimation at no load condition% % Loss density W/kg
Kh = 0.00754373;
alp = 1.29522;
bet = 1.79624;
ke = 3.11146e-5;

% steinment equation
Los_st = (Kh * f^alp * Bmax^bet + ke*(f*Bmax)^2)* WSebi   ;
Los_Tw = (Kh * f^alp * Bmax^bet + ke*(f*Bmax)^2) *WTw  ;
Los_Rbi= (Kh * f^alp * Bmax^bet + ke*(f*Bmax)^2) *WRebi   ;

Pcore = Los_st + Los_Tw ;

% Estimation of windage and friction loss
Pwf=0;

%% Magnet protection from demagnetization
% Rated condition
Bk=0;
% demagnetisation current
I_demag=Np*pi/(6*miu0*Kw*Nph)*(Br*hm/1000 - Bk*(g+hm)/1000);

% maximum allowable rms stator phase current before demagnetization
dmg_rated=Ip/I_demag;              % demagnetization indicator. dmg_inc<1, no
demagnetization
dmgrL=0.9;                         % trigger of demagnetization at rated condition
sldmgr=10;
pelDmgr=linpenalty(dmg_rated,[dmgrL sldmgr]); % penalty function for
demagnetization at rated condition
dmg_short=(8/pi*alphap*Br*hm/1000)/(Br*hm/1000-Bk*(g+hm)/1000)-1;
dmg_shortinc=dmg_short/(Xl/Xg);                                    % the
machine is safe when Xl/Xm is larger than dmg_short, or dmg_shortinc<1
dmgsL=1;                           % lower bound to rigger
sldmgs=10;                         % slope
```

```
pelDmgs=linpenalty(dmg_shortinc, [dmgsL sldmgs]); % penalty function for
demagnetization at short circuit

I_LR = Vt/( Rph+Xl);                              % locked rotor current
MMF_LR = 3*sqrt(2)/pi*Kw*Nph*I_LR/(Np/2);

%% Constraints

% constrain on saturation
if Bmax > 1.6
   pelSat = 1;
else
   pelSat =0;
end
% constrain on magnet weight
if WtMagnet > 0.53
   pelMwt = 1;
else
   pelMwt = 0;
end

%% Performance indices
Volume=pi*(SOD)^2/4*L/1000^3*1000;          % machine Volume
Weight=WSebi+WTw+WtCopper+WRebi+WtMagnet;   % Total weight
Eff=Pout/(Pout+PCu+Pcore+Pwf)*100;          % Efficiency

%% Objective Function
% sum of penalty function
penaltysum = 1000*(pelSat+pelMwt +pelDmgr+ pelDmgs);%% +hm_pen +Pel_J
output = Weight + 20*WtMagnet+ (100-Eff) + 10*Volume +penaltysum;  %
```

%%% Function to calculate number of stator turns

```
function FFEM=turnperphase(Nph)
global Nm Np D BFgap   hm g  f  q Kw  L Pout kcarter miu0 miuR Hs0 Hs1 Bs0
Bs1 Bs2 Hs2 Tw Vt ;

% rms value of induced back emf
E=4.44*f*Nph*Kw*BFgap*2/pi*pi*D*L/Np/1000^2;

% rms value of armature current
I=Pout/3/E;

% %Magnetising inductance
gp=g+hm/miuR;

% Carter Coefficient
gamma=4/pi*(Bs0/2/gp*atan(Bs0/2/gp)-1/2*log(1+(Bs0/2/gp)^2));

taos=(pi*D/Nm)- Bs0;
kcarter=taos/(taos-gamma*gp);

Lm=3/pi*(q*Nph/q/(Np/2)*Kw)^2*miu0/((g+hm/miuR)*kcarter)*D*L/1000;

% Temporary value for Bs2
Bs2=1.5*Bs1;
wsb=(Bs1+Bs2)/2;

% Temperary value for Hs2
Hs2=2*Tw;
Llslot=q*Np*(Nph*3/Nm*2)^2*miu0*(Hs2*L/3/wsb+Hs1*L/((Bs1+Bs0)/2)+Hs0*
L/Bs0)/1000;
%Approximation of end slot leakage inductance
Llend=0.05*Llslot;
Ll=Llslot+Llend;
FEFM=(E+0.2*I)^2+(2*pi*f)^2*(Lm+Ll)^2*I^2 -Vt^2;
```

%%% Function to calculate slot height

```
function SlotH = tlength(Hss)
global Nm D Hs0 Hs1 Bs1 Bs2 Rs As Hs2 Tw ;
Hs2=Hss-Hs0-Hs1;
Bs2=((D/2+Hs2+Hs1+Hs0)*tan(pi/Nm)-Tw/2/cos(pi/Nm))*2;
Bs1=((D/2+Hs0+Hs1)*tan(pi/Nm)-Tw/2/cos(pi/Nm))*2;
Aslottotal=(Bs1+Bs2)*Hs2/2+(Bs2-2*Rs)*Rs+pi*Rs^2/2;
SlotLiner=0.001;
WedgeThick=0.001;
LayIns=0.001;
AslotWire=Aslottotal-Hs2*LayIns-Bs2*LayIns-
(2*Bs1+Bs2+2*Hs2/cos(pi/Nm))*SlotLiner-Bs1*WedgeThick;
SlotH=AslotWire-As;
```